University of Central Florida
STARS

Electronic Theses and Dissertations | Doctoral Dissertation (Open Access)

Sparse Signal Recovery Under Sensing and Physical Hardware Constraints

2019

Davood Mardaninajafabadi
University of Central Florida

Find similar works at: https://stars.library.ucf.edu/etd

University of Central Florida Libraries http://library.ucf.edu

 Part of the Electrical and Electronics Commons

STARS Citation

Mardaninajafabadi, Davood, "Sparse Signal Recovery Under Sensing and Physical Hardware Constraints" (2019). *Electronic Theses and Dissertations*. 6527.
https://stars.library.ucf.edu/etd/6527

This Doctoral Dissertation (Open Access) is brought to you for free and open access by STARS. It has been accepted for inclusion in Electronic Theses and Dissertations by an authorized administrator of STARS. For more information, please contact lee.dotson@ucf.edu.

SPARSE SIGNAL RECOVERY UNDER SENSING AND PHYSICAL HARDWARE CONSTRAINTS

by

DAVOOD MARDANI NAJAFABADI
B.S. in Electrical Engineering, Islamic Azad University, Najafabad, Iran, 2009
M.S. in Electrical Engineering, Yazd University, Yazd, Iran, 2012

A dissertation submitted in partial fulfilment of the requirements
for the degree of Doctor of Philosophy
in the Department of Electrical and Computer Engineering
in the College of Engineering and Computer Science
at the University of Central Florida
Orlando, Florida

Summer Term
2019

Major Professor: George Atia

© 2019 Davood Mardani Najafabadi

ABSTRACT

This dissertation focuses on information recovery under two general types of sensing constraints and hardware limitations that arise in practical data acquisition systems. We study the effects of these practical limitations in the context of signal recovery problems from interferometric measurements such as for optical mode analysis.

The first constraint stems from the limited number of degrees of freedom of an information gathering system, which gives rise to highly constrained sensing structures. In contrast to prior work on compressive signal recovery which relies for the most part on introducing additional hardware components to emulate randomization, we establish performance guarantees for successful signal recovery from a reduced number of measurements even with the constrained interferometer structure obviating the need for non-native components. Also, we propose control policies to guide the collection of informative measurements given prior knowledge about the constrained sensing structure. In addition, we devise a sequential implementation with a stopping rule, shown to reduce the sample complexity for a target performance in reconstruction.

The second limitation considered is due to physical hardware constraints, such as the finite spatial resolution of the used components and their finite aperture size. Such limitations introduce non-linearities in the underlying measurement model. We first develop a more accurate measurement model with structured noise representing a known non-linear function of the input signal, obtained by leveraging side information about the sampling structure. Then, we devise iterative denoising algorithms shown to enhance the quality of sparse recovery in the presence of physical constraints by iteratively estimating and eliminating the non-linear term from the measurements. We also develop a class of clipping-cognizant re-

construction algorithms for modal reconstruction from interferometric measurements that compensate for clipping effects due to the finite aperture size of the used components and show they yield significant gains over schemes oblivious to such effects.

To my lovely and supportive wife, Beheshteh.

ACKNOWLEDGMENTS

I would like to express my profound gratitude to my advisor, Dr. George Atia, for his support and being a fantastic teacher who I learned a lot from him. I also would like to thank Dr. Ayman Abouraddy, for helping me to become familiar with many optical concepts. I would like to thank the committee members, professor Wasfy Mikhael, Dr. Nazanin Rahnavard, and Dr. Azadeh Vosoughi.

I would like to thank my father, Amir, and my mother, Zahra, for their endless kindness and love.

This work is supported by the U.S. Office of Naval Research contracts N00014-14-1-0260 and N00014-17-1-2458, and NSF CAREER Award CCF-1552497

TABLE OF CONTENTS

LIST OF FIGURES

CHAPTER 1: INTRODUCTION

Inverse problems wherein one aims to solve for unknown input signals or model parameters from collected data are prevalent in image and signal processing [1], optical tomography [2], computer vision and machine learning [3, 4], just to name a few. Despite noteworthy efforts to develop theory and algorithms for the inverse problems and information recovery, much of the existing work have assumed ideal acquisition systems. The effects of sensing constraints and physical hardware limitations on performance, however, have been largely unexplored. For example, while much work was devoted to leveraging structural information inherent to signals and light beams (e.g., sparsity [5], total variation [6], etc.) through the use of regularizers and studying its implications on data acquisition (e.g., recovering signals from a reduced number of measurements [7]), very little is known about the interplay of sensing and hardware limitations and signal reconstruction[1].

Among such limitations are the limited number of degrees of freedom of actual data acquisition and sampling (imaging)systems [9, 10, 14], and physical constraints imposed by imperfect hardware components forming the sensing structure, such as the finite aperture size of the hardware components in optical and imaging applications [15], and their finite spatial resolution (e.g., Spatial Light Modulators (SLMs), optical detectors, and Digital Micromirror Devices (DMDs)) [7, 16, 17, 18], to name a few. Below, we elaborate on some of the most common limitations in practical inverse problems, and explain how they adversely affect the performance of information recovery.

[1]In this chapter, we partially use the material published in Signal Processing, 2019 [8], Optics express, 2015 [9], Optics Express, 2018 [10], Journal of the Optical Society of America A (JOSA A), 2018 [11], Allerton Conference on Communication, Control, and Computing, 2016 [12], and Annual Conference on Information Sciences and Systems (CISS), 2017 [13].

Limited number of degrees of freedom: The number of degrees of freedom of a given data acquisition/sensing system sets a limit on its information capacity. For example, in interferometry-based holography and optical imaging [19, 20, 21], the swept delay in the reference arm of a two-path interferometer is the sole degree of freedom at hand. As a result, successful recovery typically necessitates a large sample complexity due to the limited informational content of the highly-correlated measurements.

This motivated the use of additional hardware components such as introducing optical masks along the path of the optical field in optical imaging and spectroscopy [7, 16, 22, 18, 23], and quantum state tomography [24, 25]. For example, in compressive signal and image recovery problems in which Compressive Sensing (CS) recovery algorithms are adopted to reconstruct a sparse signal of interest from measurements collected by a data acquisition system with a limited number of degrees of freedom, one may introduce additional (non-native) hardware components to emulate randomization. This is the underlying idea of the single-pixel camera [7, 20] where a time-varying random mask is used to acquire random projections of a scene instead of directly collecting the pixels/voxels using a large size detector. Random masks in the form of a DMD (an array of millions of individually addressable and tiltable mirror-pixels) are also utilized in optical encryption for secure communication in optical networks to compress the encrypted data prior to transmission [26, 27].

While the extra degrees of freedom afforded by the randomization pattern that these masks map on the field can boost the acquisition system's capability, the design of such masks – which are non-native to such systems – is neither cost- nor overhead-free. Moreover, since such masks block a large portion of the light field through sampling, they tend to reduce the effective signal-to-noise ratio (SNR) [28, 29].

Finite spatial resolution: Another important limitation stems from the finite spatial

resolution of cameras and optical detectors. For instance, the non-vanishing pixel size of the random masks used to either collect measurements [7] or illuminate an object [16] in imaging applications contributes to the spatial resolution of the formed images. The use of finer pixels to step-up resolution comes at the expense of higher-dimensionality [30], thereby trading-off spatial resolution for computational/design cost, as well as potential degradation in signal reconstruction following from the curse of dimensionality phenomenon [30].

In dealing with this limitation one may adopt super-resolution techniques, in which one aims to recover *missing information* about an object or light beam due to various practical restrictions (such as the optical diffraction limit [31] and the non-zero detector pixel size in optical imaging) by leveraging *prior information about the input signal* [32] . For example, in super-resolution techniques used for imaging, the non-redundant information of several images and frames are combined to improve the resolution of one image [33]. However, most of the super-resolution techniques necessitates to adopt more detectors (cameras) and hardware components which comes at the expense of more cost and computational analysis.

Aperture finiteness: The Finite-aperture size of hardware components used to implement a sampling system introduces non-linearities into the measurement model due to the ensuing clipping in the spatial domain [15]. For example in optical applications, when the light field expands due to spatial diffraction upon propagation, it gets clipped given the finite aperture size of lenses, SLMs, masks, etc. [15, 28], leading to undesired loss of information in the tail of the beam profile beyond the aperture size.

Hardware imperfection effects, such as the signal clipping stemming from the finite aperture size of the used components, and the limited spatial resolution of SLMs and detectors due to their non-vanishing pixel size, can also degrade the quality of the recovered information in optical imaging systems in which an active light source is used to illuminate a sample

object [19, 34]. In such systems, a sample object, such as a living tissue, is illuminated by a reference light beam and then the information of interest regarding the object is acquired by analyzing the reflected, scattered, or diffused version of the illumination light field. The properties of the illumination light field and its behavior in the scattering media tightly depend on the hardware setup generating it. Any destructive effect stemming from imperfect hardware components, such as the clipping effect, can drastically change the properties of the illumination filed, which, in turn, affects the quality of image recovery. For example, one may adopt the spatial-temporal diffraction-free light beams (ST-beams) proposed in [35, 36] to illuminate a sample object in an imaging problem. The limited size of the gratings and the SLM used to generate such beams can change the propagation distance of such light fields in a sample object such as a retina.

Scope and contributions

To collect more informative measurements and improve the performance of signal reconstruction under practical constraints, most of the above-mentioned solutions existing in the literature focus on hardware modifications and introduce new hardware components to the sampling structure, which incurs extra cost and complexity. In contrast, in this dissertation we keep the native sampling system unchanged and focus our attention on designing efficient sampling strategies by judiciously leveraging the available degrees of freedom and devising appropriate compressive recovery algorithms to obtain a more accurate solution for the inverse problem under practical sensing and physical constraints.

We focus here on interferometry problems, however, the sampling strategies, reconstruction algorithms and analysis machinery developed in this thesis are generally applicable to a wide range of practical signal recovery problems. In an interferometry problem, measurements are

interferograms generated by directing the input signal or light field into two different paths, namely the arms of the interferometer, and superposing their output signals. Interferometry is a very effective tool in many information recovery applications ranging from optical modal analysis [37], and imaging [38, 39], to wireless communications and radio interferometry applications [40, 41]. We provide a comprehensive description for different interferometry systems and their functionality later in the next chapter.

The contributions of this dissertation can be summarized as follows:

Unifying basis analysis framework. We first develop a unifying framework for signal reconstruction from interferometric measurements. Based on this framework, the problem of signal recovery from interferograms amounts to basis analysis in a Hilbert space. We leverage a generalized interferometry approach proposed to access the modal contents of a light beam in an optical modal analysis problem [15, 42] to enable the analysis and reconstruction of signals encountered in a broader range of applications of interferometry, of which optical modal analysis is a special case. There are two sources of generality for the basis analysis framework developed herein. First, it is applicable whether the sought-after information pertains to the input signal or to a sample object placed in the second arm of the interferometer. Modal analysis is an example of the former case and Optical Coherence Tomography (OCT) [43] an example of the latter (See Chapter 3). Therefore, we account for scenarios where the input beam passes through the second arm of the interferometer unchanged, as well as scenarios where the beam interacts with a sample object of interest. Second, our approach extends to scenarios where we may have no control over the relative delay of the two paths of the interferometer. This arises for example in the context of node localization in wireless networks. In all cases, we show that the information of interest is embedded in the coefficients of the expansion of the output signals of the interferometer arms in some relevant basis. Therefore, information recovery reduces to a problem of basis analysis in an

appropriate function space, where one can adopt a reconstruction algorithm to reveal the expansion coefficients of the interferometer signals from the interferometric measurements.

Compressive reconstruction under sensing constraints. Despite noteworthy efforts to develop performance guarantees for sparse recovery, the focus has been mostly on systems that take (noise-like) unstructured measurements in the form of a series of inner products against random vectors. From a practical standpoint, the relevance of such results is somewhat limited since we are not always at liberty to choose the type of measurements used for acquisition. However, we show both analytically and experimentally that the class of problems considered is amenable to compressive reconstruction whereby significant gains in sample and computational complexities can be achieved given prevalent sparse representations of the signals of interest in given bases.

This is an important distinction from prior work leveraging compressive sensing (CS)-based techniques in practical applications where compression gains are realized at the price of introducing new hardware components into the sampling setup – typically in the form of a sequence of designed random masks in optical applications. Here, we show that the linear transformation of the underlying measurement model satisfies sufficient conditions for a successful reconstruction such as the Restricted Isometry Property (RIP) [30], and the isotropy and incoherence properties [44], most notably under the sensing constraints set by the limited degrees of freedom of the interferometer. Hence, our contribution along this dimension aligns with, and complements, ongoing efforts to establish performance guarantees with *structured systems*, albeit these have been primarily focused on Fourier samples or Radon slices for magnetic resonance and tomographic imaging [45].

Controlled sampling policies. Beside the limited number of degrees of freedom of practical data acquisition systems, *unknown* statistical model of the sampling error or noise sets

another limitation on the quality of the reconstructed information. In such scenarios, we need more sophisticated sampling strategies, instead of random sampling methods, to collect the most informative measurements. Therefore, We leverage the side-information about the constrained sensing structure to guide the collection of informative measurements through design of efficient control policies. These policies maximize the measurement incoherence to further reduce the sample complexity for a target quality in reconstruction. We first develop two controlled sampling strategies which can be applied in a wide range of applications of CS under sensing constraints, where the linear transformation is a matrix with structured rows. Then, we show how these sampling strategies can be adopted in the interferometry problems to improve the quality of reconstruction.

Compressive recovery with structured noise. Sensing systems implemented by imperfect hardware components, such as optical detectors or cameras with finite spatial resolution or aperture size, set another limitation on the quality of signal recovery. Such limitations introduce non-linearities in the underlying measurement model. We first develop a more accurate measurement model with structured noise representing a known non-linear function of the sparse signal obtained by leveraging side information about the physical sampling structure. Then, we devise two iterative denoising algorithms, namely, Orthogonal Matching Pursuit with Structured Noise (OMPSN), and Subspace Pursuit with Structured Noise (SPSN) that are shown to enhance the quality of sparse recovery in presence of physical constraints by iteratively estimating and eliminating the non-linear term from the measurements. Numerical and simulation results demonstrate that the proposed algorithms outperform standard algorithms in detecting the support and estimating the sparse vector, given the non-linear function describing the structured noise.

Generalized interferometry under finite-aperture effects. Interferometric modal analysis under clipping effects is a practical information recovery problem whose performance

can be significantly improved by modeling such effects as a structured noise described by a non-linear function. We first show that the aperture finiteness of the hardware components has the most destructive effect on the recovery performance in the optical modal analysis problem. We then develop a clipping-cognizant measurement model capturing the finite aperture size using clipping Linear Canonical Transforms (LCTs). This model is used to represent the hardware implementation of the interferometer as a cascade of regular and clipping LCTs, and calculate the non-linear function describing the structured noise in the measurement model imposed by hardwares with finite aperture size. We also develop iterative modal reconstruction schemes leveraging the clipping-cognizant measurement model to compensate for the clipping effects.

Effect of imperfect hardware on the properties of spatial-temporal beams (ST-beams). Spatial-temporal diffraction-free beams, newly introduced in [35, 36], are provably able to propagate for large distances with no or small diffraction. This favorable property makes them attractive candidates in active data acquisition systems, in which the scattered field of an active light source is used to recover information about objects of interest. First, we briefly overview the theory of ST beams, list some of their properties, and describe the hardware setup used to generate them. Then, we explain how imperfect hardware components (such as limited-size gratings) can affect the properties of such beams and their behavior in scattering environments. We will model all of these unwanted effects as a parameter in the light field equation called *spectrum uncertainty*, and explain how it affects our ability to access the sought-after information in a practical inverse problem with an active light source.

CHAPTER 2: PRELIMINARIES

In this chapter[1], we provide a brief background on interferometry as an effective sampling strategy in many applications ranging from optical imaging and tomography [43] to radio interferometry and localization in wireless networks [40]. We also briefly go over the underlying idea of compressive sensing theory and list few compressive recovery algorithms used in this dissertation.

Interferometry

Interferometry is a measurement strategy that is widely used across all the physical sciences, with applications ranging from astronomy and radio interferometry [46, 47, 48, 49, 50], to remote sensing and Interferometric Synthetic Aperture Radar (InSAR) [51, 52], optics and photonics [53, 54], signal processing and communications [40, 55], optical encryption [27], and bio-imaging [19, 38]. Underlying the utility of interferometry in all these fields is the fundamental principle of superposition of linear waves, which applies to optical, radio-frequency, and acoustic waves, among other physical realizations. By judiciously superposing two versions of a wave, their interference may reveal sought-after information, typically about a sample or a medium that one of the waves scattered from. The interferometer in which the superposition takes place may be an instrument implemented using electrical and optical components (e.g., a Michelson interferometer in Optical Coherence Tomography (OCT) [19]), or simply a physical medium (e.g., the atmosphere in the case of localization in wireless sensor networks [40, 41]).

[1]In this chapter, we partially use the material published in Signal Processing, 2019 [8], Optics express, 2015 [9], and Optics Express, 2018 [10].

Common to all such problems are interferometric measurements, so-called *interferograms*, obtained by acquiring the energy of the superposition of the two waves or signals while some parameter is swept [56, 53]. The interferogram typically assumes values related to the auto-correlation and cross-correlation of the signals in the interferometer, which depend on the characteristics of its arms (e.g., their physical lengths in temporal interferometry). For example, in time domain OCT, one can acquire several interferometric measurements by sweeping the time delay in one of the interferometer arms [43].

Some applications:

Optical coherence tomography: OCT is a non-invasive and contact-free optical imaging method which provides high-resolution depth and transversal images from different layers of a sample object [19], and is a heavily used bio-imaging technique in ophthalmology to capture high resolution cross-sectional images of the retina [57]. In OCT, a low-coherence source emits a light beam that scatters off a sample object such as living tissue as shown in Fig. 2.1(a). The scattered light is then combined with a delayed version of the input beam to reveal the depth information of the object [43]. In this example, the path which has the sample object corresponds to the second arm of the interferometer whose reflectivity indices at the different layers are of interest. In the proposed framework, we show that the reflectivity indices appear in expansion coefficients related to the interferometric measurements.

Sensor localization: A second example pertains to localization in wireless sensor networks. As shown in Fig. 2.1(c), to determine position, a node receives two signals with two different frequencies from two adjacent anchor nodes. By synchronizing the receiver and transmitters, the delay of each path defines the distance between the nodes. Hence, the position information is embedded in the energy of samples of the combined signal [40].

Optical modal analysis: Another example is that of optical modal analysis [54, 37, 9], in which measurements collected using an optical interferometer – such as the Mach—Zehnder interferometer of Fig. 2.1(b) – are used to reveal the modal content of an optical beam.

Optical beams offer the potential for carrying a high-information content by exploiting the large-dimensional space spanned by its physical degrees of freedom (DoFs). The spatial DoF has attracted particular interest with recent advances in the synthesis and analysis of beams having complex spatial profiles [37]. Indeed, spatial multiplexing for high-speed communications in free space [58] and in multimode fibers [59] has brought to the fore the importance of accurate and rapid modal analysis in a desired basis [60], such as the that of orbital angular momentum (OAM) modes [61].

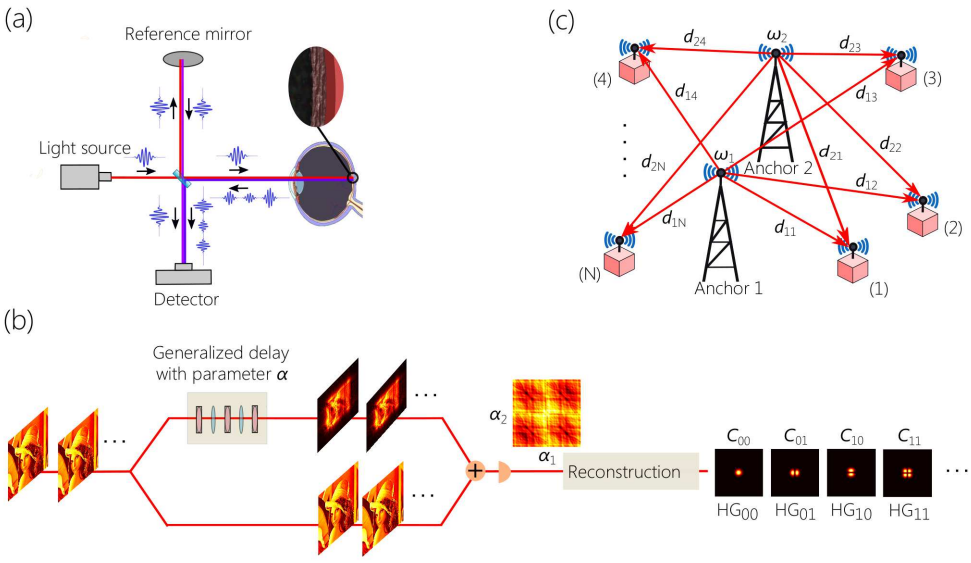

Figure 2.1: (a) Schematic of the OCT implementation using a Michelson interferometer. (b) Two-dimensional modal analysis using the generalized interferometry approach based on Hermite-Gaussian modes. (c) Topology of a wireless sensor network used for node localization.

We recently proposed an interferometric procedure that allows – in principle – for an optical beam to be analyzed in terms of a complete and orthogonal – but otherwise arbitrary – modal basis [54, 37]. We call this approach henceforth 'generalized interferometry'. Such a

strategy exploits a two-path interferometer (such as a Mach-Zhender interferometer, MZI), but replaces the usual optical delay with a 'generalized phase operator' (GPO) – a unitary spatial transformation parameterized by a continuous real number that plays the role of a 'generalized delay' in modal space. The GPO is in fact an optical transformation whose eigenfunctions are the functional elements of the modal basis of interest. Indeed, the GPO generalizes to an arbitrary basis the notion of temporal delay. The GPO delay parameter in the generalized interferometer is swept, an interferogram is recorded, and its Fourier transform reveals the beam's modal content. In the case of discrete modal bases, the GPO is a fractional optical transform; e.g., the fractional Fourier transform (frFT) [62, 63] or fractional Hankel transform (frHT) [64, 65] for Hermite-Gaussian (HG) or radial Laguerre-Gaussian (LG) modes, respectively. In practice, measurements are acquired by sampling the GPO delay – the order of the associated fractional transform – at the Nyquist rate to avoid aliasing in modal analysis. This requires collecting a large number of samples and implies more latency, which may be intolerable for delay-sensitive applications. In the next chapter, we elaborate on the generalized interferometry approach proposed.

Compressive sensing

Sparse signals are often vectors in a high-dimensional space with only few non-zero elements – known as the *support* of the signal. An $N \times 1$ vector $\mathbf{x}$ with at most s non-zero elements is called 's-sparse'. Based on the CS theory, the sparse signal $\mathbf{x}$ can be successfully recovered in a space of ambient dimension N from only $M \ll N$ linear measurements,

$$\mathbf{y} = \mathbf{A}\mathbf{x} \tag{2.1}$$

provided that the $M \times N$ sensing matrix $\mathbf{A}$ satisfies some sufficient conditions [66, 67].

When the number of interferometric measurements M is smaller than the ambient dimension N, i.e., $M \ll N$, signal recovery is equivalent to solving an under-determined system of linear equations, which is generally an ill-posed problem since it has less equations than unknowns. However, searching for a solution is feasible if the signal is sparse. In particular, we can search for the most sparse solution that minimizes the ℓ_0-norm, $\|\mathbf{x}\|_0$, of the sought-after vector $\mathbf{x}$, subject to the data constraint, i.e.,

$$\min \quad \|\mathbf{x}\|_0 \quad \text{subject to} \quad \mathbf{y} = \mathbf{A}\mathbf{x}, \tag{2.2}$$

where $\|\mathbf{x}\|_0$ is equal to the number of non-zero entries of $\mathbf{x}$ [68]. Nonetheless, the problem in Eq. (2.2) is generally NP-hard as it involves a combinatorial search over all s-sparse vectors. The complexity can be significantly reduced using a convex relaxation of Eq. (2.2)

$$\min \quad \|\mathbf{x}\|_1 \quad \text{subject to} \quad \mathbf{y} = \mathbf{A}\mathbf{x}, \tag{2.3}$$

where $\|\mathbf{x}\|_1 = \sum_{n=1}^{N} |x_n|$ is the ℓ_1-norm of $\mathbf{x}$. This ℓ_1-minimization, known as the Basis Pursuit (BP), can be reduced to a simpler Linear Programming (LP) problem, then solved using an appropriate technique such as the Primal-Dual Interior-Point Method for Convex Objectives (PDCO) [69].

It is recognized that (2.3) can successfully recover a sparse vector $\mathbf{x} \in \mathbb{R}^N$ from $M \ll N$ measurements provided the sensing matrix $\mathbf{A}$ satisfies some conditions [30]. For example, it has been established that an s-sparse vector (with at most s non-zero elements) can be reconstructed using (2.3) if $\mathbf{A}$ satisfies the Restricted Isometry Property (RIP), which requires that $(1-\delta)\|\hat{\mathbf{x}}\|_2^2 \leq \|\mathbf{A}\hat{\mathbf{x}}\|_2^2 \leq (1+\delta)\|\hat{\mathbf{x}}\|_2^2$ for any $\hat{\mathbf{x}} \in \Sigma_{2s}$, where $\Sigma_{2s} := \{\mathbf{x} \in \mathbb{R}^N : \|x\|_0 \leq 2s\}$ is the set of all $2s$-sparse vectors in $\mathbb{R}^N$ for the restricted isometry constant $0 < \delta < \sqrt{2} - 1$.

In a noisy setting, the interferometric measurements can be modeled as, $\mathbf{y} = \mathbf{A}\mathbf{x} + \mathbf{z}$, where $\mathbf{z}$ is an additive $N \times 1$ noise vector. In this case, a denoising recovery algorithm such as the Dantzig selector [70],

$$\begin{aligned} &\text{minimize } \|\mathbf{x}\|_1 \\ &\text{subject to } \|\mathbf{A}^{\mathrm{T}}(\mathbf{A}\mathbf{x} - \mathbf{y})\|_\infty \leq \eta\,\sigma, \end{aligned} \tag{2.4}$$

can be utilized to enhance the fidelity of reconstruction given the RIP, where σ^2 is the variance of the entries of $\mathbf{z}$ and η is a parameter used to control the performance of reconstruction. Beside BP and Dantzig selector, there exist other reconstruction algorithms such as Matching Pursuit (MP) [71] and Subspace Pursuit [72] which could also be applied to recover the sparse vector of interest.

RIP is a strong sufficient condition which may not be satisfied in the practical applications in which the structure of the sensing matrix is imposed by a real data acquisition system. In these cases, sparse recovery can be shown to be successful using mentioned recovery algorithms provided that the sensing matrix $\mathbf{A}$ obeys the weaker isotropy and incoherence conditions [44], defined as follows:

Definition 1. *(Isotropy [44]) If the vector* $\mathbf{g}$ *denotes a row of a random matrix* $\mathbf{G}$ *drawn from a probability distribution* F*, then* F *is said to satisfy the isotropy property if* $\mathbb{E}[\mathbf{g}^H\mathbf{g}] = \mathbf{I}$*, where* $\mathbb{E}[.]$ *is the expectation and* $\mathbf{I}$ *the identity matrix.*

Definition 2. *(Incoherence [44]) The distribution* F *of* $\mathbf{g} = [g_n] \in \mathbb{C}^N$*, is said to be incoherent with incoherence parameter* $\mu(F)$ *if* $\max\limits_{n=1,2,\ldots,N} |g_n|^2 \leq \mu$*, where* μ *is the smallest number for which this inequality holds.*

The smaller the incoherence parameter μ of the sensing matrix, the less the number of measurements required for (2.3) to yield successful reconstruction [44, Theorem 1.1]. It

was also shown that algorithms such as LASSO [73] and the Dantzig selector [70] yield stable recovery from noisy measurements under the isotropy and incoherence conditions [44, Theorems 1.2 and 1.3].

Henceforth, we refer to the matrix $\mathbf{A}$ as *isotropic and incoherent* if the distribution F of its rows (specified by the generalized delay parameter) obeys the isotropy and incoherence properties.

CHAPTER 3: A UNIFYING MODEL FOR THE INTERFEROMETRIC MEASUREMENTS: HILBERT SPACE ANALYSIS

In this chapter[1], we develop a unifying model for interferometry shown to be applicable to a wide range of problems. We show that the information of interest is embedded in the expansion coefficients of the interferometer signals in an appropriate Hilbert space. For example, in temporal interferometry this space is the span of the set of complex harmonics. We show here how this concept generalizes to other bases enabling interferometry in a variety of bases related to any degree (or degrees) of freedom of the wave. In this framework, the interferometric measurements are shown to admit an explicit structured linear representation in basis coefficients of interest.

We first provide preliminary background on temporal interferometry, and summarize the main result of [37, 15] on generalized optical modal analysis wherein the techniques developed are generalized to arbitrary non-temporal DoFs. Subsequently, we present representative applications of interferometry and demonstrate the universality of the proposed approach.

Interferogram model in temporal interferometry

A generic interferometric configuration is depicted schematically in Fig. 3.1. An input signal or optical field $\psi(t)$, where t corresponds to time, is divided into two paths (or interferometer arms), whereupon two new versions $\psi_1(t;\tau)$ and $\psi_2(t)$ are created and combined to produce a superposed signal, $\psi_{\mathrm{s}}(t;\tau) = \psi_1(t;\tau)+\psi_2(t)$. The first arm (referred to as the 'reference' arm)

[1]In this chapter, we use the material published in Signal Processing, 2019 [8].

has an impulse response $h_1(t;\tau)=\delta(t-\tau)$ where τ is a temporal delay, and the second arm (the 'sample' arm) has an impulse response $h_2(t)$. An 'interferogram' is traced by scanning over the values of τ and recording the energy of the superposed signal $I(\tau)=\langle|\psi_s(t;\tau)|^2\rangle$, where $\langle\cdot\rangle$ corresponds to an integration over time. The interferogram is thus given by

$$I(\tau)=I_1+I_2+2|I_{12}(\tau)|\cos(\theta_{12}(\tau)). \tag{3.1}$$

The first two terms on the right hand side of (3.1), i.e. $I_1 \triangleq \langle\psi_1(t;\tau)\psi_1^*(t;\tau)\rangle$ and $I_2 \triangleq \langle\psi_2(t)\psi_2^*(t)\rangle$, represent the auto-correlation of the signals produced in each arm of the interferometer (the total energy of the signal in each arm), whereas the third term, $I_{12}(\tau) \triangleq \langle\psi_1(t;\tau)\psi_2^*(t)\rangle$, captures their cross-correlation, and $\theta_{12}(\tau)$ is the phase of $I_{12}(\tau)$. Interferometric measurements are collected by sampling the delay τ, and the sought-after information about the input signal or the sample is typically embedded in the cross-correlation term. When the impulse response of the sample arm $h_2(t)=\delta(t)$, the Fourier transform (FT) of the interferogram in (3.1) reveals the power spectrum. Although (3.1) provides a general model for interferometry that is commonly used, it does not show explicitly how the correlation term relates to the information of interest, whether this information pertains to the input signal or to the 'sample'.

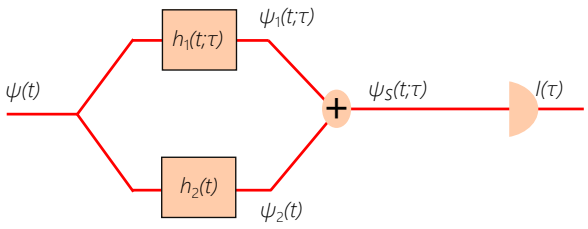

Figure 3.1: Schematic for a general two-path interferometer. The output signal of the reference arm is defined by the temporal delay τ.

Temporal interferometry as a basis analysis problem

We expand the input signal $\psi(t)$ in terms of harmonics or complex exponentials $\{e^{j\omega t}\}$, where ω is the angular frequency (i.e., the Fourier basis), such that $\psi(t) = \frac{1}{2\pi}\int_{-\infty}^{+\infty}\Psi(\omega)e^{j\omega t}d\omega$, where $\Psi(\omega)$ is the Fourier transform (FT). Hereon, we focus our attention on discrete bases by the mere fact that the data collected and the information retrieved is always represented discretely. In this case, the input signal is represented as $\psi(t) = \sum_{n=1}^{\infty} c_n e^{j\omega_n t}$ using the orthogonal discrete harmonics $\{e^{j\omega_n t}\}$ for some complex coefficients $c_n, n = 1, 2, \ldots$. Because of the discrete basis, the signal is periodic in time, so that all integrals over time extend over this period. The delay introduces a phase factor $e^{-j\omega_n\tau}$ to the coefficient c_n that is linear in τ and the modal 'index' ω_n,

$$\psi_1(t;\tau) = \psi(t-\tau) = \sum_{n=1}^{\infty} c_n e^{j\omega_n t}e^{-j\omega_n\tau}. \tag{3.2}$$

This fact will be utilized subsequently when introducing the notion of a 'generalized delay' [37, 15] for non-temporal degrees of freedom.

Modeling the sample arm of the interferometer as a linear time-invariant system $h_2(t)$, its output will be,

$$\psi_2(t) = \sum_{n=1}^{\infty} d_n e^{j\omega_n t}, \tag{3.3}$$

where $d_n = c_n H_2(\omega_n)$, $n = 1, 2, \ldots$, and H_2 is the Fourier transform of h_2. From (3.1) and the orthogonality of the complex harmonics, the interferogram becomes

$$I(\tau) = \sum_{n=1}^{\infty}|c_n|^2 + \sum_{n=1}^{\infty}|d_n|^2 + 2\sum_{n=1}^{\infty}|c_n||d_n|\cos(\omega_n\tau + \theta_n), \tag{3.4}$$

where θ_n is the phase of $c_n d_n^*$. As the first two terms do not depend on τ, we define the

interferometric measurements as,

$$\begin{aligned} y(\tau) &\triangleq \frac{1}{2}\left\{ I(\tau) - \sum_{n=1}^{\infty} \left(|c_n|^2 + |d_n|^2 \right) \right\} \\ &= \sum_{n=1}^{\infty} |c_n||d_n| \cos(\omega_n \tau + \theta_n). \end{aligned} \tag{3.5}$$

To collect M interferometric measurements, we sample M values τ_m, $m = 1, \ldots, M$, of the delay τ.

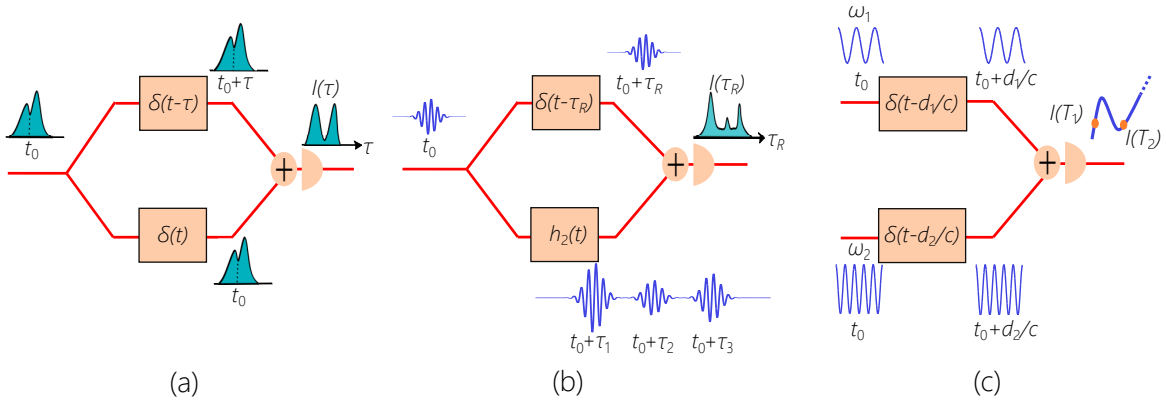

Figure 3.2: (a) Block diagram of the interferometry-based modal analysis. (b) Block diagram of OCT where the reference arm is modeled by a delay block, and the sample arm is modeled by an LTI system.(c) Block diagram of an interferometric based localization technique.

In the framework of temporal interferometry described here and in all subsequent modalities, only a finite number of coefficients c_n and d_n are of interest or even accessible by the acquisition systems. We thus introduce at this point a finite dimensionality N for the harmonic basis, $\{e^{j\omega_n t}\}_{n=1}^{N}$. Considering (3.5), we therefore obtain a linear model for the interferometric measurements in the time domain

$$\mathbf{y} = \mathbf{A}\mathbf{x}, \tag{3.6}$$

where the $M \times 1$ measurement vector $\mathbf{y}$ contains the interferometric measurements $y(\tau_m)$, the $2N \times 1$ information vector $\mathbf{x} = [\mathbf{x}_1^{\mathrm{T}} \ \mathbf{x}_2^{\mathrm{T}}]^{\mathrm{T}}$ consists of the two vectors $\mathbf{x}_1 = [|c_n||d_n| \cos(\theta_n)]$ and $\mathbf{x}_2 = [|c_n||d_n| \sin(\theta_n)]$, and the $M \times 2N$ matrix $\mathbf{A} = [\mathbf{A}_1 \ \mathbf{A}_2]$ is a block matrix with $\mathbf{A}_1 = [\cos(\omega_n \tau_m)]$, and $\mathbf{A}_2 = [-\sin(\omega_n \tau_m)]$, with $m = 1, 2, \ldots, M$ and $n = 1, 2, \ldots, N$.

The goal here is to recover some properties of the input signal (the coefficients c_n) or of the sample (the coefficients d_n) from the interferogram. The interferogram model (3.6) offers an immediate advantage. We have reduced *every* problem of temporal interferometry with the configuration in Fig. 3.1 to one of basis analysis. This is a unifying problem-independent framework in which the interferometric measurements admit a linear representation in terms of a matrix $\mathbf{A}$ of known structure, which enables more efficient approaches to information recovery.

To this point, we used temporal interferometry to analyze a signal or an optical field into its time-frequency harmonics. Instead, signals or optical fields can also be analyzed in different bases with spatial degrees of freedom, in Cartesian or polar coordinate systems, for example.

Generalized interferometry: Hilbert space analysis

In the previous section, we proposed a unifying model for temporal two-path interferometry. In this modality, we have shown that the desired information (the input signal or the sample) appears in the harmonic expansion coefficients of a linear measurement model. It turns out that the framework developed can be generalized to arbitrary degrees of freedom of the input signal beyond the temporal, such as the spatial parameters. Underlying this generalization is the notion of 'generalized delay', which replaces the standard temporal delay τ to allow for analysis in arbitrary bases for the other degrees of freedom.

In temporal interferometry, we have represented the input signal as a finite discrete superposition of time-frequency complex exponentials. The delayed output signal of the reference arm in (3.2) is obtained by passing the input signal through a temporal delay modeled as an LTI system with an impulse response $h_1(t;\tau) = \delta(t-\tau)$. Equivalently, applying a delay amounts to applying a linear phase factor $e^{-j\omega_n\tau}$, $n = 1, 2, ..., N$ to the basis harmonics $e^{j\omega_n t}$, $n = 1, 2, ..., N$. In other words, the harmonics $e^{j\omega_n t}$ are the *eigenfunctions* of the delay system $h_1(t;\tau)$ with *eigenvalues* $\lambda_n = e^{-j\omega_n\tau}$.

In moving to other degrees of freedom but maintaining the overall interferometric structure, we must replace the temporal delay with an appropriate 'generalized delay'. The signal in this case is an element in a Hilbert space spanned by an orthonormal basis $\{\phi_n(x)\}$ with respect to an arbitrary variable $x \in \mathbb{R}$ (e.g. space, angle, etc). As before, we represent the input signal or light field $\psi(x)$ as a superposition of the basis elements, $\psi(x) = \sum_{n=1}^{N} c_n\phi_n(x)$, where the c_n's are the basis coefficients. In this setting, we take the generalized delay α (potentially multi-dimensional) – represented by an impulse response $h_1(x;\alpha)$ – to be the unitary linear system whose impact on the signal is analogous to that of the temporal delay in (3.2). In other words, the eigenfunctions of the transformation $h_1(x;\alpha)$ must be the Hilbert-space basis $\{\phi_n(x)\}$ with eigenvalues of the form $e^{-jn\alpha}$. We refer to α hereon as the generalized delay parameter. With these features taken into consideration, the delay operator in the Hilbert-space basis takes on a diagonal representation,

$$h_1(x, x';\alpha) = \sum_{n=1}^{N} e^{-jn\alpha}\phi_n(x)\phi_n^*(x'). \tag{3.7}$$

The structure of this operator has several salutary properties that justify calling it a generalized delay. It is additive in the delay parameter $\int dx' h_1(x, x';\alpha)h_1(x', x'';\beta) = h_1(x, x'';\alpha+\beta)$; its inverse is the same operator but with a delay parameter $-\alpha$; and $h_1(x, x';0)$ is the iden-

tity. It has been shown that this structure corresponds in general to fractional transforms. For example, when the basis $\{\phi_n(x)\}$ is that of Hermite-Gaussian function, h_1 corresponds to the fractional Fourier transform (frFT) [62, 74]; when the basis is that of Laguerre-Gaussian functions, h_1 corresponds to a fractional Hankel transform, etc [64, 37].

As such, the response of this 'delay' to the input $\phi_n(x)$ is $\int_{-\infty}^{+\infty} \phi_n(x')h_1(x,x';\alpha)dx'$ will be $e^{-jn\alpha}\phi_n(x)$. Thus, a signal $\psi(x)$ after being 'delayed' takes the form

$$\psi_1(x;\alpha) = \int_{-\infty}^{+\infty} \psi(x)h_1(x,x';\alpha)dx' = \sum_{n=1}^{N} c_n e^{-jn\alpha}\phi_n(x). \tag{3.8}$$

This idea underlies our approach to conduct interferometry in arbitrary bases related to other degrees of freedom. As pointed out earlier, we focus on signals in finite-dimensional Hilbert spaces since in practice only few basis elements contribute to the actual signal or can be accessed.

The sample arm is modeled as an LTI system $h_2(x)$ that maps the input signal to an output

$$\psi_2(x) = \sum_{n=1}^{N} d_n\phi_n(x), \tag{3.9}$$

where $d_n,\ \ n = 1, 2, ..., N$ are new basis coefficients. In temporal interferometry, the signal energies are acquired by time-averaging for each setting of the temporal delay τ. Here, in generalized interferometry, the signal energy is obtained by averaging over the degree of freedom x for each setting of the delay α. Accordingly, the interferogram generated is

$$I(\alpha) = I_1 + I_2 + 2\sum_{n=1}^{N} |c_n||d_n| \cos\big(n\alpha + \theta_n\big), \tag{3.10}$$

which is analogous to (3.4), and I_1 and I_2 represent the energy in each arm.

A number M of interferometric measurements are collected by sampling the delay parameter $\alpha_m,\ m = 1, 2, ..., M$. Therefore, similar to (3.5), we obtain a linear model for the interferometric measurements where,

$$\begin{aligned} y(\alpha_m) &\triangleq \tfrac{1}{2}(I(\alpha_m) - I_1 - I_2) \\ &= \sum_{n=1}^{N} |c_n||d_n| \cos\big(n\alpha_m + \theta_n\big),\ m = 1, 2, ..., M. \end{aligned} \tag{3.11}$$

Thus (3.11) can also be cast in vector form as

$$\mathbf{y} = \mathbf{A}\mathbf{x}, \tag{3.12}$$

where the definitions and dimensions of the information coefficient vector $\mathbf{x}$, the measurement vector $\mathbf{y}$, and the matrix $\mathbf{A}$ are identical to those in (3.6) after replacing the temporal delay samples τ_m with the sampled generalized delay parameter α_m. Similar to temporal interferometry, the measurement model in (3.11) enables us to retrieve information about the input signal or the sample embedded in the coefficients c_n and d_n.

Remarkably, the result in (3.12) shows that the proposed framework is in fact basis-neutral. This is clear from the fact that $\mathbf{x}$, $\mathbf{y}$, and $\mathbf{A}$ have no traces of the basis functions $\{\phi_n(x)\}$, which is a consequence of the diagonal representation of the generalized delay in this basis. Therefore, any analysis based on (3.12) is independent of the underlying basis and applies equally to all. Based on this unifying model, the information of interest embedded in the expansion coefficients of the interferometer signals in an appropriate Hilbert space can be simply reconstructed by taking a FT of the collected interferograms.

Remark 1. *Our approach extends naturally to signals or fields described by multiple degrees*

of freedom, in which case interferometry can be performed in higher dimensions by introducing several generalized delays, one for each degree of freedom – an example is shown in Fig. 2.1(b). In such cases, multi-dimensional interferograms are produced by sampling the corresponding delay parameters.

Remark 2. *The applicability of this two-path interferometry framework is by no means restricted to deterministic (periodic) signals, but applies naturally to stochastic signals as well, by virtue of the linearity inherent in the superposition of fields at the output. The only modification required would be replacing the time-average by an expectation over random field realizations. In the case of ergodic stochastic signals, this expectation can be carried out by averaging over a period of time larger than the 'coherence time' that is proportional to the inverse of the bandwidth of the power spectral density, as known from the Wiener-Khinchtine theorem [75].*

Examples and representative applications

• **Interferometry-based optical modal analysis:** This example concerns analyzing an optical field into its constituent modes via the interferometric configuration in Fig. 3.2(a). The goal is to reconstruct the modal energies $|c_n|^2, n = 1, \ldots, N$ of an optical field represented in a finite basis as $\psi(x) = \sum_{n=1}^{N} c_n \phi_n(x)$. In optical spectroscopy, where x is the time variable t, the goal is to analyze a pulsed field into its temporal modes. Hence, $\psi(t)$ enters a two-path optical interferometer such as a Mach-Zehnder interferometer (MZI), and a delay τ is swept. The input field passes through the sample arm without undergoing any change where $h_2(t) = \delta(t)$, thus $\psi_2(t) = \psi(t)$. Normalizing the energy to unity $\sum_{n=1}^{N} |c_n|^2 = 1$, the interferometric measurements are $y(\tau_m) = \sum_{n=1}^{N} |c_n|^2 \cos(\omega_n \tau_m)$, $m = 1, 2, ..., M$. Hence, given these M measurements, the $M \times 1$ measurement vector $\mathbf{y}$ with entries $y(\tau_m)$ fits the

linear model in (3.12) for a modal coefficient vector $\mathbf{x} = [|c_1|^2|c_2|^2 \dots |c_N|^2]^{\mathrm{T}}$ and an $M \times N$ matrix $\mathbf{A} = [\cos(\omega_n \tau_m)]$. Revealing the spectrum of the optical field thus amounts to solving a system of linear equations.

As a case study for optical modal analysis in an arbitrary domain, we show how to leverage the proposed interferometry framework to decompose an optical field in the Hilbert space spanned by the Hermite-Gaussian (HG) beams, which are natural modes of laser resonators [76]. Consider an optical field $\psi(x)$ consisting of a superposition of HG modes. To analyze the field into its constituent modes, the reference arm should include a frFT of order α since the HG modes are eigenfunctions of the frFT with eigenvalues $e^{-jn\alpha}$ [63]. The kernel of an frFT system of order α is,

$$h_1(x, x'; \alpha) \propto \exp\left\{\frac{j\pi}{2}(x^2 \cot\alpha + x'^2 \cot\alpha - 2xx' \csc\alpha)\right\}, \tag{3.13}$$

whose optical implementation makes use of two cylindrical lenses, and three Spatial Light Modulators (SLMs) as the phase operator components [37, 15]; here x and x' are appropriately normalized spatial coordinates. Figure 3.3 depicts an actual implementation of a frFT filter using a three-SLM configuration used to analyze an input beam into its HG modes. We refer the reader to [15] for further details.

The output from the frFT is superposed with the output of the sample arm $\psi(x)$ to acquire the interferometric measurements. Considering (3.11), the interferogram can again be cast as $\mathbf{y} = \mathbf{A}\mathbf{x}$, where $\mathbf{x}^T = [|c_1|^2|c_2|^2 ... |c_N|^2]$, and $\mathbf{A} = [\cos(n\alpha_m)]$, $n = 1, 2, ..., N$, and $m = 1, 2, ..., M$. Thus, we have shown that optical modal analysis where we seek to recover information about the input signal is a special case of the unifying framework proposed. Specifically, in the modal analysis example $d_n = c_n$ ($\theta_n = 0$) for $n = 1, 2, ..., N$, $\mathbf{A} = \mathbf{A}_1$, and $\mathbf{x} = \mathbf{x}_1$ in (3.12).

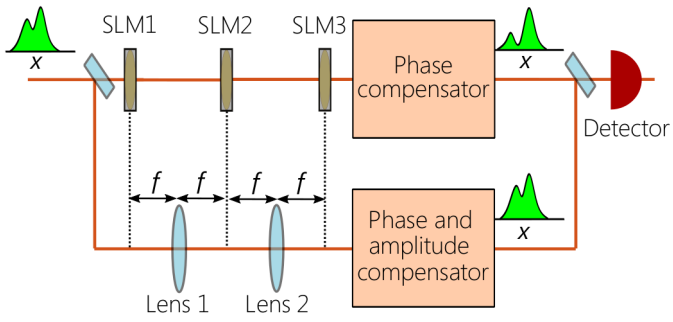

Figure 3.3: Schematic of a frFT filter implemented using SLMs that act as quadratic phase operators.

• **Time-Domain OCT (TD-OCT):** OCT makes use of a low-coherence (large-bandwidth) optical source in a two-path interferometer, as illustrated in Fig. 2.1(a). If the spectrum of this source is $s(\omega)$, we discretize it and obtain the coefficients $c_n = s(\omega_n)$. A layered sample is placed in the sample arm, a delay is swept in the reference arm, and the time-averaged energy of the superposed signal is recorded for each delay to reconstruct the layered sample. Hence, this is an example of interferometry where we seek to recover information about the sample impulse response $h_2(t)$ (see Fig. 3.2(b)). We model the (typically reflective) layered sample by a linear time invariant impulse response $h_2(t) = \sum_{\ell=1}^{L} r_\ell \delta(t - T_\ell)$, which is parametrized by the round-trip time T_ℓ for the field to travel from the ℓ^{th} sample layer to the sample surface, and r_ℓ is the field reflectivity of the ℓ^{th} layer. Accordingly, the output from the sample arm is characterized by the coefficients $d_n = c_n \sum_{\ell=1}^{L} r_\ell e^{-j\omega_n T_\ell}, n = 1, 2, \ldots, N$. Assuming that the source is well-characterized (i.e., the coefficients c_n are known), then our linear model retrieves the coefficients d_n.

• **Localization in wireless networks:** A related example is that of localization in wireless sensor networks shown in Fig. 2.1(c). Consider two anchor nodes each transmitting a sinusoid with distinct frequencies ω_1 and ω_2. The transmitted signals $\psi_k(t) = a_k e^{j\omega_k t}$, $k = 1, 2$, superpose at the receiver to produce the signal $\psi_s(t) = \psi_1(t - d_1/c) + \psi_2(t - d_2/c)$, where d_1

and d_2 are the distances between the receiver and the anchor nodes, and c is the speed of light in vacuum (a schematic of this system is shown in Fig. 3.2(c)). In contrast to standard interferometry, in this case we have no control over the relative delay of the two paths. Instead, the received signal is sampled at different time instants to recover the distances. Although this problem cannot be viewed as one of basis analysis, by sampling M points corresponding to sampling instances $T_m, m = 1, \ldots, M$, we obtain linear measurements $\mathbf{y} = \mathbf{A'x}$, where $\mathbf{x} = \left[|a_1||a_2|\cos(\frac{\omega_2 d_2 - \omega_1 d_1}{c}) \quad |a_1||a_2|\sin(\frac{\omega_2 d_2 - \omega_1 d_1}{c})\right]^T$ and the matrix $\mathbf{A'}$ has dimensions $M \times 2$, with the entries in each row being $\cos((\omega_1 - \omega_2)T_m)$ and $-\sin((\omega_1 - \omega_2)T_m)$. This can be easily generalized to multiple receiving nodes.

• **Radio Interferometry:** In this application, an array of radio telescopes is used to measure the spatial coherence of the electric fields to obtain a clear image of the sky brightness [47, 48]. The field intensity $I(x, y) = E(x, y) \times E^*(x, y)$, x and y being the space coordinates and E the complex electric field, is recovered from samples of the coherence function called visibilities [50]. This configuration is a special case of the generalized interferometer considered herein in the sense that the complex exponentials (forming a basis) are eigenfunctions of the existing time delay operator due to free-space propagation between the astronomical objects and the radio telescopes, with the field intensity obtained as the expansion coefficients in this basis.

CHAPTER 4: SIGNAL RECONSTRUCTION FROM INTERFEROMETRIC MEASUREMENTS UNDER SENSING CONSTRAINTS

Based on the generalized framework introduced in the previous chapter which works for arbitrary basis, an FT of the interferometric measurements can be used to recover the the information of interest. However, we established that the interferogram relates to the Hilbert space coefficients via a linear operator (of known structure) defined by the parameters of the interferometer. Based on this linear model in this chapter[1], we show that signal reconstruction from interferometric measurements is amenable to compressive data acquisition. Specifically, reconstruction can be carried out using a reduced number of measurements despite the constrained structure of matrix $\mathbf{A}$ provided $\mathbf{x}$ admits some additional structure. This is particularly useful for scenarios where measurements are costly, as well as in delay-sensitive applications. We seek reconstruction of $\mathbf{x}$ from $M \ll N$ interferometric measurements corresponding to M settings of the interferometric delay parameter α.

We point out two fundamental differences between our approach and prior work employing compressive techniques. First, the vast majority of prior work on compressive sensing presumes one has full control over the design of the sensing matrix – for example, in optics, by introducing designed random masks along the path of an optical field in an imaging system [7, 24, 77]. In sharp contrast, the matrix $\mathbf{A}$ in our interferometric formulation is imposed through the structure of the interferometer itself. Therefore, compression has to be carried out under sensing constraints set by the limited degrees of freedom of the sensing system. It is not clear at the outset whether performance guarantees on reconstruction can

[1]In this chapter, we use the material published in Signal Processing, 2019 [8].

be established given the special structure of the constrained matrix $\mathbf{A}$. Second, previous work on using compressive sensing in optical interferometry has mostly focused on reducing the number of measurements used for recovery/reconstruction, but not on compressive data acquisition. For example, in the context of OCT, the approach in [38, 78] selects a random subset of many interferometric measurements collected using a CCD array detector. This amounts to using fewer measurements in the recovery of depth information and discarding measurements already collected by the physical sensing system. By contrast, our approach directly uses the degrees of freedom inherent to the sensing system (by assigning some random values to the generalized phase α) to reduce the data acquired in the first place for subsequent recovery.

Constrained sensing

Sub-Gaussian random sensing matrices satisfy the RIP with high probability for $M \approx \mathcal{O}(s \log N)$, which motivated their use in several CS applications. However, in practice one may not have full control over the design of the sensing matrix $\mathbf{A}$ as it is normally determined by the structure of the data acquisition system (DAQ). Here, we show that CS can be exploited in 'native' interferometry, that is, without modifying the underlying interferometer structure nor introducing additional components. Recalling that the rows of the sensing matrix $\mathbf{A}$ have the α-dependent structure $\mathbf{a}_m = [\mathbf{a}_{m1} \ \mathbf{a}_{m2}], \ m = 1, 2, ..., M$ where $\mathbf{a}_{m1}^{\mathrm{T}} = [\cos(n\alpha_m)], \ \mathbf{a}_{m2}^{\mathrm{T}} = [-\sin(n\alpha_m)]$, $\mathbf{A}$ has only few degrees of freedom corresponding to the settings of the delay parameter α. Next section of this chapter focuses on signal reconstruction based on compressive interferometric measurements of the form (3.12) and establishing performance guarantees thereof.

Guarantees with randomized delays

Collecting informative interferometric measurements (3.12), and in turn achieving better performance in reconstruction, is premised on selecting appropriate values for the generalized delay parameter α. We consider sensing matrices generated by drawing generalized delays from random distributions.

Throughout this section, we consider normalized interferometric measurements $\mathbf{y} = \hat{\mathbf{A}}\mathbf{x}$, where $\hat{\mathbf{A}} = \sqrt{2/M}\mathbf{A}$ and $\mathbf{A}$ the original matrix defined in (3.12). Our next theorem establishes that the matrix $\hat{\mathbf{A}}$ is RIP provided the generalized delay parameters are selected from an appropriate distribution.

Theorem 1. *If the generalized delay parameters α_m, $m = 1, 2, \ldots, M$, of the matrix $\mathbf{A}$ in (3.12) are chosen independently at random from the uniform distribution $\mathcal{U}[0, 2\pi]$, then there exist positive constants c_1, c_2 such that $\hat{\mathbf{A}} := \sqrt{2/M}\mathbf{A}$ satisfies the RIP with respect to all s-sparse vectors with any $s \leq c_1 M/\log(2N/s)$, and an RIP constant $0 < \delta < 1$ with probability greater than $1 - 2e^{-c_2 M}$, where $c_2 \leq c_0(\delta/2) - c_1[1 + (1 + \log(12/\delta))/\log(2N/s)]$.*

Proof. Following the procedure in [79], it suffices to show that $\hat{\mathbf{A}}$ satisfies the concentration inequality $\mathbb{P}\{|\|\hat{\mathbf{A}}\mathbf{x}\|^2 - \|\mathbf{x}\|^2| \geq \epsilon\|\mathbf{x}\|^2\} \leq 2e^{-Mc_0(\epsilon)}$, $0 < \epsilon < 1$ for all $\mathbf{x} \in \Sigma_s$ under the condition in the statement of Theorem 1. Since the M realizations $\alpha_m, m = 1, \ldots, M$, are selected independently from a random uniform distribution $\mathcal{U}[0, 2\pi]$, $\|\hat{\mathbf{A}}\mathbf{x}\|^2$ can be written as a sum of M i.i.d. random variables $\|\hat{\mathbf{A}}\mathbf{x}\|^2 = \sum_{m=1}^{M} |\langle \hat{\mathbf{a}}_m, \mathbf{x}\rangle|^2$, $\forall \mathbf{x} \in \Sigma_s$, where $\langle ., . \rangle$ denotes the inner product of its two vectors argument. Assuming a fixed but arbitrary vector $\mathbf{x}_0 \in \Sigma_s$, each random variable $Z_m \triangleq |<\hat{\mathbf{a}}_m, \mathbf{x}_0>|^2$ can be bounded as $Z_m \triangleq |<\hat{\mathbf{a}}_m, \mathbf{x}_0>|^2 \leq \|\hat{\mathbf{a}}_m\|^2 \cdot \|\mathbf{x}_0\|^2 \leq \frac{2s}{M}\|\mathbf{x}_0\|^2$, $m = 1, 2, \ldots, M$, using the Cauchy-Schwarz inequality [80]. Hence, the random variable $\|\hat{\mathbf{A}}\mathbf{x}_0\|^2$ is a summation of M bounded random variables $Z_m \in [0, \frac{2s}{M}\|\mathbf{x}_0\|^2]$.

Accordingly, using Hoeffding's inequality [81] we have $\mathbb{P}\{|\|\hat{\mathbf{A}}\mathbf{x}_0\|^2 - \mathbb{E}\|\hat{\mathbf{A}}\mathbf{x}_0\|^2| \geq \epsilon\|\mathbf{x}_0\|^2\} \leq 2e^{-\frac{2\epsilon^2\|\mathbf{x}_0\|^4}{\frac{4s^2}{M}\|\mathbf{x}_0\|^4}} = 2e^{-M\frac{\epsilon^2}{2s^2}}$, $0 < \epsilon < 1$. Given the distribution of α, $\mathbb{E}\|\hat{\mathbf{A}}\mathbf{x}\|^2 = \|\mathbf{x}\|^2$ for all $\mathbf{x} \in \Sigma_s$. Thus, we can rewrite this probability bound as, $\mathbb{P}\{|\|\hat{\mathbf{A}}\mathbf{x}\|^2 - \|\mathbf{x}\|^2| \geq \epsilon\|\mathbf{x}\|^2\} \leq 2e^{-Mc_0(\epsilon)}$, $0 < \epsilon < 1$, $\forall\ \mathbf{x} \in \Sigma_s$, where $c_0(\epsilon) = \epsilon^2/2s^2$. Hence, it follows from [79, Theorem 5.2] that the matrix $\hat{\mathbf{A}}$ is RIP with respect to all $\mathbf{x} \in \Sigma_s$ with RIP constant $0 < \delta < 1$, with probability greater than $1 - 2e^{-c_2 M}$, where $c_2 \leq c_0(\delta/2) - c_1[1 + (1 + \log(12/\delta))/\log(2N/s)]$. □

Based on Theorem 1, $\hat{\mathbf{A}}$ satisfies the RIP with higher probability as the number of measurements M increases. The next corollary identifies an asymptotic regime where the sensing matrix satisfies the RIP with probability 1.

Corollary 1. *The sensing matrix $\hat{\mathbf{A}}$ defined in Theorem 1 satisfies the RIP with a constant $0 < \delta < 1$ for all s-sparse vectors with probability 1, if $N, M \to \infty$ and $M = \omega\left(\frac{s}{c_0(\delta/2)}\log(\frac{24eN}{\delta s})\right)$*[2].

Proof. The proof follows directly from the fact that c_2 is always a positive constant, so $\lim_{M\to\infty} -c_2 M = -\infty$ given the asymptotic order of M in the statement of the corollary. Therefore, the probability $1 - 2e^{-c_2 M} \to 1$. □

The results of Theorem 1 and Corollary 1 are general in that they apply to every problem in interferometry with the measurement model in (3.12). We have already established the generality of the framework that gave rise to (3.12), which was also shown to be basis-neutral. As a direct application of this result, the following corollary establishes that the matrix arising in optical modal analysis, where $\mathbf{A} = \mathbf{A}_1$, and $\mathbf{x} = \mathbf{x}_1$, is also RIP.

[2]The notation $f(n) = \omega(g(n))$ means that $f(n)$ dominates $g(n)$ asymptotically, i.e., $\lim_{n\to\infty} \frac{f(n)}{g(n)} = \infty$.

Corollary 2. *Given* $0 < \delta < 1$ *and* $s \leq c_1 M/\log(N/s)$*, the sensing matrix* $\hat{\mathbf{A}} = [\sqrt{2/M}\cos(n\alpha_m)]$ *arising in the (generalized) optical modal analysis example (which consists of only the cosine terms), is RIP with respect to all s-sparse vectors in* $\mathbb{R}^N$ *with probability greater than* $1 - 2e^{-c_2 M}$*, where* $c_2 \leq c_0(\delta/2) - c_1[1 + (1 + \log(12/\delta))/\log(N/s)]$.

The proof follows directly from Theorem 1.

Theorem 1 established a lower bound on the probability that $\hat{\mathbf{A}}$ is RIP, which goes asymptotically to 1 per Corollary 1. In non-asymptotic regimes and when the number of measurements is not sufficiently large, this bound can be fairly far from 1. It turns out that the constrained matrix $\mathbf{A}$ also satisfies some weaker sufficient conditions for recoverability when the generalized delay parameters are drawn uniformly at random. We establish that the ensemble of sensing matrices corresponding to α's drawn from a uniform distribution $\mathcal{U}[0, 2\pi]$ is isotropic and incoherent [44], therefore an arbitrary fixed sparse vector $\mathbf{x}$ can be reconstructed from compressive measurements with high probability [44].

We can readily state the following lemma which establishes sufficient conditions for successful reconstruction from interferometric measurements based on the generalized interferometry framework.

Lemma 1. *Suppose* M *interferometric measurements are acquired by selecting the generalized delay parameters* $\alpha_m, m = 1, 2, \ldots, M$*, from a uniform distribution* $\mathcal{U}[0, 2\pi]$*. If* $M \geq 2L_0(1 + \beta)s\log(2N)$ *for a positive constant* L_0 *and any* $\beta > 0$*, the* ℓ_1*-norm minimization in (2.3) yields the s-sparse vector* $\mathbf{x} \in \mathbb{R}^N$ *from the normalized measurements* $\mathbf{y} = \hat{\mathbf{A}}\mathbf{x}$ *with probability at least* $1 - \frac{5}{2N} - e^{-\beta}$.

Proof. Based on [44, Theorem 1.1], we only need to show that $\sqrt{M}\,\hat{\mathbf{A}}$ is incoherent and isotropic under the conditions in the statement of Lemma 1. It is easy to see that for the

matrix $\hat{\mathbf{A}}$, $\max_{n=1,2,\ldots,2N} |\hat{a}_{m,n}|^2 \leq 2/M$, as the cosine and sine terms are bounded below and above by -1 and 1, respectively. So, the matrix $\sqrt{M}\,\hat{\mathbf{A}}$ is incoherent with parameter $\mu = 2$. Also, if $\alpha_m \sim \mathcal{U}[0, 2\pi]$, then $\mathbb{E}[\hat{\mathbf{a}}_m^H \hat{\mathbf{a}}_m] = (1/M)\,\mathbf{I}$, therefore $\sqrt{M}\,\hat{\mathbf{A}}$ is isotropic. Accordingly, Lemma 1 follows from [44, Theorem 1.1]. □

We also consider the noisy case $\mathbf{y} = \hat{\mathbf{A}}\mathbf{x} + \mathbf{z}$, where $\mathbf{z} \sim \mathcal{N}(0, \sigma^2 I)$ and $\mathbf{x}$ an arbitrary vector (not necessarily sparse). The following lemma provides a sufficient condition on the number of measurements for stable recovery.

Lemma 2. *Consider the same setting in the statement of Lemma 1. For any $\beta > 0$, if the number of noisy measurements $M \geq L_0.(1+\beta).2.s\log(2N)$, then the LASSO algorithm [73] with parameter $\lambda_{LASSO} = 10\sqrt{\log(2N)}$ yields a vector $\bar{\mathbf{x}}$ satisfying*

$$\|\bar{\mathbf{x}} - \mathbf{x}\|_2 \leq \min_{1 \leq \bar{s} \leq s} \zeta(\bar{s}), \tag{4.1}$$

where $\zeta(\bar{s}) \triangleq L(1+\gamma)\Big(\frac{\|\mathbf{x}-\mathbf{x}_{\bar{s}}\|_1}{\sqrt{\bar{s}}} + \sigma\sqrt{\bar{s}\log(2N)}\Big)$ with probability at least $1 - 6/(2N) - 6e^{-\beta}$, where L is a positive constant, $\gamma = \sqrt{\frac{(1+\beta)2\bar{s}\log(2N)\log M \log^2 \bar{s}}{M}}$, and $\mathbf{x}_s$ is the s-sparse approximation of $\mathbf{x}$ obtained by keeping the s largest entries of $\mathbf{x}$ and setting all other entries to zero.

Proof. Similar to the proof of Lemma 1, Lemma 2 follows from the incoherence and isotropy of $\sqrt{M}\,\hat{\mathbf{A}}$ and the results of Theorem 1.2 and 1.3 in [44]. □

Instead of LASSO, we can use the Dantzig selector [70] to recover the sparse vector in noise. In this case, the performance bound in (4.1) is still valid by replacing γ with γ^2 [44].

Simulation and experimental results

In this section, we study two different examples to evaluate the performance of the proposed approach to signal reconstruction from interferometric measurements under sensing constraints. First, we consider the optical modal analysis problem with one and two spatial degrees of freedom (1D and 2D optical modal analysis). Second, we reconstruct information regarding a layered sample object placed in one arm of the interferometer in TD-OCT.

Optical modal analysis

Analyzing a light beam based on HG modes: As discussed earlier, the HG modes are the eigenfunctions of an frFT of order α with eigenvalues $e^{-jn\alpha},\ n = 1, 2, ..., N$. To analyze an optical beam in a Hilbert space spanned by the HG modes, we collect M interferometric measurements by selecting M different frFT orders $\alpha_m,\ m = 1, 2, ..., M$, then apply a CS reconstruction method to reveal the modal content of the beam (the modal energies). In this case, $\mathbf{y} = \mathbf{A}\mathbf{x}$, where the $M \times N$ matrix $\mathbf{A} = [\cos(n\alpha_m)]$ and $\mathbf{x}^{\mathrm{T}} = [|c_1|^2|c_2|^2...|c_N|^2]$ is s-sparse. The frFT orders $\alpha_m,\ m = 1, 2, ..., M$, specifying the rows of $\mathbf{A}$ are i.i.d. and drawn from a uniform distribution $\mathcal{U}[0, 2\pi]$, thus $\mathbf{A}$ is isotropic and incoherent. In this experiment, $N = 64$ and $s = 4$ (modes HG_{25}, HG_{32}, HG_{38}, and HG_{60}, where HG_n is n^{th} Hermite-Gaussian mode). In presence of noise, $\mathbf{y} = \mathbf{A}\mathbf{x}+\mathbf{z}$, where the noise $\mathbf{z} \sim \mathcal{N}(0, \sigma^2\mathbf{I})$ is white and Gaussian, and $\mathrm{SNR} \triangleq 10\log(\frac{\mathbf{x}^{\mathrm{H}}\mathbb{E}[\mathbf{A}^{\mathrm{H}}\mathbf{A}]\mathbf{x}}{\sigma^2})$, where $\mathbb{E}[.]$ denotes the expectation over the distribution of α_m parametrizing $\mathbf{A}$. To evaluate the quality of reconstruction, the scaled recovery error is defined as $e \triangleq \frac{\|\mathbf{x}-\bar{\mathbf{x}}\|_2^2}{\|\mathbf{x}\|_2^2}$. We use the BP and the Dantzig selector algorithms to reconstruct the modal coefficients in noise-free and noisy environments, respectively.

We first assume an ideal implementation for the frFT of different orders. Accordingly, for

order α_m, the output beam is $\psi_1(x;\alpha_m) = \sum_{n=1}^{N} c_n \phi_n(x) e^{-jn\alpha_m}$, where $\alpha_m,\ m = 1, 2, ..., M$ are selected independently and identically from the uniform distribution $\mathcal{U}[0, 2\pi]$.

Based on the generalized framework introduced in the previous chapter which works for arbitrary basis, an FT of the interferometric measurements can be used to recover the modal energies of the input beam. Since the largest mode order is $N = 64$, sampling uniformly at the Nyquist rate amounts to collecting $2N = 128$ measurements by selecting the orders of the frFT uniformly and deterministically between 0 and 2π. In this case, $\bar{\mathbf{x}} = |\mathbf{F}\mathbf{y}|$, where $\mathbf{F}$ is a $2N \times 2N$ DFT matrix. While in the FT approach $M = 2N = 128$ interferometric measurements are needed for successful recovery, Fig. 4.1 shows that the modal content can be retrieved with significantly less measurements with the CS approach. Despite the constrained structure of $\mathbf{A}$, from only $M = 25$ measurements the CS approach yields performance comparable to that of FT whilst achieving substantial savings in data acquisition time.

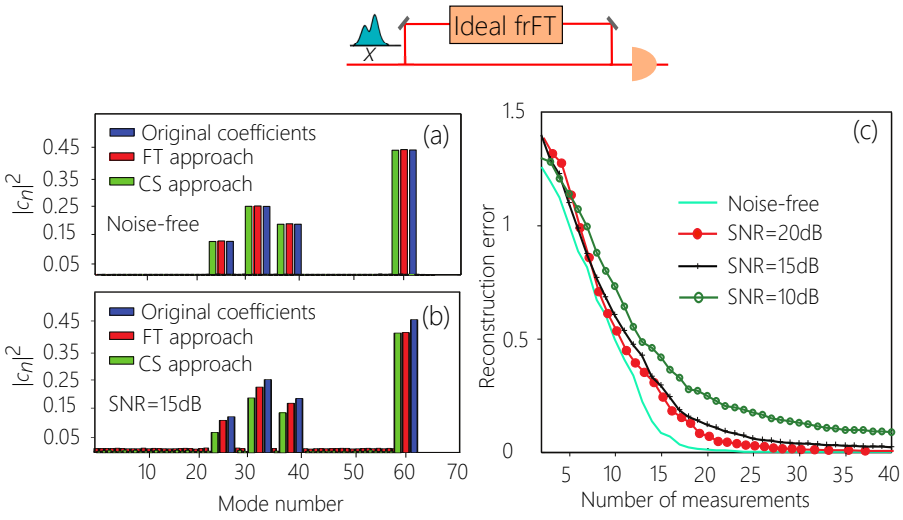

Figure 4.1: (a) Comparing the CS approach with $M = 25$ to the FT approach with $2N = 128$ measurements in the noise-free case, (b) comparison at SNR= 15dB, (c) reconstruction error of the CS approach versus M for different SNRs.

We investigate the recovery/reconstruction performance by calculating the reconstruction error for a different number of measurements in both noise-free and noisy settings. Fig. 4.1(c) shows the decay of the reconstruction error with M using the compressive approach.

Here, we also report on results from an actual laboratory experiment implementing the frFT filter. Producing exact HG modes is practically infeasible. Instead, we obtain approximate modes shown in the insets of Fig. 4.2. Obviously, such beams are not perfectly orthogonal, hence will have non-vanishing mutual projections. As such, even if a single mode is active, there will be non-zero coefficients for the adjacent modes.

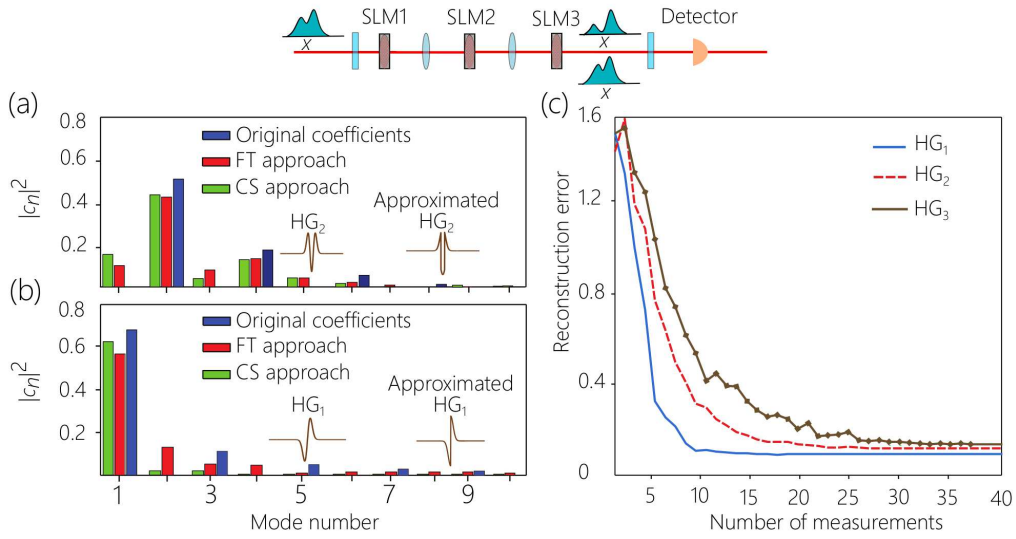

Figure 4.2: Comparing the reconstruction performance of the CS approach to that of the FT from experimental measurements. (a) Using approximate HG_1 mode. (b) Using approximate HG_2 mode. (c) Evaluating the performance of the CS approach in the experiment using approximate HG_1, HG_2, and HG_3 in terms of reconstruction error versus the number of interferometric measurements.

In Fig. 4.2(a) and (b), we compare the performance of the CS approach to that of FT for an

optical beam consisting of HG_1 and another of HG_2, where HG_1 and HG_2 are the first and second Hermite-Gaussian modes, respectively. The FT approach uses 128 interferometric measurements collected uniformly by choosing the generalized delays between 0 to 2π. In the CS approach, only $M = 25$ random measurements are used.

We also investigate the reconstruction error based on the experimental results. As shown in Fig. 4.2(c), efficient reconstruction requires about $M = 25$ measurements. This corresponds to 25 settings of the frFT order for the CS approach versus 128 for FT.

Multi-dimensional interferometry: The proposed interferometry framework can be extended to problems with more than one degree of freedom where several generalized delay systems are used corresponding to different degrees of freedom. In this example, we consider a signal $E(x, y) = \sum_{nm} c_{nm}\phi_n(x)\eta_m(y)$, where $\{\phi_n(x)\}$ and $\{\eta_m(y)\}$ are two sets of HG basis elements and c_{nm} are real and positive expansion coefficients.

We implement two generalized delays, namely two cascaded frFT systems of orders α_1 and α_2. For $N = 100$ basis elements, we examine the performance of our approach in reconstructing signals formed by the superposition of a small number s of basis elements. Rows (a) and (b) of Fig. 4.3 display the 2D signals and the reconstructed coefficient(s) for $s = 1$ and $s = 4$, respectively. Our approach is shown to yield accurate reconstruction of the expansion coefficients from a small number of interferometric measurements $M = 50$, a saving of 75% in sample complexity compared to directly taking a FT of the resulting interferogram. This example underscores the ability of the proposed approach to handle spatially-multiplexed signals commonly used, for example, in high-speed communications.

Orbital Angular Momentum (OAM) beams (modes) $\{\phi_n(x) = e^{jnx}\},\ n = 1, 2..., N$ form another orthonormal spatial basis in which the degree of freedom x is the angle measured in the transverse plane perpendicular to the direction of propagation (instead of time). To

analyze an optical beam into its OAM modes, the authors in [54, 37] use a rotator in one arm of an MZI interferometer. This is tantamount to replacing the delay element with an operator $h_1(x, x'; \theta) = \delta(x - x' - \theta)$ with spatial rotation θ for which the OAM modes are indeed eigenfunctions. Other examples of modal bases include the radial Laguerre-Gaussian (LG) modes $\{L_p^{|\ell|}(x)\}_p$ with order p and parameter ℓ, and the one-dimensional Hermite-Gaussian (HG) modes $\{\phi_n(x)\}_n$.

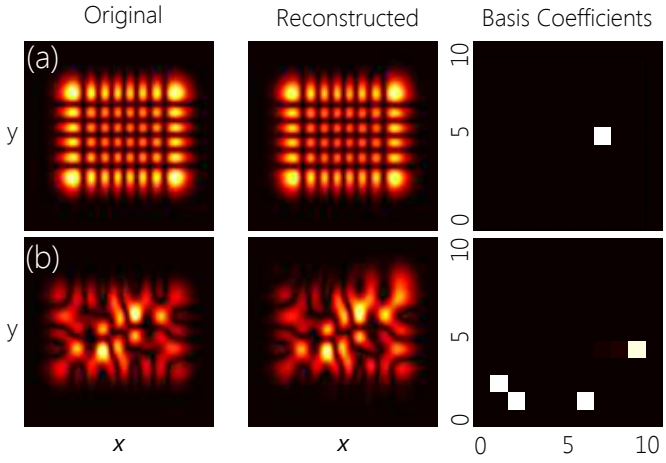

Figure 4.3: Reconstruction of 2D HG signals (described by two spatial degrees of freedom) from compressive interferometric measurements. (a) (left) Original signal $\text{HG}_{57} = \phi_5(x)\eta_7(y)$ i.e, $(m, n) = (5, 7)$, (middle) reconstructed signal and (right) reconstructed coefficient c_{57}. (b) (left) Original 2D signal formed by the superposition of the, $s = 4$, 2D HG basis elements $(1, 2), (2, 1), (6, 1), (9, 4)$, (middle) reconstructed signal, and (right) reconstructed coefficients.

We present another multi-dimensional modal analysis example in which the input signal is represented as a superposition of LG-OAM modes with radial and angular degrees of freedom, respectively. In this example, we consider the input signal $E(x, y) = \sum_{np} c_{np}\phi_n(x)L_p^{|\ell|}(y)$, where $\{\phi_n(x)\}$ and $\{L_p^{|\ell|}(y)\}$ are OAM and LG basis elements, respectively. As seen in Fig. 4.4(a), the incident beam is formed from $s = 4$ active LG-OAM modes (3,3), (4,5), (5,1),

(6,2). Since the interferometric measurements follow the derived linear model, we use CS recovery algorithms to reveal the modal content of the optical beam. Figure 4.4(c) shows the reconstruction error versus the number of interferometric measurements.

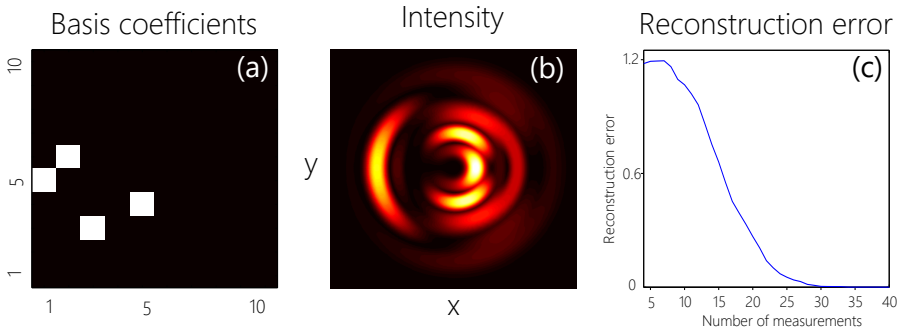

Figure 4.4: Multi-dimensional modal analysis based on LG-OAM modes. (a) Active modal coefficients. (b) Intensity of the beam. (c) Reconstruction error versus number of interferometric measurements.

Modal analysis with larger number of modes: To evaluate the performance of the proposed compressive recovery approach with a larger number of potential and active modes, we analyze a light beam with $N = 128$, and $s = 10$ or $s = 15$. We use BP to reconstruct the modal content in the noise-free scenario and the Dantzig selector in a noisy scenario with SNR= 20dB. Figure 4.5 shows the decrease in the reconstruction error as we increase the number of measurements using the compressive interferometry approach for both sparsity levels for the noise-free and noisy scenarios, underscoring the applicability of the proposed approach to problems of larger size.

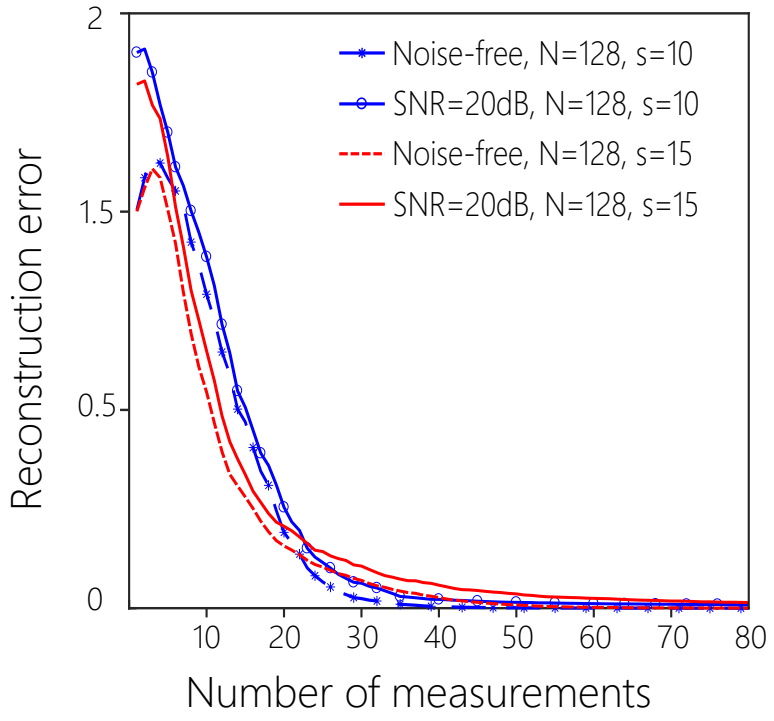

Figure 4.5: Evaluating the performance of the compressive approach for ambient dimension $N = 128$, and number of non-zero elements $s = 10$, $s = 15$.

Information recovery in TD-OCT

Here, we present an example of TD-OCT in which we seek to recover the reflectivity and depth information of L different layers of a sample object within our unifying interferometry framework. The desired information here is in the basis coefficients d_n, $n = 1, 2, ..., N$, which can be retrieved by solving the system of linear equations in (3.12). In this experiment, we first consider a sample object with $L = 10$ layers. By solving (3.12), we reconstruct the 20×1 vector $\mathbf{x}$ depicted in Fig. 4.6(a), which is shown to match the ground truth. Subsequently, the reflectivity of the layers and their depths are correctly reconstructed from the retrieved coefficients d_n as displayed in Fig. 4.6(b).

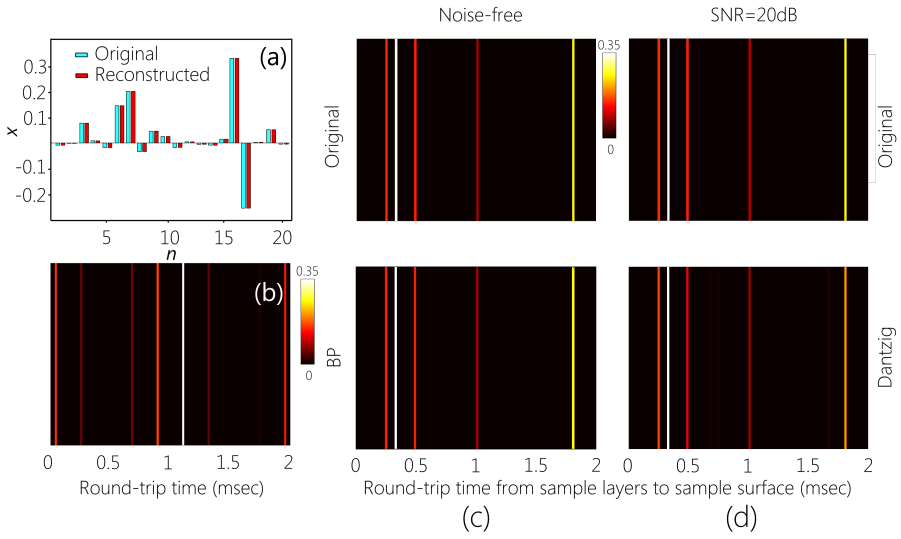

Figure 4.6: Reconstructing the depth information of a sample object in TD-OCT using the unifying interferometry framework. (a) Entries of the reconstructed vector $\mathbf{x}$ in (3.12). (b) Reconstructed reflectivity and depth information for the layers of the sample object. (c) Reconstructing the reflectivity indices of a sample object with $L = 100$ layers and $s = 5$ reflective layers from compressed interferometric measurements using BP and Dantzig selector, Noise-free case. (d) Noisy setting with SNR $= 20$ dB.

We consider a second example of OCT where the sample object has $L = 100$ layers among which only $s = 5$ unknown layers have non-zero reflectivity. The sparsity of the vector of reflectivity indices enables recovery from few measurements. The reflectivity coefficients are successfully retrieved using Basis Pursuit and the Dantzig selector from $M = 60$ interferometric measurements as shown in Fig. 4.6(c) and (d) for noise-free and noisy settings (SNR $= 20$ dB). We remark that recovery using BP or the Dantzing selector is by no means exclusive. Since the established RIP, and isotropy and incoherence conditions are fairly strong criteria, they can generally guarantee successful reconstruction using other algorithms such as LASSO [73]. Depending on the ambient dimension and the sparsity rate,

more accurate recovery may also be achievable by directly minimizing the ℓ_0-norm using techniques such as in [82]. Optimizing over the choice of reconstruction algorithms, however, is not the main focus of our work.

CHAPTER 5: CONTROLLED AND SEQUENTIAL SAMPLING

Introduction

In the previous chapter, we have shown both theoretically and experimentally that the sparse signal of interest can be successfully reconstructed from the interferometric measurements collected by selecting a random set of generalized delays from an appropriate distribution. We established that despite the limited number of degrees of freedom of the sampling system, the resulting structured and random sensing matrix satisfies some sufficient conditions for a successful recovery. However, the *unknown* statistical model of the sampling error or noise capturing the imperfect functionality of sensing systems is another prohibit factor in reconstructing the sparse vector under the sensing constraints in a noisy environment. When prior knowledge about the noise distribution or its variance is at our disposal, standard de-noising reconstruction algorithms such as LASSO [73] and the Dantzig selector [70] can provably stably recover a sparse signal from noisy measurements under some sufficient conditions on the sensing matrix [67, 44]. In this chapter[1], we consider reconstruction under sensing constraints when the noise statistics are completely unknown.

To account for the aforementioned limitations of sensing systems, we seek efficient means to collect informative measurements. In other words, we focus on improving the quality of the sensing matrix (hence the quality of measurements) through proper control of the degrees of freedom of the sensing system rather than searching for more effective reconstruction algorithms. To this end, we propose two controlled sampling algorithms for collecting informative measurements under constrained sensing structures. It is shown that the pro-

[1]In this chapter, we use the material presented in Allerton Conference on Communication, Control, and Computing, 2016 [12].

posed algorithms yield notable reductions in the required number of measurements while dispensing with the usual de-noising requirements.

Despite these gains in sample complexity, the number of measurements has to be chosen based on a worst case analysis if collected in a batch in order to meet a pre-determined performance requirement. To address this issue, we develop a sequential approach in which the controller stops collecting measurements as soon as there is enough confidence about the performance of reconstruction. The stopping rule leverages a reconstruction error estimator from [83]. Given a target performance in reconstruction, it is shown that the sequential controlled approach yields substantial gains in sample complexity. The proposed algorithms are remarkably general in the sense that they can be adopted to improve the quality of reconstruction in wide range of practical applications beyond the specific interferometry problem studied in the previous chapter.

In this chapter, we first propose two controlled sampling strategies along with a sequential approach to select the sampling parameters of an arbitrary data acquisition system whose corresponding sensing matrix is structured. We then show how the proposed controlled sampling algorithms can be adopted to improve the quality of reconstruction in an interferometry problem.

Problem Setup

We consider reconstructing a sparse vector from compressive noisy measurements under sensing constraints. The measurements follow the linear model,

$$\mathbf{y} = \mathbf{A}\mathbf{x} + \mathbf{n}, \tag{5.1}$$

where $\mathbf{y}$ is an $M \times 1$ vector of compressive measurements, $\mathbf{x}$ an $N \times 1$ sparse vector with at most s non-zero elements, and $\mathbf{n}$ an $M \times 1$ noise vector. Traditionally, the sensing matrix $\mathbf{A}$ is *designed* from sub-Gaussian random ensembles, under which reconstruction is guaranteed with high probability. Instead, we consider reconstruction with a constrained sensing matrix $\mathbf{A}$ and a sampling noise vector $\mathbf{n}$ with unknown statistics. The constrained sensing system defines the structure of the sensing matrix. In particular, we assume that the sensing matrix $\mathbf{A}$ takes the form,

$$\mathbf{A} = \begin{bmatrix} \mathbf{a}_1 \\ \mathbf{a}_2 \\ \vdots \\ \mathbf{a}_M \end{bmatrix} = \begin{bmatrix} \mathbf{f}(\alpha_1) \\ \mathbf{f}(\alpha_2) \\ \vdots \\ \mathbf{f}(\alpha_M) \end{bmatrix}, \tag{5.2}$$

where $\mathbf{f}(.)$ is a fixed vector function defined by the structure of the sampling system, and $\mathbf{a}_i, i = 1, 2, \ldots, M$ are the rows of the sensing matrix. The parameters $\alpha_i, i = 1, 2, \ldots, M$ are sampling variables, which could be selected deterministically or randomly according to a given distribution representing the degrees of freedom of the sensing system. As such, the sampling variable α is the only degree of freedom for setting the rows of the sensing matrix.

As shown for the specific problem of interferometry in the previous chapter, the sampling variables can be drawn randomly from an appropriate distribution such that the sensing matrix $\mathbf{A}$ would satisfy the isotropic property [44], i.e. $\mathbb{E}[\mathbf{a}_i^H \mathbf{a}_i] = \mathbf{I}$, where $\mathbf{a}_i^H$ is the Hermitian (conjugate transpose) of the i^{th} row of the sensing matrix, and $\mathbf{I}$ an $N \times N$ identity matrix.

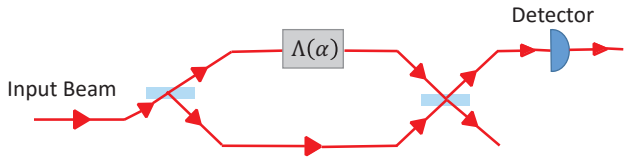

Figure 5.1: Two-arm interferometer used for modal analysis.

In contrast to the standard assumption about the noise being white (often Gaussian) with known variance, herein we further consider a setting where the sampling noise $\mathbf{n}$ has unknown statistics. As such, the common de-noising reconstruction algorithms may not be suitable to recover the sparse or compressible signal even if $\mathbf{A}$ is isotropic.

Instead, we model (5.1) as a compressible vector recovery problem,

$$\mathbf{y} = \mathbf{A}(\mathbf{x} + \mathbf{n}') \triangleq \mathbf{A}\boldsymbol{\beta}, \tag{5.3}$$

where $\mathbf{n} = \mathbf{A}\mathbf{n}'$ and $\boldsymbol{\beta}$ is a compressible vector for a sufficiently high signal to noise ratio (SNR). In the next section, we develop two algorithms to choose the sampling variables α_i in a controlled manner to guarantee accurate reconstruction. Then, we devise a sequential algorithm for data acquisition thereby reducing the required number of measurements.

Controlled sampling

Figure 5.2 shows a randomized approach in which the sampling variables are chosen at random from a given distribution. While the intended vector $\beta = \mathbf{x} + \mathbf{n}'$ is compressible, stable recovery is not guaranteed even if the distribution satisfies the isotropic property due to the lack of knowledge about the noise model. Therefore, we develop control policies

for choosing the degrees of freedom $\alpha_i, i = 1, 2, \ldots, M$ corresponding to M measurements, aiming at improving the quality of the sensing matrix $\mathbf{A}$ wherefore stable reconstruction can be achieved if the SNR is sufficiently high, i.e., when $\boldsymbol{\beta}$ is compressible.

Fig. 5.3 illustrates our proposed controlled approach for choosing the sampling variables. We propose two control policies in which the sampling variables are selected successively such that some measure of information gain is maximized in every step. In Algorithm 1, the newly selected value of α minimizes the projection of the corresponding row $\mathbf{f}(\alpha)$ on the row space of the previously formed rows of $\mathbf{A}$. In Algorithm 2, the sampling variables are selected so as to successively maximize the minimum singular value of the matrix formed from the previous rows and the newly added row. The process is continued until M measurements are collected. A terminal reconstruction algorithm recovers the sparse vector $\mathbf{x}$ from the noisy measurements. The two algorithms are detailed in the tables of Algorithm 1 and 2. The degree of freedom α is generally selected from some dictionary, which could be continuous or discrete. The $\ell \times N$ matrix $\mathbf{A}^\ell$ is the matrix formed from the first ℓ rows.

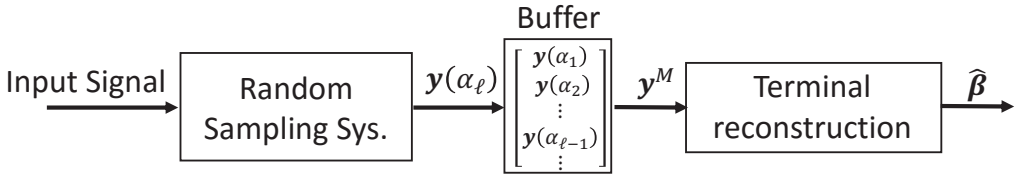

Figure 5.2: Collecting measurements at random.

As shown in Algorithm 1, the ℓ^{th} value α_ℓ is selected as

$$\alpha_\ell = \arg\min_{\alpha \in \mathcal{A}} \text{proj}_{\mathcal{R}(\mathbf{A}^{\ell-1})} \mathbf{f}(\alpha)$$

to minimize the projection onto the row space of $\mathbf{A}^{\ell-1}$. In Algorithm 2, α_ℓ is selected to

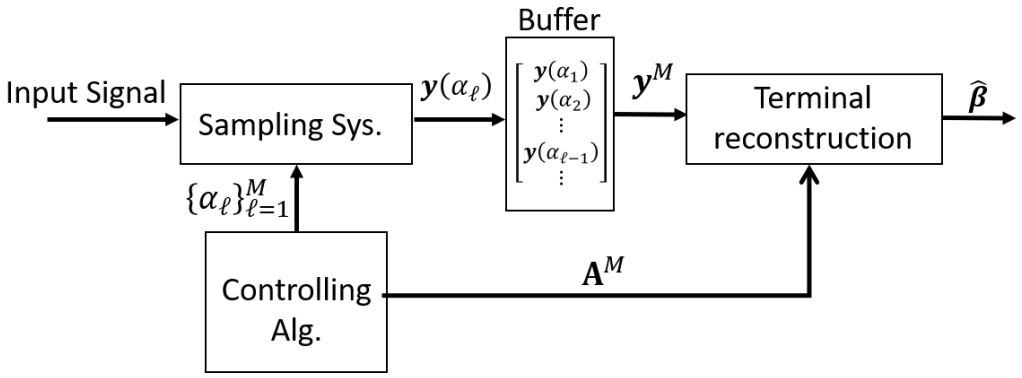

Figure 5.3: Controlled approach for collecting measurements.

Algorithm 1 Minimizing row space projection

Input:

vector function $\mathbf{f}(.)$, dictionary $\mathcal{A}$ of sampling variables

Initialization:

$\ell = 2$, $\mathbf{A}^{\ell-1} = \mathbf{a}_1 = \mathbf{f}(\alpha_1), \alpha_1 \in \mathcal{A}$

While $\ell \leq M$

$\alpha_\ell = \arg\min_{\alpha \in \mathcal{A}} \text{proj}_{\mathcal{R}(\mathbf{A}^{\ell-1})} \mathbf{f}(\alpha)$, where $\text{proj}_{\mathcal{R}(\mathbf{A}^{\ell-1})}$ denotes the projection onto the row space of $\mathbf{A}^{\ell-1}$

$\mathbf{A}^\ell = \begin{bmatrix} \mathbf{A}^{\ell-1} \\ \mathbf{f}(\alpha_\ell)) \end{bmatrix}$

$\ell = \ell + 1$

end While

Output:

$\{\alpha_\ell\}_{\ell=1}^M$, $\mathbf{A} := \mathbf{A}^M$.

maximize the minimum singular value of $\mathbf{A}^\ell$, i.e.,

$$\alpha_\ell = \arg\max_{\alpha \in \mathcal{A}} \lambda_{\min} \left(\begin{bmatrix} \mathbf{A}^{\ell-1} \\ \mathbf{f}(\alpha) \end{bmatrix} \right), \tag{5.4}$$

where $\lambda_{\min}(\mathbf{G})$ is the minimum singular value of a matrix $\mathbf{G}$.

While the proposed controlled sampling approach helps collect informative measurements under sensing constraints, determining the required number of measurements for successful

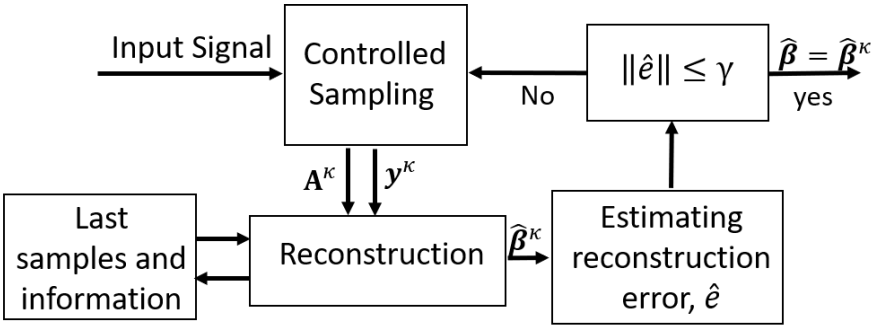

Figure 5.4: Sequential approach to collect the minimum number of measurements.

recovery could be quite challenging. If the number of measurements M is decided prior to data acquisition, M will have to be chosen based on worst case analysis to ensure a target performance in reconstruction, which could in turn lead to an excessive number of measurements. Reducing the sample complexity can be quite beneficial especially in delay-intolerant applications or settings in which data collection is costly. To this end, we propose a sequential approach for data acquisition, in which the controller stops collecting measurements as soon as there is enough confidence that the collected measurements would yield the desired performance. The sequential test consists of a control policy (according to Algorithm 1 or

Algorithm 2 Maximizing singular values

Input:

vector function $\mathbf{f}(.)$, dictionary $\mathcal{A}$ of sampling variables

Initialization:

$\ell = 2$, $\mathbf{A}^{\ell-1} = \mathbf{a}_1 = \mathbf{f}(\alpha_1), \alpha_1 \in \mathcal{A}$

While $\ell \leq M$

$\alpha_\ell = \arg\max_{\alpha \in \mathcal{A}} \lambda_{\min} \left(\begin{bmatrix} \mathbf{A}^{\ell-1} \\ \mathbf{f}(\alpha) \end{bmatrix} \right)$

$\mathbf{A}^{\ell} = \begin{bmatrix} \mathbf{A}^{\ell-1} \\ \mathbf{f}(\alpha_\ell)) \end{bmatrix}$

$\ell = \ell + 1$

end While

Output:

$\{\alpha_\ell\}_{\ell=1}^{M}$, $\mathbf{A} := \mathbf{A}^{M}$.

2), a stopping rule and a terminal approach for reconstruction.

Sequential Approach

We develop a sequential approach thereby reducing the number of measurements acquired to reconstruct the unknown sparse vector given a target reconstruction performance. At each time step κ, the controller verifies if the collected measurements are sufficient to meet the desired performance based on a stopping rule described in this section. If deemed insufficient, the controller collects a new measurement. If the stopping criterion is met, a terminal reconstruction algorithm is adopted to recover the sparse vector. Next, we describe the main steps of the proposed sequential approach.

Primary reconstruction: Suppose a new measurement is collected at time κ by adopting one of the control policies described in the previous Section. An estimate $\hat{\boldsymbol{\beta}}^{\kappa}$ of the compressible vector is obtained using the current and the previous measurements. At this stage, we verify if the current estimate is satisfactory according to the criterion defined by the following stopping rule.

Stopping rule: The stopping rule uses an estimate of the reconstruction error by adopting an estimation procedure from [84], and a predefined value for maximum the number of iterations, κ_{max}. To get an estimate of the error, T extra measurements $y_i = \mathbf{a}_i\boldsymbol{\beta}, i = 1, 2, \ldots, T$ are collected at random. These measurements could be collected once and used for the rest of the procedure. We estimate the second moment of $Z = Y - \hat{Y}$, where $\hat{y}_i = \mathbf{a}_i\hat{\boldsymbol{\beta}}^{\kappa-1}, i = 1, 2, ..., T$, are based on the estimate $\hat{\boldsymbol{\beta}}^{\kappa-1}$, and viewed as realizations of the random variable $\hat{Y}$. The estimate of the second moment is used as a stopping criterion, i.e., we stop either when $\mathbb{E}[Z^2] < \gamma$, for a predefined threshold γ, or $\kappa = \kappa_{max}$. The

following lemma establishes that the second moment of Z provides an upper bound on the reconstruction error. Note that the randomness in Z depends on the distribution of the degree of freedom α of the sensing system.

Lemma 3. *If the sampling variable α is generated from a distribution satisfying $\mathbb{E}[\mathbf{a}(\alpha)^T\mathbf{a}(\alpha)] = \mathbf{I}$, with $\mathbb{E}[\mathbf{a}(\alpha)] = 0$, then $\mathbb{E}[Z^2(\alpha)] = \mathbb{E}[(Y - \hat{Y})^2]$ provides an upper bound on the reconstruction error of the sparse vector $\mathbf{x}$, i.e.,*

$$\|\mathbf{x} - \hat{\mathbf{x}}\|^2 \leq \mathbb{E}[Z(\alpha)^2]. \tag{5.5}$$

Proof. The proof follows directly from the assumption of the lemma. We calculate the second moment of $Z(\alpha)$ as,

$$\begin{aligned}\mathbb{E}[Z(\alpha)^2] &= \mathbb{E}[(Y(\alpha) - \hat{Y}(\alpha))^2] \\ &= \mathbb{E}[(\mathbf{a}(\alpha)(\mathbf{x} - \hat{\mathbf{x}}) + (n - \hat{n}))^2] \\ &= (\mathbf{x} - \hat{\mathbf{x}})\mathbb{E}[\mathbf{a}(\alpha)^T\mathbf{a}(\alpha)](\mathbf{x} - \hat{\mathbf{x}})^T + \mathbb{E}[n^2] + |\hat{n}|^2.\end{aligned} \tag{5.6}$$

Since $\mathbb{E}[\mathbf{a}(\alpha)^T\mathbf{a}(\alpha)] = \mathbf{I}$, then

$$\mathbb{E}[Z(\alpha)^2] = \|\mathbf{x} - \hat{\mathbf{x}}\|^2 + c, \tag{5.7}$$

where c is an unknown positive constant that depends on the noise. □

At each iteration, we estimate $\mathbb{E}[Z(\alpha)^2]$ as,

$$\mathbb{E}[Z(\alpha)^2] \cong \frac{1}{T}\sum_{i=1}^{T} z^2(\alpha_i). \tag{5.8}$$

If the number of measurements used for estimation, T, is sufficient, the estimated metric in

(5.8) provides a reliable upper bound for the error.

Terminal Reconstruction Algorithm

If the upper bound in (5.8) is less than a predefined threshold γ at time κ, or $\kappa = \kappa_{max}$, we stop collecting new measurements and reconstruct the compressible vector as $\hat{\boldsymbol{\beta}} = \hat{\boldsymbol{\beta}}^{\kappa-1}$, where $\hat{\boldsymbol{\beta}}^{\kappa-1}$ is the reconstructed compressible vector using $\kappa - 1$ measurements. Hence, we stop collecting extra measurements as soon as the stopping rule is satisfied thereby reducing the sample complexity.

Controlled sampling in generalized interferometry

Based on the proposed interferometry framework introduced in Chapters 3 and 4, a signal recovery problem from interferometric measurements amounts to a basis analysis problem in which the information of interest is embedded in the expansion coefficients of the interferometer signals in an appropriate space. It was shown in (3.11) that the acquired interferometric measurements are linearly related to these space coefficients through the $M \times 2N$ matrix $\mathbf{A} = [\mathbf{A}_1 \;\; \mathbf{A}_2]$, where $\mathbf{A}_1 = [\cos(\omega_n \alpha_m)]$, and $\mathbf{A}_2 = [-\sin(\omega_n \alpha_m)]$, with $m = 1, 2, \ldots, M$ and $n = 1, 2, \ldots, N$. Comparing this matrix to the general model in (5.2), the vector function $\mathbf{f}(\alpha)$ in the specific problem of interferometry takes the form of,

$$\mathbf{f}(\alpha) = [\cos(\omega_1\alpha) \quad \cos(\omega_2\alpha) \quad \ldots \quad \cos(\omega_N\alpha) \quad \sin(\omega_1\alpha) \quad \sin(\omega_2\alpha) \quad \ldots \quad \sin(\omega_N\alpha)]. \tag{5.9}$$

Hence, instead of a random selection, the generalized delay parameter α can be chosen via the proposed controlled sampling strategies discussed in this chapter, where the noise statistical model is unknown. It is shown through the numerical and experimental results presented in the next section that the quality of information recovery improves by collecting more informative measurements in the proposed controlled manner. As an example, we consider the problem of optical modal analysis in which each row of the sensing matrix would be,

$$\mathbf{f}(\alpha) = [\cos(\omega_1\alpha) \quad \cos(\omega_2\alpha) \quad \dots \quad \cos(\omega_N\alpha)]. \tag{5.10}$$

Numerical and experimental Results

To demonstrate the performance of the proposed algorithms, we provide numerical and experimental results for the problem of optical modal analysis as a specif application following the unifying model for the generalized interferometry problems described in Chapter 3. The goal is to reconstruct the modal content of a light beam from compressive interferometric measurements collected under the physical hardware constraints of the two-path interferometer. The light beam has the form $E(t) = \sum_{i=1}^{N} c_i\psi_i(t)$, where t represents time (e.g. for spectral harmonics) or position (e.g. for spatial modes), $\psi_i(x)$ an orthonormal modal basis, $c_i, i = 1, 2, ..., N$ the modal coefficients, and N the number of possible modes. The beam is assumed to be s-sparse in this modal basis, i.e., at most s coefficients are non-zero.

We consider the measurement model as $\mathbf{y} = \mathbf{A}\mathbf{x} + \mathbf{n}$, where $\mathbf{x}$ is an $N \times 1$ vector with entries $x_i = |c_i^2|, i = 1, \dots, N$, $\mathbf{y}$ a vector of interferometric measurements, and the rows of the sensing matrix $\mathbf{A}$ given by (5.10). In this experiment, we simulate the sampling noise using

white Gaussian noise $\mathbf{n} \sim \mathcal{N}(0, \sigma^2\mathbf{I})$, where σ^2 is an *unknown* noise variance. The SNR of the samples is then defined as SNR $\triangleq 10\log(\frac{\mathbf{x}^{\mathrm{H}}\mathbb{E}[\mathbf{A}^{\mathrm{H}}\mathbf{A}]\mathbf{x}}{\sigma^2})$.

For this simulation, the maximum possible number of modes is $N = 64$. We also assume that the input light beam has unit energy and at most $s = 4$ active modes.With random sampling, we select the α values uniformly between 0 to 2π. In this case, the sensing matrix $\mathbf{A}$ satisfies the isotropy property. We use the Basis Pursuit algorithm for reconstruction, albeit different algorithms could also be used.

As discussed in this chapter, sampling in a controlled manner using the proposed policies maximizes the incoherence between the rows of the sensing matrix, which holds promise to achieve additional reduction in the number of measurements for a target performance. In Fig. 5.5, we show the reconstruction error in a modal analysis problem using HG modes from an actual laboratory experiment. The input light field consists of non-vanishing projections on 4 modes and SNR= 20dB. The results show that the controlled approach has a smaller sample complexity compared to the random approach.

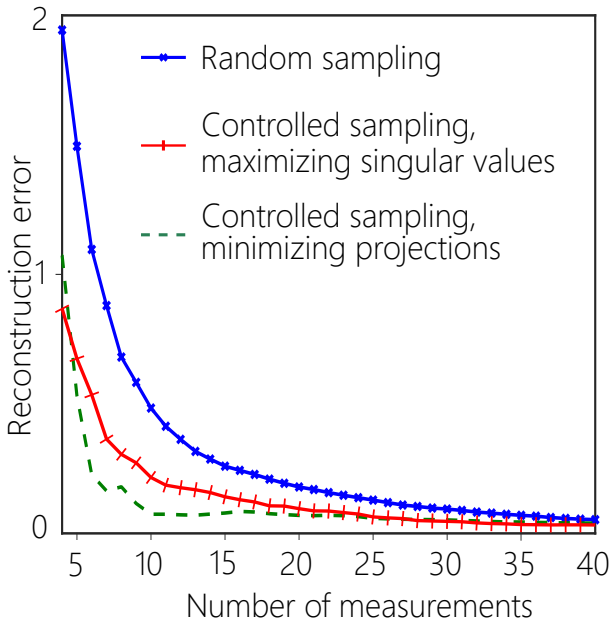

Figure 5.5: Reconstruction error versus M for random and controlled sampling approaches.

Next, we investigate the gains of the sequential approach. T extra measurements are collected uniformly at random to estimate the error bound used for stopping. To assess the performance of the proposed sequential approach with control, we conduct 1000 runs of modal analysis. In each run, measurements are collected sequentially until either the target reconstruction error requirement $e_\beta = 0.04$ is met, or the maximum number of iterations $\kappa_{max} = 40$ is reached. The latter is obtained based on the number of measurements in the worst case required to achieve the target reconstruction error. For this purpose, we use $T = 8$ and $T = 30$ measurements to estimate the error bound with $\gamma = 0.01$, and $\gamma = 0.02$, respectively. Figure 5.6 shows histograms of the number of collected measurements, i.e., a distribution of the stopping time, with the controlled and randomized approaches for a fixed reconstruction error of 0.04. The controlled approach exhibits a better distribution of stopping times, i.e., the reconstruction error requirement is met with less measurements. It can

also be seen that the performance of the sequential approach does not change significantly with $T = 8$ and $T = 30$ measurements.

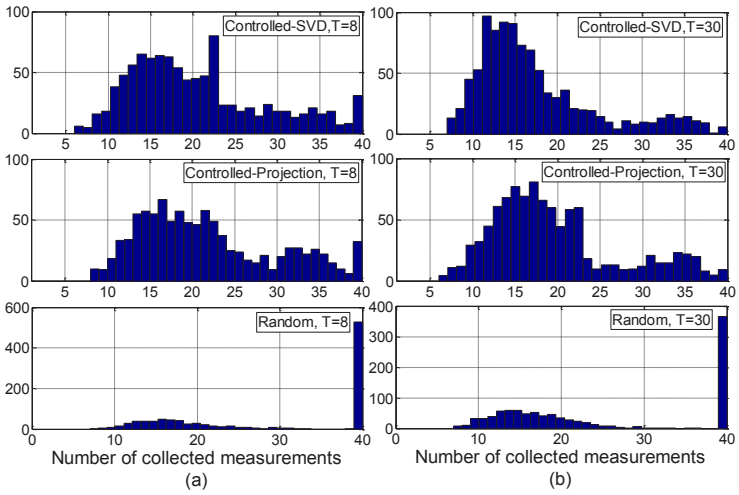

Figure 5.6: The histograms of the required number of measurements for a fixed recovery performance of $e_\beta = 0.04$ and $SNR = 20$ dB, (a) $T = 8$, $\gamma = 0.01$. (b) $T = 30$, $\gamma = 0.02$.

Since the error bound is less tight for smaller values of T, the stopping threshold can be gauged to ensure favorable recovery. As such, the stopping threshold γ is generally set to a value smaller than the target for smaller values of T. Calibration can be used to set better values for the threshold γ. Due to inevitable inaccuracies in the error estimate, occasionally the target performance may not be met. We compare the percentage of times the target performance is unrealized in sequential and batch approaches. We use the singular value based control policy, and set $T = 8$ and $\gamma = 0.01$. The average required number of measurements in 1000 runs are 26, 20, 17, 16 and 15 for SNRs 17 dB, 20 dB, 24 dB, 27 dB and 30 dB, respectively. We perform the simulation in batch using the same average values plus $T = 8$ more measurements used for estimating the error, and calculate the percentage of time the target recovery performance is violated. Figure 5.7 shows the percentage of violation for both the sequential and batch approaches. With the same average number of

measurements, the sequential approach provides a significant improvement over the batch approach.

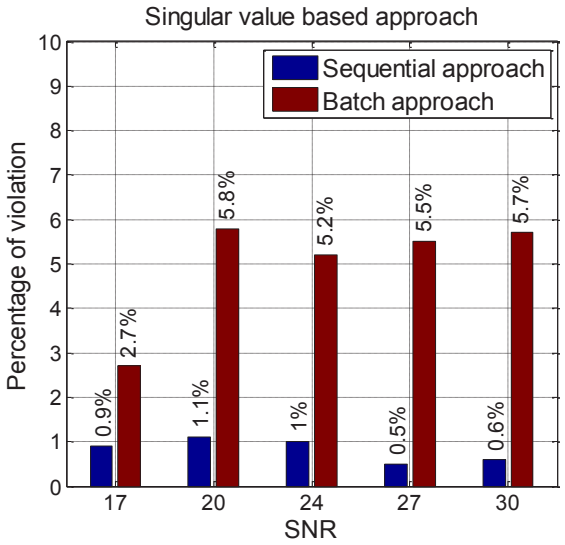

Figure 5.7: Comparing the percentage of time the target performance is violated for both the sequential and batch approaches at different SNRs with singular value based control policy. Here, $T = 8$, $\gamma = 0.01$

Figure 5.8 demonstrates the savings in the required number of measurements by using the sequential approach for a target reconstruction error of $e_\beta = 0.04$ and a tolerable violation of 1% based on 1000 runs. In the batch approach, the number of measurements has to be set based on a worst case, i.e., the maximum number of measurements for which the target reconstruction error and a percentage of time that this error is violated are satisfied. Adopting the sequential approach is shown to yield savings in sample complexity. This simulation also accounts for the extra T measurements required for error estimation (here $T = 8$).

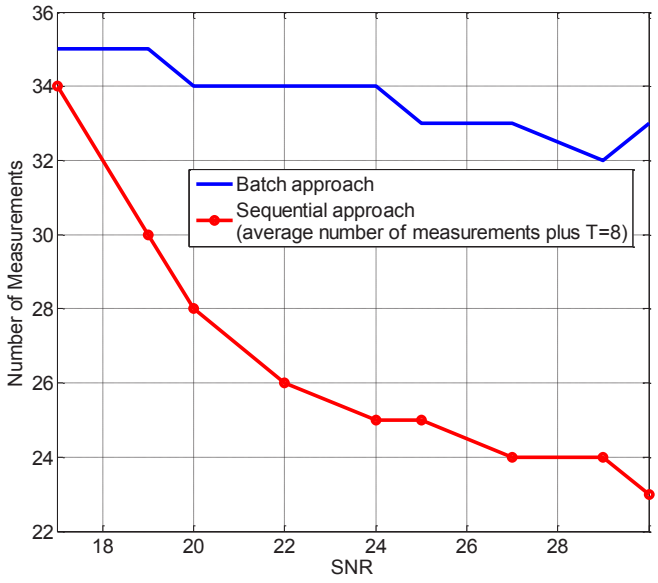

Figure 5.8: Comparing the average number of measurements for error estimation and reconstruction for the sequential and batch approaches based on 1000 runs. The target reconstruction error and the allowable violation probability are 0.04 and 0.01, respectively. In the sequential approach, the threshold of the stopping rule is $\gamma = 0.01$ and the number of measurements collected for estimating the error is $T = 8$.

CHAPTER 6: COMPRESSIVE RECOVERY WITH STRUCTURED NOISE

Introduction

In the previous chapters, we showed how the sensing constraints imposed by the limited number of degrees of freedom of a practical sampling system affect the perfromance of signal reconstruction. In this chapter[1], we focus our attention on another limitation due to imperfect hardware components used to implement the sampling system. Referring to the optical modal analysis example, the limited aperture sizes of SLMs and lenses can be shown to introduce nonlinear terms in the measurement model, whose effects will be comprehensively studied in the next chapter. Other examples include reconstruction of MR images from k-space measurements collected through imperfect hardware [85], and signal recovery from quantized measurements acquired through Analog to Digital Converters (ADCs) [86].

Motivated by these examples, we model the imperfections of sampling systems using structured noise. In contrast to related work on sensing with structured noise, which primarily focused on the sparsity property of such noise [87], we consider a known nonlinear function of the sparse vector with a bounded ℓ_2-norm as our additive structured noise. Quantized measurements acquired through an ADC, and interferograms produced by interferometers with limited-aperture SLMs and lenses are examples of measurements that fit this model.

Approximating the measurement model in presence of the physical constraints through a known nonlinear function of the sparse vector, we propose two novel iterative reconstruction

[1] In this chapter, we use the material presented in Annual Conference on Information Sciences and Systems (CISS), 2017 [13].

algorithms, namely, Orthogonal Matching Pursuit with Structured Noise (OMPSN), and Subspace Pursuit with Structured Noise (SPSN) to remedy the effect of such constraints. The proposed algorithms adopt the main ideas underlying SP and OMP in that the support of the sparse vector is detected then an estimate of the sparse vector is updated at each iteration, albeit they iteratively estimate and remove the non-linear term from the measurements, which makes them more suitable in non-ideal sampling settings. Our numerical results demonstrate that the proposed algorithms outperform the standard OMP and SP algorithms in detecting the support, as well as estimating the sparse vector from inaccurate measurements collected under practical sensing constraints. Hence, our approach to tackle the non-linearity is to estimate and remove its effect on the measurements given side information about the underlying sensing system. Alternatively, one could also resort to non-linear recovery algorithms specifically designed for CS with non-linear models such as the Iterative Hard Thresholding (IHT) based algorithm proposed in [88]. However, such algorithms incur higher computational complexity as shown in the results section. In particular, we show that the proposed algorithms attain better performance in reconstruction than IHT based algorithms in fewer iterations.

Problem Statement

In CS we intend to recover an $N \times 1$ s-sparse vector $\mathbf{x}$ with at most s non-zero elements supported on set T from $M \ll N$ linear compressive measurements

$$\mathbf{y} = \mathbf{A}\mathbf{x}, \tag{6.1}$$

where $\mathbf{A}$ is an $M \times N$ sensing matrix. Adopting appropriate reconstruction algorithms, recovery is guaranteed if $\mathbf{A}$ satisfies some sufficient conditions such as the Restricted Isom-

etry Property (RIP) [30, 89]. However, under practical sensing constraints (e.g. hardware imperfections) the linear model in (6.1) is usually invalid. In such cases, the compressive measurements are better represented as,

$$\mathbf{y} = \mathbf{h}(\mathbf{x}), \tag{6.2}$$

where $\mathbf{h}(.)$ is any (non-linear) vector function from $\mathbb{R}^N$ to $\mathbb{R}^M$. In many applications such as with quantized measurements [86], the model in (6.2) can be reduced to

$$\mathbf{y} \approx \mathbf{A}\mathbf{x} + \mathbf{f}(\mathbf{x}), \tag{6.3}$$

with acceptable accuracy for a known (generally nonlinear) function $\mathbf{f}(.)$ from $\mathbb{R}^N$ to $\mathbb{R}^M$ with bounded ℓ_2-norm, i.e., $\frac{\|\mathbf{f}(\mathbf{x})\|_2}{\|\mathbf{x}\|_2} \leq \epsilon,\ \forall\ \mathbf{x} \in \Sigma_s$. Here, Σ_s is the set of all s-sparse vectors in $\mathbb{R}^N$. Given that $\mathbf{f}(.)$ is known, the nonlinear part amounts to structured noise $\mathbf{n} \triangleq \mathbf{f}(x)$.

Example: To clarify this source of error, consider the optical modal analysis example in which we seek to analyze a light beam $\psi(t)$ in a Hilbert space spanned by an orthonormal basis $\{\phi_i(t)\}_{i=1}^N\}$ (e.g. corresponding to spatial modes) as $\psi(t) = \sum_{i=1}^N c_i \phi_i(t)$, where $c_i,\ i = 1, 2, ..., N$ are positive and real modal coefficients with $\sum_{i=1}^N |c_i|^2 = 1$. Applying different phase shifts $\alpha_m \in \mathcal{A}$ and superposing the output beams of the interferometer produces intensity measurements

$$I(\alpha_m) = 1 + \sum_{i=1}^{N} |c_i|^2 a_i(\alpha_m),\ \alpha_m \in \mathcal{A}, \tag{6.4}$$

where $|\mathcal{A}| = M \ll N$, and $a_i(.),\ i = 1, 2, ..., N$ are functions defined by the setup [54, 37]. Commonly, most of the energy of the beam is contained in few modes, hence the vector $\mathbf{x}$ with entries $|c_i|^2,\ i = 1, 2, ..., N$ is naturally sparse. As a result, the interferometric measurements

admit a linear model

$$\mathbf{y} \triangleq \mathbf{I} - \mathbf{1} = \mathbf{A}\mathbf{x}, \tag{6.5}$$

and CS reconstruction algorithms can be applied to reveal the modal content, $\mathbf{x}$ [9, 90]. Here, $\mathbf{1}$ is an $M \times 1$ vector of all ones, and $\mathbf{I} \triangleq [z(\alpha_1)z(\alpha_2)...z(\alpha_M)]^T$. In this system, the $M \times N$ sensing matrix $\mathbf{A} \triangleq [a_i(\alpha_m)]_{m,i},\ m = 1, 2, ..., M, i = 1, 2, ..., N$.

The linear model in (6.5) is ideal in that it does not account for practical hardware limitations. For example, we can show that clipping effects from the limited aperture sizes of the lenses and SLMs give rise to measurements of the form

$$\mathbf{y} = \bar{\mathbf{A}}\mathbf{x} + \underbrace{\mathbf{B}\mathbf{g}(\mathbf{x})}_{\mathbf{f}(\mathbf{x})}, \tag{6.6}$$

where $\bar{\mathbf{A}}$ is a modified sensing matrix, $\mathbf{B}$ an $M \times N(N-1)$ matrix, and $\mathbf{g}(\mathbf{x})$ an $N(N-1) \times 1$ vector with entries $\sqrt{x_i x_j}$, for $i \neq j,\ i = 1, 2, ..., N,\ j = 1, 2, ..., N$ [75]. Given the known interferometer structure, the function $\mathbf{f}(\mathbf{x})$ can be approximated and treated as structured noise.

Iterative denoising algorithms

In recovering a sparse vector from incomplete or noisy measurements, the iterative reconstruction algorithms leverage some side information about the noise, such as an upper bound on its ℓ_2-norm, to establish new stopping rules, but not to improve the recovery procedure. For example, instead of stopping after s iterations, [91] devises a new stopping rule for the OMP algorithm by incorporating side information about the upper bound of the noise energy. In sharp contrast, in the following we propose two iterative denoising algorithms – as

variants for the OMP and SP algorithms – that leverage side information about the sampling system structure, thus the known function $\mathbf{f}(.)$, for sparse recovery.

OMP with Structured Noise (OMPSN)

The proposed greedy algorithm, termed OMP with Structured Noise (OMPSN), seeks to find a sparse solution from linear and incomplete measurements $\mathbf{y}$ of the form (6.3) by leveraging side information about the sampling system. Similar to OMP, we adopt a maximum correlation criterion to iteratively detect the support of the sparse vector. An approximated support set Λ is updated at each iteration, then the sparse vector $\mathbf{x}'$ supported on Λ is estimated via the ℓ_2-norm minimization,

$$\mathbf{x}' = \underset{\mathbf{x}:\text{supp}(\mathbf{x})\subseteq\Lambda}{\arg\min} \|\mathbf{y} - \mathbf{A}\mathbf{x}\|_2. \tag{6.7}$$

Approximating the structured noise as $\mathbf{n}' = \mathbf{f}(\mathbf{x}')$, we update the measurements by subtracting the estimated noise from the collected measurements as,

$$\mathbf{y}_u = \mathbf{y} - \mathbf{n}'. \tag{6.8}$$

Subsequently, the residual vector $\mathbf{y}_r$ is calculated for the next iteration using $\mathbf{y}_u$ as the measurement vector and Λ as an approximation of the actual support T (see Algorithm 3). The same procedure is repeated for s iterations to estimate the support of $\mathbf{x}$. At each iteration the measurements are refined so that the model approaches the linear model $\mathbf{y} = \mathbf{A}\mathbf{x}$. In Algorithm 3, $\mathbf{A}_\Lambda^\dagger \triangleq (\mathbf{A}_\Lambda^H \mathbf{A}_\Lambda)^{-1}\mathbf{A}_\Lambda^H$, where the matrix $\mathbf{A}_\Lambda$ and vector $\mathbf{x}'_\Lambda$ are the columns of $\mathbf{A}$ and entries of $\mathbf{x}'$ indexed by Λ, respectively.

To visualize the operation of OMPSN, Fig. 6.1 illustrates the progression of the algorithm

in the case where the support is correctly identified over the iterations, i.e. $\Lambda \subseteq T$. If the acquisition system was ideal (i.e., $\mathbf{f}(\mathbf{x}) = 0$), the measurement vector $\mathbf{y}$ would lie in the span of the columns of $\mathbf{A}_T$ and the ℓ_2-norm minimization (6.7) would yield the exact solution. But if $\mathbf{f}(\mathbf{x})$ is non-zero, the performance of sparse recovery is improved by continuously updating the measurement vector $\mathbf{y}$ as in (6.8) to obtain $\mathbf{y}_u$ which lies closer to the column space of $\mathbf{A}_\Lambda$, so that eventually $\mathbf{y}_u \approx \mathbf{A}\mathbf{x}$.

Performance of OMPSN: For brevity, we defer the full analysis of OMPSN to an extended version of this work and provide some insight in the sequel. In the noiseless case, OMP was shown to detect the exact support of an s-sparse vector from compressive measurements in s iterations if $\mathbf{A}$ satisfies the RIP with a sufficiently small parameter [92]. With noisy measurements $\mathbf{y} = \mathbf{A}\mathbf{x} + \mathbf{n}$, where $\|\mathbf{n}\|_2 \leq \epsilon$, OMP can be modified by incorporating side information about the norm of the noise component to stop when $\|\mathbf{y}_r\|_2 \leq \epsilon$, rather than using s iterations.

The analysis leverages Theorem 1 in [91], which established that the modified OMP algorithm with the new stopping rule yields the correct support if $\mathbf{A}$ satisfies the Mutual Incoherence Property (MIP) [93] with $\mu < \frac{1}{2s-1}$, and $|x_i| \geq \frac{2\epsilon}{1-(2s-1)\mu}$, $\forall\, i \in \text{supp}(\mathbf{x})$, where μ is the mutual incoherence defined as $\mu \triangleq \max_{i \neq j} |\mathbf{a}_i^H \mathbf{a}_j|$, $i = 1, 2, ..., N, j = 1, 2, ..., N$, and $\mathbf{a}_i^H$ is the conjugate transpose of the i^{th} column of $\mathbf{A}$. If $\frac{\|\mathbf{f}(\mathbf{x})\|_2}{\|\mathbf{x}\|_2} \leq \epsilon$ for ϵ sufficiently small (equivalently when the Signal to Noise Ratio, SNR $\triangleq 10 \log \frac{\|\mathbf{A}\mathbf{x}\|_2^2}{\|\mathbf{f}(\mathbf{x})\|_2^2}$ is sufficiently large), and the conditions of [91, Theorem 1] hold, OMPSN correctly identifies the first element of the support and estimates the corresponding entry of $\mathbf{x}$. As we correctly identify more elements of the support, we refine our estimates of $\mathbf{x}$, and in turn of the structured noise. Since the measurements are progressively updated, we obtain cleaner measurements, $\mathbf{y}_u = \mathbf{A}\mathbf{x} + \hat{\mathbf{n}}$, with $\frac{\|\hat{\mathbf{n}}\|_2}{\|\mathbf{x}\|_2} \leq \hat{\epsilon}$ for which $\hat{\epsilon} \leq \epsilon$, so the condition $|x_i| \geq \frac{2\hat{\epsilon}}{1-(2s-1)\mu}$ is satisfied even for smaller entries of $\mathbf{x}$. As $\hat{\epsilon} \to 0$ with more iterations, OMPSN can accurately recover $\mathbf{x}$ in s iterations with high probability.

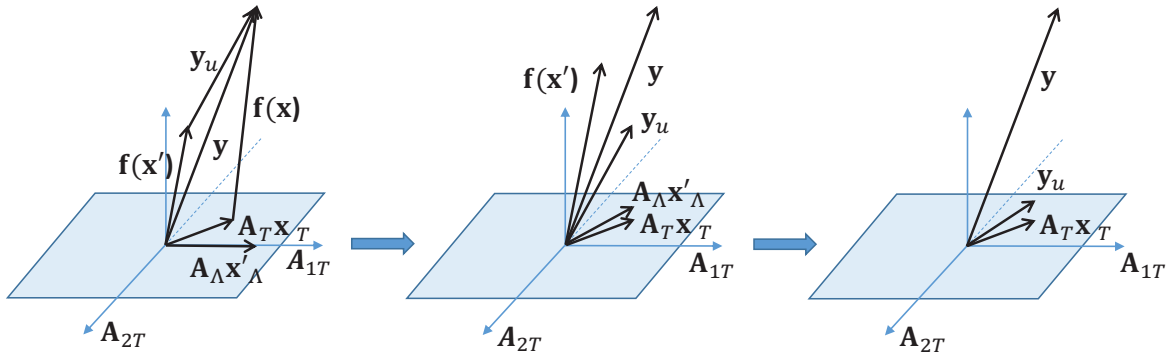

Figure 6.1: Recovering a 2-sparse vector using OMPSN. At each iteration one element of the support is detected and more accurate measurements $\mathbf{y}_u$ are calculated.

Algorithm 3 Orthogonal Matching Pursuit with Structured Noise (OMPSN)

Input:

$\mathbf{A}$, $\mathbf{y}$, s, function $\mathbf{f}(.)$

Initialization:

$\mathbf{y}_u = \mathbf{y}$, $\mathbf{y}_r = \mathbf{y}$, $\Lambda = \emptyset$, $\ell = 0$.

While $\ell < s$

$\Lambda = \Lambda \bigcup \{ \underset{i \in \{1,2,\ldots,N\}}{\text{argmax}} \; |\mathbf{a}_i^H \mathbf{y}_r| \}$

$\mathbf{x}'_\Lambda = \mathbf{A}_\Lambda^\dagger \mathbf{y}_u$, $\mathbf{x}'_{\Lambda^c} = \mathbf{0}$

$\mathbf{n}' = \mathbf{f}(\mathbf{x}')$ // estimating the structured noise

$\mathbf{y}_u = \mathbf{y} - \mathbf{n}'$ // update step

$\mathbf{y}_r = \mathbf{y}_u - \mathbf{A}_\Lambda \mathbf{A}_\Lambda^\dagger \mathbf{y}_u$ // calculating residual

$\ell = \ell + 1$

end While

Output:

$\hat{\mathbf{x}} = \mathbf{x}'$.

SP with Structured Noise (SPSN)

We develop a second algorithm termed (SPSN) as a variant of SP [72] in the presence of structured noise. We briefly describe the main steps and report on performance results in Section 6. Similar to OMPSN, SPSN is also an iterative greedy algorithm that seeks a sparse solution from inaccurate measurements (6.3). The main distinction is that the compressive measurements are used to detect the entire support set, $\hat{T}$, at every iteration. Subsequently, we perform the following steps at each iteration to approximate the structured noise and mitigate the imperfections of non-ideal acquisition systems: (i) Estimate the sparse vector: $\tilde{\mathbf{x}}_{\hat{T}} = \mathbf{A}_{\hat{T}}^{\dagger}\mathbf{y}_u$, $\tilde{\mathbf{x}}_{\hat{T}^c} = \mathbf{0}$; (ii) Approximate the noise given the knowledge of $\mathbf{f}(.)$: $\tilde{\mathbf{n}}{=}f(\tilde{\mathbf{x}})$; (iii) Update the measurements: $\mathbf{y}_u = \mathbf{y} - \tilde{\mathbf{n}}$; (iv) Calculate the residual: $\mathbf{y}_r = \mathbf{y}_u - \mathbf{A}_T\mathbf{A}_T^{\dagger}\mathbf{y}_u$; (v) Start a new iteration with updated measurements $\mathbf{y}_u$.

The analysis of SPSN leverages a result in [72], which established that in the presence of additive noise with bounded ℓ_2-norm, SP reconstructs an s-sparse vector with bounded error if $\mathbf{A}$ satisfies the RIP of order $3s$ with parameter $\delta < 0.083$. This sufficient condition implies a primary condition under which the SPSN recovers the sparse signal from inaccurate measurements with tolerable error.

Simulation and numerical results

To examine the performance of the proposed algorithms, we consider three examples with imperfect sampling structures. In all examples, the reconstruction error is defined as $\frac{\|\mathbf{x}-\hat{\mathbf{x}}\|_2}{\|\mathbf{x}\|_2}$, where $\hat{\mathbf{x}}$ is the estimated sparse vector. The results are obtained by averaging over 1000 independent runs.

Algorithm 4 Subspace pursuit with structured noise

Input:

$\mathbf{A}$, $\mathbf{y}$, s, function $f(.)$

Initialization:

$\mathbf{y}_u = \mathbf{y}$.

$\hat{T}$={Indices of s biggest absolute values of $\mathbf{A}^H\mathbf{y}_u$ }

$\mathbf{y}_r = \mathbf{y}_u - \mathbf{A}_{\hat{T}}\mathbf{A}_{\hat{T}}^{\dagger}\mathbf{y}_u$

While $\mathbf{y}_r \neq 0$

$T' = \hat{T} \bigcup$ {Indices of s biggest absolute values of $\mathbf{A}^H\mathbf{y}_r$}

$\mathbf{x}' = \mathbf{A}_{T'}^{\dagger}\mathbf{y}_u$

$\tilde{T}$={Indices of s biggest absolute values of $\mathbf{x}'$ }

$\tilde{\mathbf{x}}_{\hat{T}} = \mathbf{A}_{\tilde{T}}^{\dagger}\mathbf{y}_u, \quad \tilde{\mathbf{x}}_{\hat{T}^c} = \mathbf{0}$

$\tilde{\mathbf{n}}$=$f(\tilde{\mathbf{x}})$ // estimating the structured noise

$\mathbf{y}_u$=$\mathbf{y} - \tilde{\mathbf{n}}$ // Update step

$\tilde{\mathbf{y}}_r$=$\mathbf{y}_u - \mathbf{A}_{\tilde{T}}\mathbf{A}_{\tilde{T}}^{\dagger}\mathbf{y}_u$ // Calculating residual

If $\|\tilde{\mathbf{y}}_r\|_2 > \|\mathbf{y}_r\|_2$

Terminate iteration.

else

$\mathbf{y}_r = \tilde{\mathbf{y}}_r$

$\hat{T} = \tilde{T}$

end If

end While

Output:

$\hat{\mathbf{x}}$=$\tilde{\mathbf{x}}$.

Polynomial Model

We aim to recover a 5-sparse vector $\mathbf{x} \in \mathbb{R}^{100}$ from $M = 40$ measurements modeled as (6.3), where $\mathbf{f}(\mathbf{x}) = \mathbf{B}\mathbf{g}(\mathbf{x})$. Here, $\mathbf{g}(\mathbf{x})$ is an $N \times 1$ polynomial function with the i^{th} entry,

$$g_i(\mathbf{x}) = x_{m_i}^2 + x_{n_i}^3 + x_{k_i}^4 + x_{l_i}^5, \ m_i \neq n_i \neq k_i \neq l_i. \tag{6.9}$$

Normalizing $\mathbf{g}(\mathbf{x})$, the entries of the $M \times N$ matrix $\mathbf{B}$ are drawn from a Gaussian distribution $\mathcal{N}(0, \sigma^2)$, so SNR $\triangleq 10\log_{10}\frac{\|\mathbf{A}\mathbf{x}\|_2^2/M}{\sigma^2}$. The entries of $\mathbf{A}$ and the non-zero elements of $\mathbf{x}$ are drawn from a Gaussian distribution. The polynomial model (6.9) provides a general example

for dense structured noise – not necessarily sparse corrupting noise.

In Fig. 6.2, we compare the reconstruction error of the proposed algorithms with that of OMP and SP for different SNRs. The proposed algorithms are shown to outperform regular OMP and SP for most SNRs.

To recover the support of $\mathbf{x}$, we can alternatively use the IHT-based algorithm of [88] designed to extract information from non-linear measurements. In this approach, the measurements $\mathbf{y} = \mathbf{A}(\mathbf{x})$, where $\mathbf{A}(.)$ is a general non-linear function, are linearly approximated by an affine Taylor series expansion at point $\hat{\mathbf{x}}$ as $\mathbf{y} \approx \hat{\mathbf{A}}_{\hat{\mathbf{x}}}\mathbf{x}$. Subsequently, this approximation is used in an iterative process to recover the sparse vector $\mathbf{x}$ as,

$$\mathbf{x}^{n+1} = \mathcal{P}_s(\mathbf{x}^n + \mu\hat{\mathbf{A}}^T_{\mathbf{x}^n}(\mathbf{y} - \mathbf{A}(\mathbf{x}^n))), \tag{6.10}$$

where $\mathbf{x}^n$ is the vector recovered at the n^{th} iteration, $\mathcal{P}_s$ the projection operator on the set of s-sparse vectors Σ_s, and μ the step size. Adapting this algorithm to our measurement model, the iterations in (6.10) reduce to

$$\mathbf{x}^{n+1} = \mathcal{P}_s(\mathbf{x}^n + \mu\mathbf{A}^T_{\mathbf{x}^n}(\mathbf{y} - \mathbf{A}\mathbf{x}^n - \mathbf{f}(\mathbf{x}^n))). \tag{6.11}$$

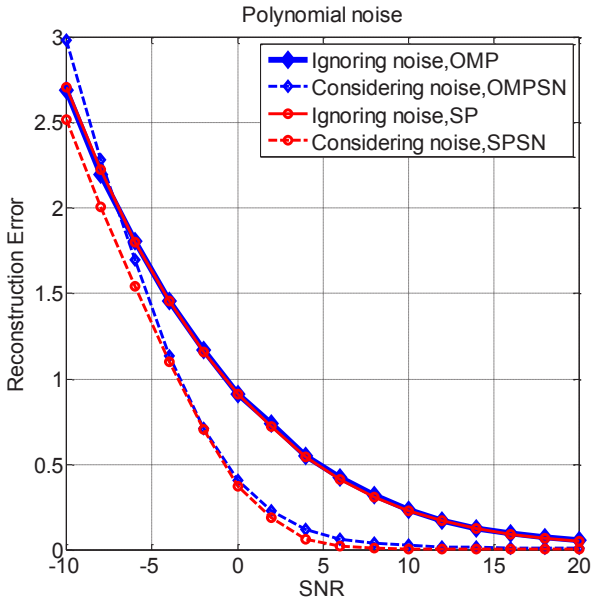

Figure 6.2: Reconstruction error of denoising and regular iterative algorithms versus SNR with the polynomial noise model, $N = 100, M = 40, s = 5$.

In Fig. 6.3, we compare the performance of our proposed approaches and the IHT-based technique with the polynomial model. As shown in Fig. 6.3-(a), OMPSN and SPSN achieve a lower reconstruction error than IHT at decent SNRs. We also note that OMSPN and SPSN have lower computational complexity as they require no more than $s = 5$ iterations versus 30 iterations for IHT to achieve the shown performance with similar complexity per iteration. In Fig. 6.3-(b), we compare the performance of the three algorithms while fixing the number of iterations, i. e., $s = 5$. As shown, the proposed algorithms achieve a substantially smaller reconstruction error than the IHT-based non-linear approach.

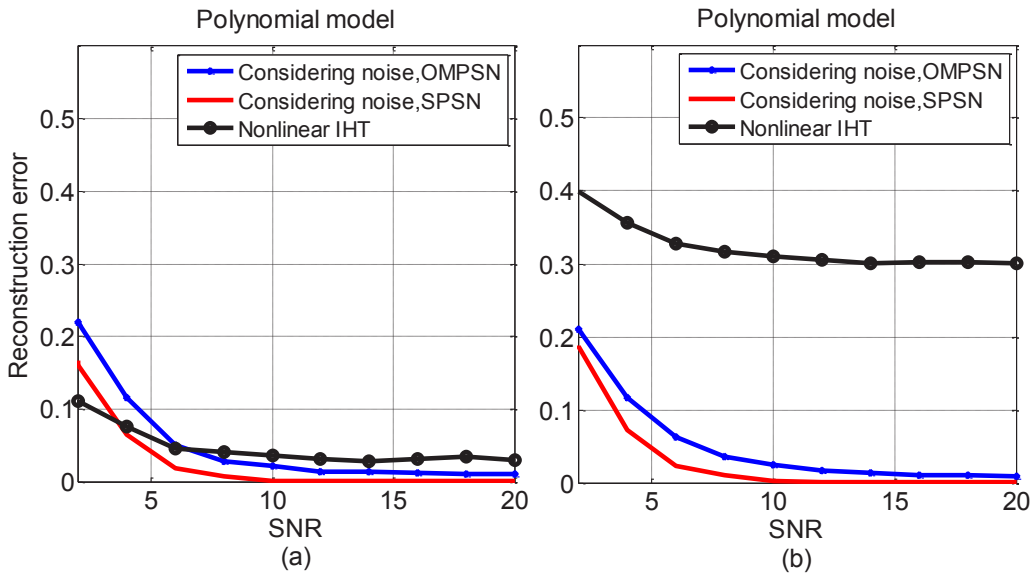

Figure 6.3: Comparing the performance of the proposed OMPSN and SPSN algorithms to the IHT-based approach in [88]. (a) OMPSN and SPSN use $s = 5$ iterations, versus 30 iterations for IHT, (b) performance with a fixed number of iterations (5 iterations).

Optical Interferometry Model

We consider the optical interferometry model (6.6) of Section 6. The sparse vector is generated as before with $N = 100$ and $s = 5$. For simplicity, the entries of $\hat{\mathbf{A}}$ and $\mathbf{B}$ are drawn from a Gaussian distribution. Fig. 6.4 (a) demonstrates that the proposed algorithms are more successful at estimating the sparse vector $\mathbf{x}$ than OMP and SP. Fig.6.4 (b) shows the percentage of support misdetections computed as the ratio of the number of incorrect indices and s. OMPSN, and SPSN are shown to outperform the regular OMP and SP algorithms.

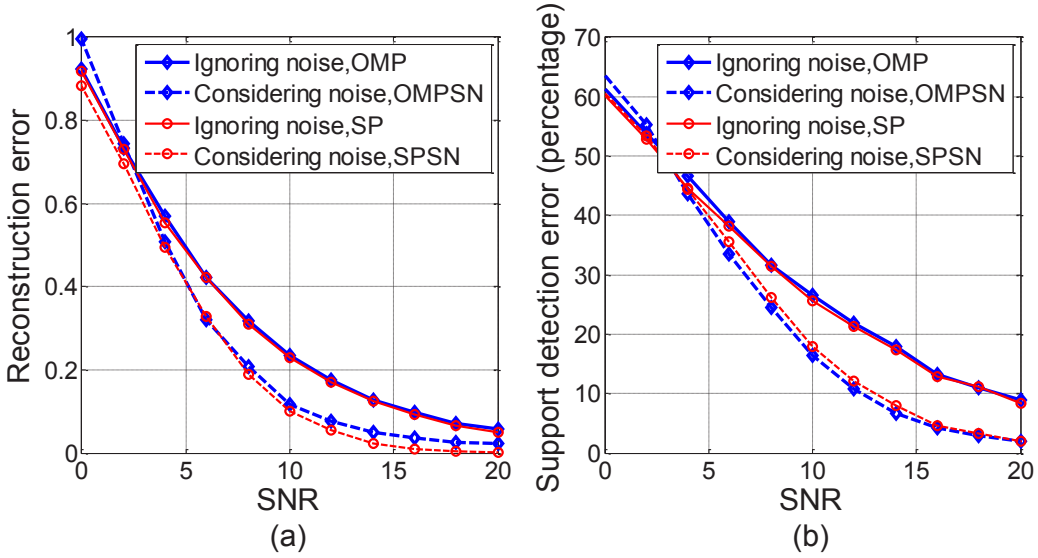

Figure 6.4: Performance of the proposed denoising algorithms and regular OMP and SP, (a) reconstruction error, (b) percentage of misdetections of the support versus SNR for the optical interferometry model (6.6), $N = 100, M = 40, s = 5$.

Image Reconstruction

In this example we seek to reconstruct a sparse image from inaccurate measurements contaminated by structured noise following the same model in (6.6). Here, $\mathbf{x}$ is a 400×1 sparse vector of intensity measurements of a 20×20 pixels image. The number of pixels with nonzero intensity s, and the number of collected measurements M are 29, and 250, respectively. The noise function $\mathbf{g}(x)$ is defined as in the previous example. At SNR= 5dB, OMPSN and SPSN are better at detecting the support than OMP and SP as shown in Fig. 6.5 (a). Also, the proposed algorithms estimate the nonzero elements of $\mathbf{x}$ more accurately at SNR= 10dB as shown in Fig. 6.5 (b).

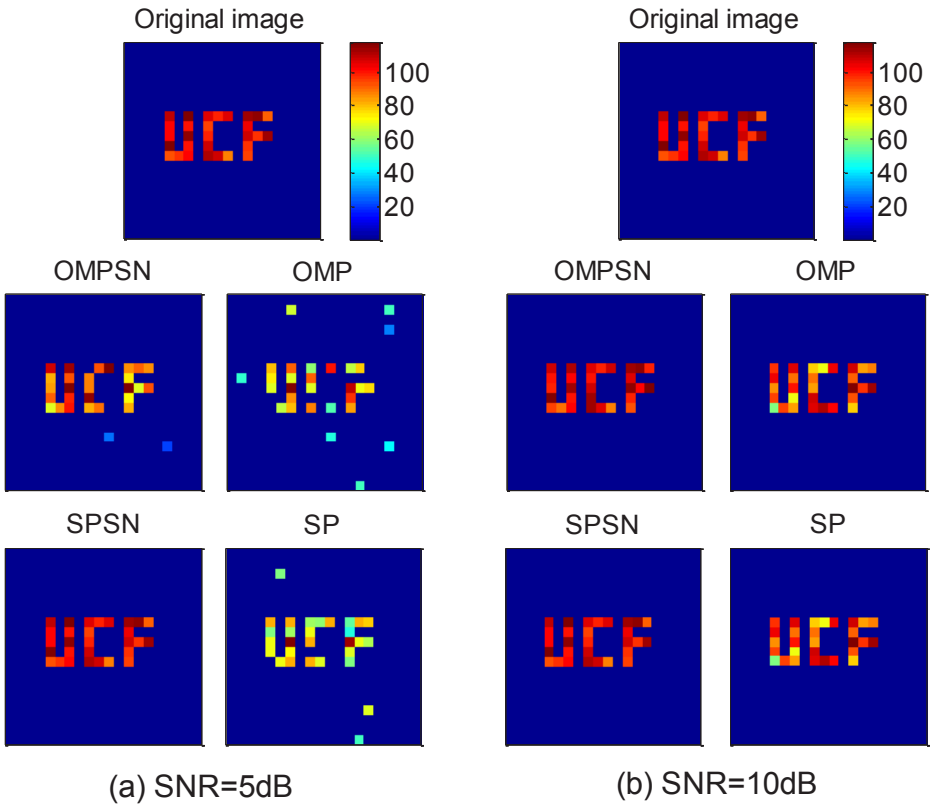

Figure 6.5: Performance of algorithms at SNR=5dB, SNR=10dB, $N = 400, M = 250$, and $s = 29$, with the noise model in (6.6).

CHAPTER 7: OPTICAL MODAL ANALYSIS UNDER CLIPPING EFFECTS

Introduction

In the previous chapter, we studied the effect of imperfect hardware components used to implement the data acquisition systems on the quality of information recovery. As shown and discussed, these effects can be modeled as a structured noise in the measurement model. To overcome the adverse effects of such physical constraints in the signal recovery problems, we introduced two de-noising recovery algorithms in which the measurements are gradually refined over several iterations and the information of interest is simultaneously reconstructed.

Clipping effects due to the finite-aperture size of the hardware components, the limited *spatial phase resolution* along the transverse direction due to the non-vanishing pixel size, and the *phase granularity* due to the finiteness of the number of phase quantization levels of devices such as optical detectors and SLMs are examples of undesired physical effects which can introduce non-linearities in the measurement model. Among such limitations, aperture-finiteness of the hardware components has the most destructive effect in many signal recovery problems such as optical modal analysis.

This chapter[1] takes a principled approach to analyzing the effects that the finite aperture size and the ensuing beam clipping have on the ability to perform optical modal analysis in generalized interferometry. We also leverage the results of the analysis to devise a class of clipping-cognizant reconstruction algorithms to compensate for such effects, shown to yield

[1]In this chapter, we use the material published in Journal of the Optical Society of America A (JOSA A), 2018 [11].

significant gains over schemes oblivious to such effects. To the best of our knowledge, this is the first work to provide a rigorous analysis of the interplay of finite aperture size on signal reconstruction and to provide clipping-cognizant solutions thereof. Next, we summarize the main technical contributions of this work.

• We develop a clipping-cognizant measurement model capturing the finite aperture size using clipping Linear Canonical Transforms (LCTs). Details regarding the response of clipping LCTs are provided in Appendix A.

• We analyze the response of a generalized delay system modeled as a cascade of regular and clipping LCTs. Appendix B provides an analysis of the output field for different combinations of LCTs.

• We develop iterative modal reconstruction schemes leveraging the clipping-cognizant measurement model to compensate for the clipping effects.

It is important to note that our work is different from, and should not be confused with, a large body of work on super-resolution techniques, in which one aims to recover *missing information* about an object or light beam due to various practical restrictions (such as the optical diffraction limit [31] and the non-zero detector pixel size in optical imaging) by leveraging *prior information about the input signal* [32]. For example, in super-resolution techniques used for imaging, the non-redundant information of several images and frames are combined to improve the resolution of one image [33]. In this paper, we do not seek to recover information missing due to finite-aperture size. Rather, we exploit a derived (through rigorous analysis) clipping-cognizant measurement model to ensure that information relevant to the modal content of a light beam (and intrinsic to the interferometric measurements) is not disregarded in the reconstruction phase as in traditional models that overlook finite-

aperture effects.

We also remark that while our focus is on optical modal analysis using interferometry, the analysis and machinery developed herein can be quite useful in other contexts, therefore could inspire further research on reconstruction algorithms that account for important and practical hardware limitations.

Optical modal analysis: Ideal setting

We briefly restate the problem of optical modal analysis based on the generalized interferometry framework and analysis provided in Chapter 2, and Chapter 3, where we showed that a signal or optical field of interest can be analyzed in any arbitrary Hilbert space. More formally, consider an input beam, $\psi(x) = \sum_{n=1}^{N} c_n \phi_n(x)$, in a Hilbert space spanned by a discrete orthonormal basis $\{\phi_n(x)\}$, with arbitrary degree of freedom x (e.g., spatial, angular, temporal), where c_n, $n = 1, 2, \ldots, N$, are the modal coefficients. Replacing the time delay in the reference arm with a generalized operator $h(x, x'; \alpha) := \sum_{n=1}^{N} e^{-in\alpha} \phi_n(x) \phi_n^*(x')$ for which $\{\phi_n(x)\}$ are eigenfunctions, the output beam will be,

$$\psi(x; \alpha) = \sum_{n=1}^{N} c_n \, e^{-in\alpha} \phi_n(x), \tag{7.1}$$

where α is a generalized delay parameter, and $e^{-in\alpha}$ the eigenvalue corresponding to $\phi_n(x)$. Combining the output of the reference arm and the input beam, we record an interferogram $I(\alpha)$.

Based on the general model established in (3.12), the interferometric measurements take the form of,

$$\mathbf{y} = \mathbf{A}\mathbf{x}, \tag{7.2}$$

where $\mathbf{y} = [y(\alpha_1)\, y(\alpha_2)\, \ldots\, y(\alpha_M)]^{\mathrm{T}}$ is an $M \times 1$ measurement vector with entries, $y(\alpha_m) := \frac{I(\alpha_m)-2}{2}$, for M chosen settings α_m, $m = 1, 2, ..., M$, of the generalized delay parameter, $\mathbf{x} = [|c_1|^2\, |c_2|^2\, \ldots\, |c_N|^2]^{\mathrm{T}}$ the $N \times 1$ vector of modal weights, and $\mathbf{A}$ an $M \times N$ matrix with entries $\cos(n\alpha_m)$, $n = 1, 2, ..., N$, $m = 1, 2..., M$, mapping the coefficient vector $\mathbf{x}$ to an $\mathbb{R}^M$-dimensional measurement space. Our prior work exploited this alternative representation for the interferogram model to achieve compression gains in sample complexity and establish analytical performance guarantees for generalized modal analysis from compressive interferometric measurements sampled at sub-Nyquist rates [9, 8].

Finite-aperture effect

The previous section focused on optical modal analysis using generalized interferometry in an idealistic setting. In practice, however, the quality of the measurements collected will inevitably depend on the limitations of the hardware used and the underlying physical system constraints – hence, the actual interferogram will deviate from the idealistic model in (7.2), which could adversely affect the performance of modal reconstruction. For example, in [15] we have reported on the degradation in the quality of interferograms recorded experimentally originating from *clipping effects* due to the finite-aperture size of the SLMs, the limited *spatial phase resolution* along the transverse direction due to their non-vanishing pixel size, and the *phase granularity* due to the finiteness of the number of phase quantization levels.

Our experimental investigations have further revealed that the clipping of the beams at the output of the SLMs beyond their aperture size limits has the most consequential effect on the quality of interferograms and, in turn, on modal reconstruction. For illustration, consider the example in Fig. 7.1, which shows the output interferogram of the generalized interferometer in Fig. 3.3 for an input beam consisting of the second Hermite Gaussian mode HG_2, but this

time taking the finite-aperture and non-vanishing pixel size of the SLMs into consideration. In theory, we expect the interferogram to exhibit a peak at $\alpha = 0$. However, in both simulations and experiments, we see an apparent drop at $\alpha = 0$ when the size of the SLMs is 16mm and the pixel size is 10μm (Fig. 7.1(a)). This is because the configuration shown no longer realizes the intended (ideal) frFT for which the HG mode is an eigenfunction. The observed drop is retained even if we use a finer pixel size of 5μm as shown in Fig. 7.1(b). The peak, however, is extant if we increase the SLM size to 60mm as per Fig. 7.1(c).

Motivated by that, this paper seeks to develop a thorough mathematical analysis of the impact of the finite-aperture size on the interferograms, and, leveraging the results of this analysis, propose a new paradigm for reconstruction that alleviates the ensuing degradation in mode recovery.

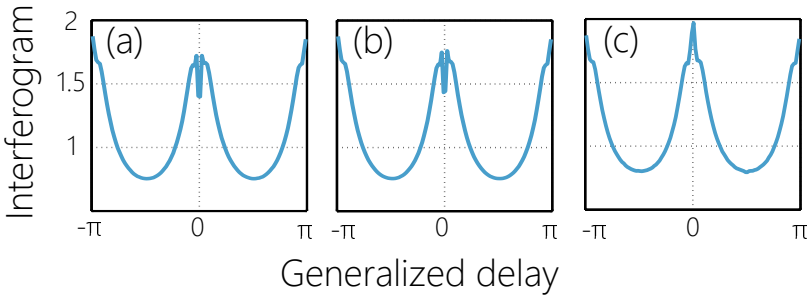

Figure 7.1: The effect of spatial aperture and pixel size on the quality of the interferograms. (a) SLM size of 16mm and pixel size of 10μm. (b) SLM size of 16mm and pixel size of 5μm. (c) SLM size of 60mm and pixel size of 10μm [15].

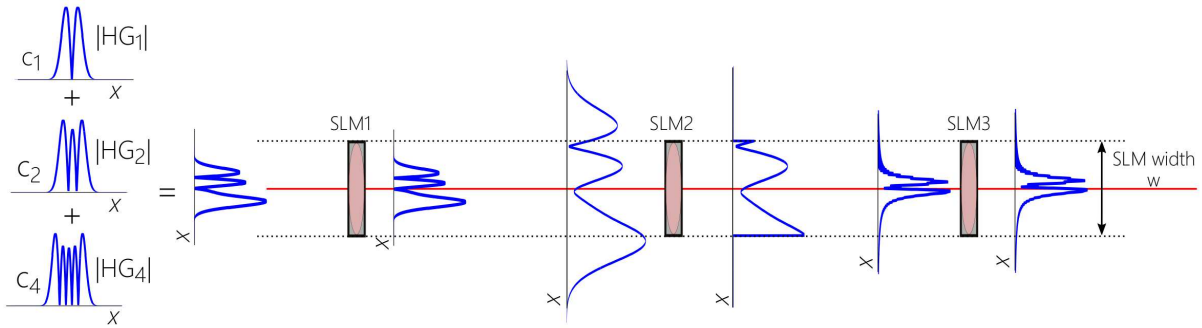

Figure 7.2: Progression of a beam obtained as the superposition of $\mathrm{HG}_1, \mathrm{HG}_2, \mathrm{HG}_4$ modes as it propagates, diffracts and gets clipped by the SLMs of the frFT filter. The SLM width is $w = 5$mm.

Clipping-cognizant measurement model

Many of the components used to implement an optical setup can be modeled as spacial cases of a Linear Canonical Transform (LCT) characterized by four parameters defining the parameter matrix $M = \begin{pmatrix} a & b \\ c & d \end{pmatrix}$ with unit determinant, i.e., $ad - bc = 1$, as,

$$\psi^M(u) = T^M\{\psi(x)\}(u) = \int_{-\infty}^{\infty} \psi(x) h^M(x,u) dx, \tag{7.3}$$

where,

$$h^M(x,u) = \sqrt{\frac{1}{j2\pi b}} \exp(\frac{j}{2b}(ax^2 - 2xu + du^2)) \tag{7.4}$$

for $b \neq 0$, and

$$\psi^M(u) = T^M\{\psi(x)\}(u) = \sqrt{d} \exp(j\frac{cdu^2}{2})\psi(du) \tag{7.5}$$

for $b = 0$ [94, 95, 96]. The notation $T^M\{\psi(.)\}$ denotes the LCT operator with parameter matrix M acting on input $\psi(.)$, and u represents the degree of freedom in the LCT domain.

Optical lenses, SLMs, and some of the commonly used linear operators such as Fourier transform, Fresnel integration and fractional Fourier transform are special cases of an LCT with different parameter matrices. For example, Fresnel integration used to approximate the short-range free-space diffraction in an optical setup is an LCT with $M = \begin{pmatrix} 1 & \frac{\lambda l}{2\pi} \\ 0 & 1 \end{pmatrix}$, where λ is the field wavelength and l is the free-space length.

To model an optical component with finite-aperture size w, we propose a *clipping LCT*, $T_w^M\{.\}(u)$, whose output for an incident beam $\psi(x)$ is equal to that of an ideal LCT acting on $\psi(x)$ multiplied by a rectangular function of width w, i.e., $T_w^M\{\psi(x)\}(u) = T^M\{\psi(x)\Pi(\frac{x}{w})\}(u)$. Leveraging the product property of the LCT, which describes the LCT of a product of two functions (see Appendix A), $T_w^M\{\psi(x)\}(u)$ gives,

$$\psi^M(u;w) = \frac{w}{2\pi|b|} e^{\frac{jd}{2b}u^2} \left((\psi^M(u) e^{\frac{-jd}{2b}u^2}) * \operatorname{sinc}\left(\frac{wu}{2\pi b}\right)\right), \tag{7.6}$$

where $*$ denotes convolution for $b \neq 0$ and,

$$\psi^M(u;w) = \sqrt{d} \exp\left(i\frac{cd}{2}u^2\right) \psi(du) \Pi\left(\frac{du}{w}\right), \tag{7.7}$$

for $b = 0$.

As mentioned earlier, the generalized delay operator is practically implemented using a cascade of optical components. For example, an frFT system analyzing the content of HG beams is realized using three SLMs separated by distances of $2f$ (see Fig. 3.3), where f is the focal distance of the lenses in the second arm of the interferometer. By the additivity property of LCTs [95], we can show that this system is equivalent to a cascade of five LCTs with parameter matrices $M_i = \begin{pmatrix} 1 & 0 \\ c_i & 1 \end{pmatrix}$, $i = 1, 2, 3$ (corresponding to an SLM with the

phase c_i), and $M = \begin{pmatrix} 1 & \frac{\lambda f}{\pi} \\ 0 & 1 \end{pmatrix}$ (modeling the Fresnel diffraction in free-space) as seen in the schematic of Fig.3.3. We model the SLMs using clipping LCTs given their finite-aperture size leading to the beam clipping illustrated in Fig.7.2.

In general, the fractional transform in the reference arm of the interferometer in any degree of freedom can be modeled as a cascade of regular and clipping LCTs. However, it is important to note that the Hilbert space basis elements $\{\phi_n(x)\}$ are no longer eigenfunctions of this transformation owing to the present clipping effect. We obtain a closed-form expression for the output of any combination of clipping and regular LCTs (see Lemma 2 to Lemma 5 in Appendix B). Accordingly, the output of the generalized delay for an input basis element $\phi_n(x)$, is $\mathcal{L}\{\phi_n(x)\} = e^{-in\alpha}\hat{\phi}_n(x;\alpha,\mathbf{w}),\ n = 1, 2, ..., N$, where $\mathbf{w}$ is a model parameter vector whose entries are the aperture sizes of the optical components (e.g., the widths $w_i,\ i = 1, 2, 3$, of the three SLMs in the frFT realization). As an example, following from Lemma 4 in Appendix B, the response of the frFT system of order α implemented using finite-aperture SLMs to HG_n, the n^{th} mode $\phi_n(x)$, is

$$\begin{aligned}\hat{\phi}_n(x;\alpha,\mathbf{w}) = \frac{w_1 w_2 |\csc\alpha|}{(\lambda l)^2}\Big[\Big(\exp\left(-j\frac{\pi\csc\alpha}{\lambda l}x^2\right) \\ \times\left(\phi_n(x)\exp\left(-j\frac{\pi\cot\alpha}{\lambda l}x^2\right) * \mathrm{sinc}\left(\frac{w_1 x\csc\alpha}{\lambda l}\right)\right)\Big) \\ * \mathrm{sinc}\left(\frac{w_2 x}{\lambda l}\right)\Big] \times \Pi\left(\frac{x}{w_3}\right)\exp\left(j\frac{\pi(\csc\alpha+\cot\alpha)}{\lambda l}x^2\right).\end{aligned} \tag{7.8}$$

Accordingly, the output of the reference arm is,

$$\psi(x;\alpha,\mathbf{w}) = \mathcal{L}\left\{\sum_{n=1}^{N} c_n\phi_n(x)\right\} = \sum_{n=1}^{N} c_n e^{-in\alpha}\hat{\phi}_n(x;\alpha,\mathbf{w}). \tag{7.9}$$

Hence, the interferogram as function of α is

$$\begin{aligned} I(\alpha;\mathbf{w}) =& < |\psi(x)|^2 > + < |\psi(x;\alpha,\mathbf{w})|^2 > \\ &+ < \psi(x)\psi^*(x;\alpha,\mathbf{w}) > + < \psi(x;\alpha,\mathbf{w})\psi^*(x) >, \end{aligned} \tag{7.10}$$

where the superscript * denotes the conjugate operator. The first term on the RHS of (7.10) is the input energy which is unity. The second term is the output energy of the reference arm, hereon denoted by $e_o(\alpha,\mathbf{w})$. From (7.9), the remaining terms on the RHS of (7.10) can be expanded as,

$$\begin{aligned} & 2\,\mathbb{R}\mathrm{e}\{\sum_{n=1}^{N} |c_n|^2 e^{in\alpha} \int_{-\infty}^{+\infty} \hat{\phi}_n(x;\alpha,\mathbf{w})\phi_n^*(x)dx\} \\ & + \sum_{n=1}^{N}\sum_{\substack{n'=1 \\ n'\neq n}}^{N} c_n c_{n'}^* (e^{-in\alpha} \int_{-\infty}^{+\infty} \hat{\phi}_n(x;\alpha,\mathbf{w})\phi_{n'}^*(x)\,dx \\ & + e^{in'\alpha} \int_{-\infty}^{+\infty} \phi_n(x)\hat{\phi}_{n'}^*(x;\alpha,\mathbf{w})\,dx)\,, \end{aligned} \tag{7.11}$$

where $\mathbb{R}\mathrm{e}\{.\}$ denotes the real part. Defining $g_{nn'}(\alpha;\mathbf{w}) := \int_{-\infty}^{+\infty} \hat{\phi}_n(x;\alpha,\mathbf{w})\phi_{n'}^*(x)\,dx$, the interferogram takes the form,

$$\begin{aligned} & I(\alpha;\mathbf{w}) = 1 + e_o(\alpha,\mathbf{w}) \\ & + 2\sum_{n=1}^{N} |c_n|^2 |g_{nn}(\alpha;\mathbf{w})| \cos(n\alpha + \angle g_{nn}(\alpha;\mathbf{w})) \\ & + \sum_{n=1}^{N}\sum_{\substack{n'=1 \\ n'\neq n}}^{N} c_n c_{n'}^* (e^{-in\alpha} g_{nn'}(\alpha;\mathbf{w}) + e^{in'\alpha} g_{n'n}^*(\alpha;\mathbf{w})). \end{aligned} \tag{7.12}$$

Defining the interferometric measurements $y(\alpha,\mathbf{w}) := \frac{1}{2}(I(\alpha,\mathbf{w}) - 1 - e_o(\alpha,\mathbf{w}))$, the mea-

surement model can be written in matrix form as

$$\mathbf{y} = \bar{\mathbf{A}}\mathbf{x} + \mathbf{B}\bar{\mathbf{x}}, \tag{7.13}$$

where $\mathbf{y} \triangleq [y(\alpha_1, \mathbf{w}), y(\alpha_2, \mathbf{w}), \ldots, y(\alpha_M, \mathbf{w})]^{\mathrm{T}}$, the $M \times N$ matrix $\bar{\mathbf{A}} \triangleq [|g_{nn}(\alpha; \mathbf{w})| \cos(n\alpha + \angle g_{nn}(\alpha; \mathbf{w}))]$, the $M \times N(N-1)$ matrix $\mathbf{B} \triangleq \frac{1}{2}[g_{nm}(\alpha_i; \mathbf{w}_i) + g^*_{mn}(\alpha_i; \mathbf{w}_i)]$, and $\bar{\mathbf{x}} \triangleq [c_1 d^*_2, c_1 d^*_3, \ldots, c_1 d^*_N, c_2 d^*_1, c_2 d^*_3, \ldots, c_N d^*_{N-1}]^{\mathrm{T}}$ is an $N(N-1) \times 1$ vector showing the interaction between the different modes. Since $\hat{\phi}_n(x; \alpha, \mathbf{w})$, $n = 1, 2, ..., N$, can be accurately calculated as in the frFT example of (7.8) from the lemmas derived in Appendix B, the sensing matrix $\bar{\mathbf{A}}$, and the coefficient matrix $\mathbf{B}$ in (7.13) are entirely accessible for modal recovery. To account for noise potentially contaminating the measurements, we also incorporate an additive white Gaussian noise term $\mathbf{z}$ whose entries have variance σ^2 to obtain the final measurement model

$$\mathbf{y} = \bar{\mathbf{A}}\mathbf{x} + \mathbf{B}\bar{\mathbf{x}} + \mathbf{z}\,. \tag{7.14}$$

Next, we develop a class of algorithms that are shown to bring about performance gains in modal reconstruction in presence of finite aperture effects by leveraging the clipping-cognizant model derived in (7.14).

Reconstruction methods

The previous analysis has revealed that the effect of aperture finiteness on the interferometric measurements is manifested in the sensing matrix $\bar{\mathbf{A}}$, the coefficient matrix $\mathbf{B}$, and the output energy $e_o(\alpha; \mathbf{w})$ of the reference arm. Therefore, a reconstruction method that takes advantage of prior information about these terms given the measurement model derived in (7.14) should yield more reliable recovery.

In an idealistic setting in which the measurement model is given by (7.2), a FT of interferometric measurements acquired by sampling the generalized delay α at Nyquist rate suffices to retrieve the modal energies, i.e., $\hat{\mathbf{x}} = |\mathbf{F}\mathbf{y}|$, where $\mathbf{F}$ is the discrete Fourier transform matrix, and $\hat{\mathbf{x}}$ contains the modal energies $|c_n|^2, n = 1, 2, \ldots, N$ of the input beam. Since in many modal analysis problems a large portion of the beam energy is carried by a small set of modes, i.e., the coefficient vector $\mathbf{x}$ is sparse, we devise sparse recovery algorithms to retrieve the modal content of optical beams in presence of clipping under the linear model in (7.14).

Our first method ignores the third term on the RHS of (7.12). In this case, the interferometric measurements are approximated by

$$\mathbf{y} \approx \bar{\mathbf{A}}\mathbf{x} + \mathbf{z}, \tag{7.15}$$

where $\bar{\mathbf{A}}$ is defined after (7.14). Under this assumption, we can readily use a denoising recovery algorithm such as the Dantzig selector [70] to recover the modal content, which solves

$$\begin{aligned} &\text{minimize } \|\hat{\mathbf{x}}\|_1 \\ &\text{subject to } \|\bar{\mathbf{A}}^{\mathrm{T}}(\bar{\mathbf{A}}\hat{\mathbf{x}} - \mathbf{y})\|_\infty \leq \eta\,\sigma, \end{aligned} \tag{7.16}$$

where η is a tuning parameter used to control the performance of reconstruction. We remark that although this method ignores terms derived in (7.12) pertinent to the present clipping, it still partially accounts for clipping captured in the definition of $\bar{\mathbf{A}}$ in (7.14) which is different from the ideal $\mathbf{A}$ in (7.2).

Nevertheless, seeking to further enhance the quality of reconstruction, our second method takes the effect of the term $\mathbf{B}\bar{\mathbf{x}}$ into consideration, hereon referred to as interference or noise

Algorithm 5 Iterative reconstruction algorithm

Input:

$\mathbf{y}$, $\mathbf{A}$, $\mathbf{B}$, σ

Initialization:

$\gamma = 0$, $\sigma' \leftarrow \sigma$

$\hat{\mathbf{x}} \leftarrow$ Solving Dantzig Selector with constraint:

$\|\bar{\mathbf{A}}^{\mathrm{T}}(\bar{\mathbf{A}}\hat{\mathbf{x}} - \mathbf{y})\|_{\infty} \leq \eta\,\sigma'$

While $\ell < L$

$\bar{\mathbf{x}} \leftarrow$ Estimating $\bar{\mathbf{x}}$ from $\hat{\mathbf{x}}$

$\gamma(\ell) = \sqrt{\frac{\sum_{i=1}^{N(N-1)} |\bar{x}_i|^2 \|\mathbf{b}_i\|^2}{M}}$ // Estimating an upper bound on the standard deviation

$\sigma' \leftarrow \sigma' + \gamma$ // Updating the constraint

$\hat{\mathbf{x}} \leftarrow$ Updating the estimate of $\mathbf{x}$ (solution of Dantzig selector)

if $|\gamma(\ell) - \gamma(\ell - 1)| \leq \zeta$, stop iterations

$\ell = \ell + 1$

end While

Output:

$\mathbf{x} = \hat{\mathbf{x}}$.

factor. To this end, one possibility is to estimate $\bar{\mathbf{x}}$, then subtract $\mathbf{B}\bar{\mathbf{x}}$ from the acquired measurements. However, this poses two main challenges. First, the vector $\mathbf{x}$ is unknown. Second, the relation between $\mathbf{x}$ and $\bar{\mathbf{x}}$ is not one-to-one, which makes it impossible to accurately estimate $\bar{\mathbf{x}}$ and exactly compute the term $\mathbf{B}\bar{\mathbf{x}}$ to eliminate it from the measurements even if $\mathbf{x}$ is known. As such, we propose an iterative reconstruction algorithm detailed in Algorithm 5, which uses the Dantzig selector as a core recovery procedure.

Algorithm 5 is initiated with an estimate of $\mathbf{x}$ obtained by solving (7.16). Then, an approximate upper bound on the standard deviation of $\mathbf{B}\bar{\mathbf{x}}$ is calculated as, $\gamma = \sqrt{\frac{\sum_{i=1}^{N(N-1)} |\bar{x}_i|^2 \|\mathbf{b}_i\|^2}{M}}$, where $|\bar{x}_i|$ is the i^{th} element of an approximate $|\bar{\mathbf{x}}|$, and $\|\mathbf{b}_i\|$ the ℓ_2-norm of the i^{th} column of $\mathbf{B}$. The magnitudes of the entries of $\bar{\mathbf{x}}$ are obtained from the approximate vector $\mathbf{x}$ calculated in the previous iteration. This upper bound is used to update the constraint in the Dantzig selector to $\eta\,(\sigma + \gamma)$ to improve reconstruction in the next iteration. The algorithm terminates when the difference between the γ's in two consecutive iterations falls below a threshold ζ, or when the number of iterations reaches a predefined maximum value L.

Numerical results

To study the effect of finite-aperture on the interferometry-based modal analysis problem, we consider the example of analyzing a light beam into its HG modes. For data generation, the interferometer is implemented using three SLMs of the same aperture size w, and the free-space propagation between the SLMs is modeled using Fresnel integration (see Fig. 3.3). The fidelity of this generative model has been confirmed by the agreement of the data with actual experimental measurements in [15]. In this example, the potential number of modes $N = 64$, and the beam energy is carried by $s = 4$ modes. To recover the modal energies in the inverse problem, we leverage the derived measurement model (7.14). Here, we define $\text{SNR} \triangleq 10 \log\left(\frac{\mathbb{E}[I(\alpha;\mathbf{w})^2]}{\sigma^2}\right)$, where $\mathbb{E}[.]$ stands for the expectation w.r.t. the distribution of the generalized delay α (here sampled from a uniform distribution $\mathcal{U}(0, 2\pi)$) and $I(\alpha, \mathbf{w})$ the interferogram in (7.12). We evaluate the recovery error as $e \triangleq \frac{\|\mathbf{x}-\hat{\mathbf{x}}\|_2^2}{\|\mathbf{x}\|_2^2}$, where $\hat{\mathbf{x}}$ is the reconstructed version of the sparse vector $\mathbf{x}$.

To validate the derived measurement model and further underscore the importance of accounting for the finite aperture effects, Fig. 7.3 displays the normalized distance, $\|\mathbf{I} - \hat{\mathbf{I}}\|_2/\|\mathbf{I}\|_2$, between the true measurements $\mathbf{I}$ (obtained from the generative forward model) and the predicted measurements $\hat{\mathbf{I}}$ for a range of increasingly refined measurement models. The green curve with square markers in Fig. 7.3 shows the normalized distance for the idealistic model (7.2), which completely ignores the clipping effect. The black curve with circle markers is for a model that only captures the output energy term $\mathbf{e_o}(\mathbf{w}) = [e_o(\alpha_1, \mathbf{w}), e_o(\alpha_2, \mathbf{w}), \ldots, e_o(\alpha_M, \mathbf{w})]^{\mathrm{T}}$ in (7.12) in accounting for the clipping, but otherwise ignores all other terms. The solid (red) curve further considers the modified sensing matrix $\bar{\mathbf{A}}$ as per (7.15), thus yields smaller error. Finally, the dotted blue curve corresponds to the most comprehensive model in (7.14), where all the clipping-related terms are accounted

for, i.e., the modified matrix $\bar{\mathbf{A}}$, the coefficient matrix $\mathbf{B}$, and the output energy of the frFT system $\mathbf{e_o}(\mathbf{w})$. Fig. 7.3 indicates that the model in (7.14) well captures the effect of the finite aperture. Consequently, it is expected that more accurate recovery of the modal content of the input beam can be achieved by leveraging this model.

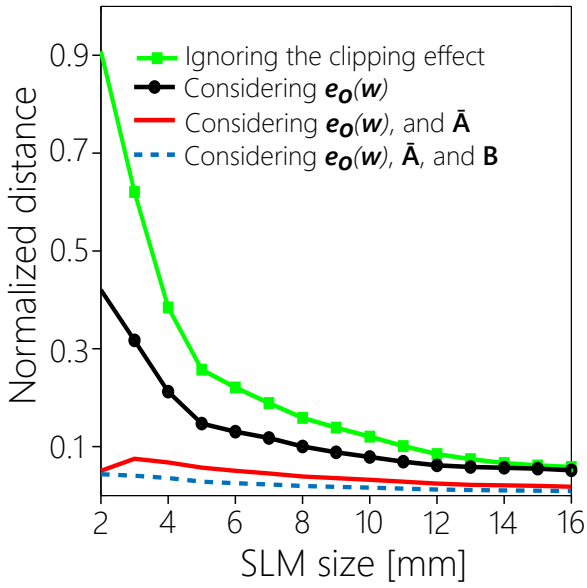

Figure 7.3: Measurement model error in presence of clipping effect.

Next, we investigate the reconstruction performance with clipping-cognizant recovery. Fig. 7.4 shows the reconstruction error of the FT-based reconstruction versus the SLM size. Rather than the FT of $\frac{1}{2}\mathbf{I}(\mathbf{w}) - \mathbf{1}$, we reconstruct the sparse vector $\hat{\mathbf{x}} = |\mathbf{F}(\frac{1}{2}\{\mathbf{I}(\mathbf{w}) - \mathbf{1} - \mathbf{e_o}(\mathbf{w})\})|$, where $\mathbf{I}(\mathbf{w}) = [I(\alpha_1, \mathbf{w}), I(\alpha_2, \mathbf{w}), \ldots, I(\alpha_M, \mathbf{w})]^{\mathrm{T}}$ and $\mathbf{1}$ is a vector of all ones. Therefore, we provide a first level of compensating for the clipping effect by accounting for the the output energy term $\mathbf{e_o}(\mathbf{w})$. As shown in Fig.7.4, considering the clipping effect (red curve) reduces the reconstruction error and improves the quality of modal recovery.

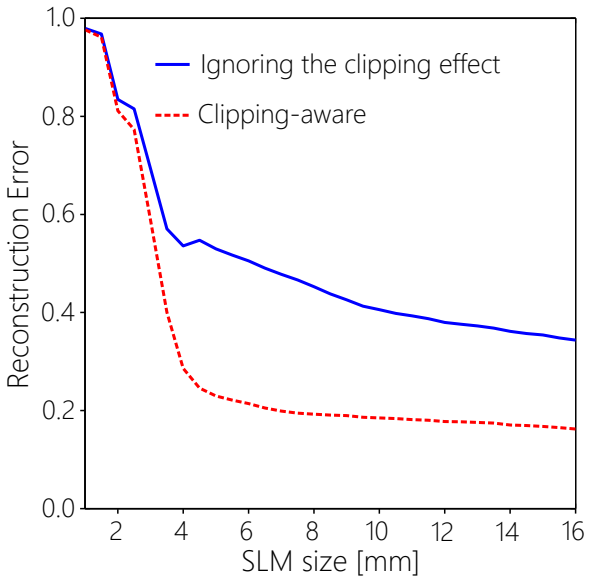

Figure 7.4: FT-based modal recovery and considering the clipping effect, reconstruction error versus SLM size.

Figs. 7.5 (a) and 7.5 (b) show the reconstruction error of the proposed modal analysis approach versus the SLM size while adopting the CS-based recovery algorithms. As shown, accounting for the output energy of the frFT system and the modified sensing matrix $\bar{\mathbf{A}}$ as per measurement model (7.15) greatly improves the quality of recovery over the idealistic model in (7.2), where the finite-aperture effect is ignored.

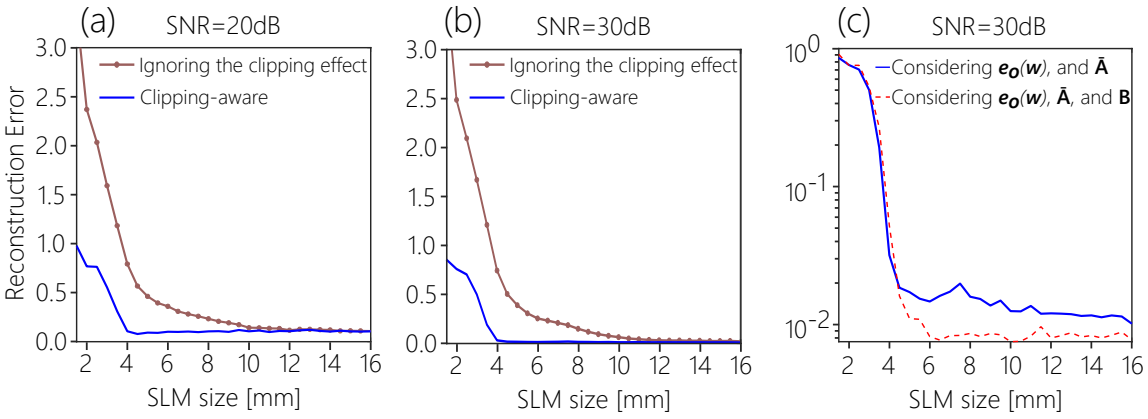

Figure 7.5: Comparing reconstruction performance of the CS based approach with considering the clipping terms $\mathbf{e_o}(\mathbf{w})$, and $\bar{\mathbf{A}}$ to that of the case in which the clipping effect is ignored. (a) SNR=20dB. (b) SNR=30dB. (c) Comparing the reconstruction error of the iterative algorithm to that of the regular CS based algorithm where the term $\mathbf{B}\bar{\mathbf{x}}$ is ignored, SNR=30dB.

To further improve the quality of reconstruction, we consider the more comprehensive measurement model in (7.14), which also incorporates the derived $\mathbf{B}\bar{\mathbf{x}}$ and uses the proposed iterative recovery algorithm described in Algorithm 5. Fig. 7.5 (c) shows that Algorithm 5 yields further improvement in recovering the modal content of the incident light beam. Fig. C.8 shows a significant improvement in the recovery of the modal energies using Algorithm 5 versus a Dantzig selector that ignores the clipping effect.

CHAPTER 8: THE EFFECT OF HARDWARE LIMITATIONS ON THE PROPERTIES OF SPATIAL-TEMPORAL LIGHT BEAMS

Introduction

In the previous chapters, we studied the effect of hardware limitations and sensing constraints of the data acquisition systems on the performance of signal reconstruction. In this Chapter, we study such limitations one step before collecting measurements, where a reference light field is generated to illuminate a sample object in the active imaging systems [19]. In such data acquisition systems, measurements are samples of the scattered, diffused, or reflected light field [34]. Spatial-temporal diffraction-free beams, newly introduced in [35, 36], are provably able to propagate for large distances with no or small diffraction. This favorable property makes them attractive candidates in active data acquisition systems, in which the scattered field of an active light source is used to recover information about objects of interest.

Theory of ST-beams

In general, a one dimensional polychromatic light filed can be written as a superposition of plane waves as,

$$E(x,z;t) = \int\int F(k_x,\omega)e^{ik_x x}e^{ik_z z}e^{-i\omega t}d\omega dk_x, \tag{8.1}$$

where x and z determine the location along the transverse, and the propagation axes, respectively, and t stands for the time. Temporal frequency is represented by ω, and spatial frequencies along x and y directions are shown by k_x and k_z, receptively. Here, $F(k_x,\omega)$ is

the spectrum of the light field which is the Fourier transform of the field at $z = 0$. For a separable and regular Gaussian light beam, this spectrum can take the form of,

$$F(k_x, \omega) = F_1(k_x).F_2(\omega), \tag{8.2}$$

where $F_1(k_x)$ and $F_2(\omega)$ can be two independent Gaussian functions of k_x, ω, respectively.

Based on the theory of spatial-temporal light beams introduced in [35], one can generate diffraction-free beams by introducing a correlation between the spatio-temporal degrees of freedom of the beam. As such, only one spatial frequency k_x is assigned to one temporal frequency ω via an appropriate class of one to one functions [36]. Based on the theory of ST-beams, these one-to-one functions can be conic sections created by intersecting the light cone and the spectral planes with the angle θ with respect to the k_z axis as shown in Fig. 8.1. The green curve in this Figure is a trajectory in the spectrum domain relating the temporal and spatial degrees of freedom of the beam as a hyperbola, parabola, or ellipse, depending on the intersection angle. The spectrum of an ideal ST-beam can then be formulated as,

$$F(k_x, \omega) = F_1(k_x).\delta(\omega - g(k_x)). \tag{8.3}$$

Where, $\delta(.)$ is Dirac delta function, and $g(.)$ is a conic function providing a one-to-one relation between $|k_x|$, and ω. This conic function is acquired by intersecting the light cone $k_z = \sqrt{(\omega/c)^2 - k_x^2)}$, and the spectral plane $\frac{\omega}{c} = \beta + (k_z - \beta)\tan\theta$ which forms a conic equation as,

$$\frac{(\frac{\omega}{c} - \frac{\beta}{1+\tan\theta})^2}{\frac{\beta^2\tan^2\theta}{(1+\tan\theta)^2}} - \frac{k_x^2}{\frac{\beta^2(\tan\theta-1)}{1+\tan\theta}} = 1, \tag{8.4}$$

where β is a constant and c is the speed of light in free space. Figure 8.2 shows two examples of the ST-beams generated by intersecting the light cone with the spectral planes with

$\theta = \pi/3$, and $\theta = \pi/6$, which form Hyperbola and elliptical trajectories, respectively. As seen in Fig. 8.2 (c) and (f) the profile of the beams almost remain unchanged after 20mm traveling along the z axis.

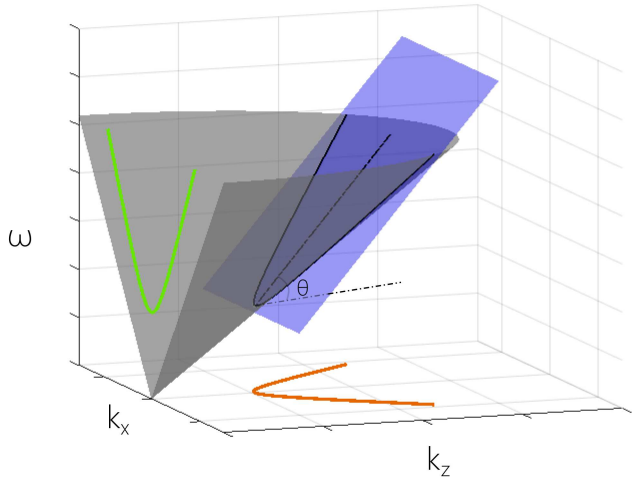

Figure 8.1: Intersection of the light cone and a spectral plane.

ST-beams behavior after hitting a blocker

Diffraction-free nature of ST-beams makes them a potential candidate for optical imaging applications in which a light filed, used to illuminate the sample object, should travel into a scattering medium such as a living tissue [43]. As the energy of the ST-beams remains focused during the propagation, they can penetrate more deeply in a sample object. To study how the ST-beams behaves in the scattering environments, and figure out how the information about such environments is embedded in the scattered filed, we examine their behavior in presence of a one dimensional optical blocker as a very simple model for the scattering environments.

Figure 8.3 shows the behavior of a ST-beam, where the intersection angle $\theta = \pi/6$ and

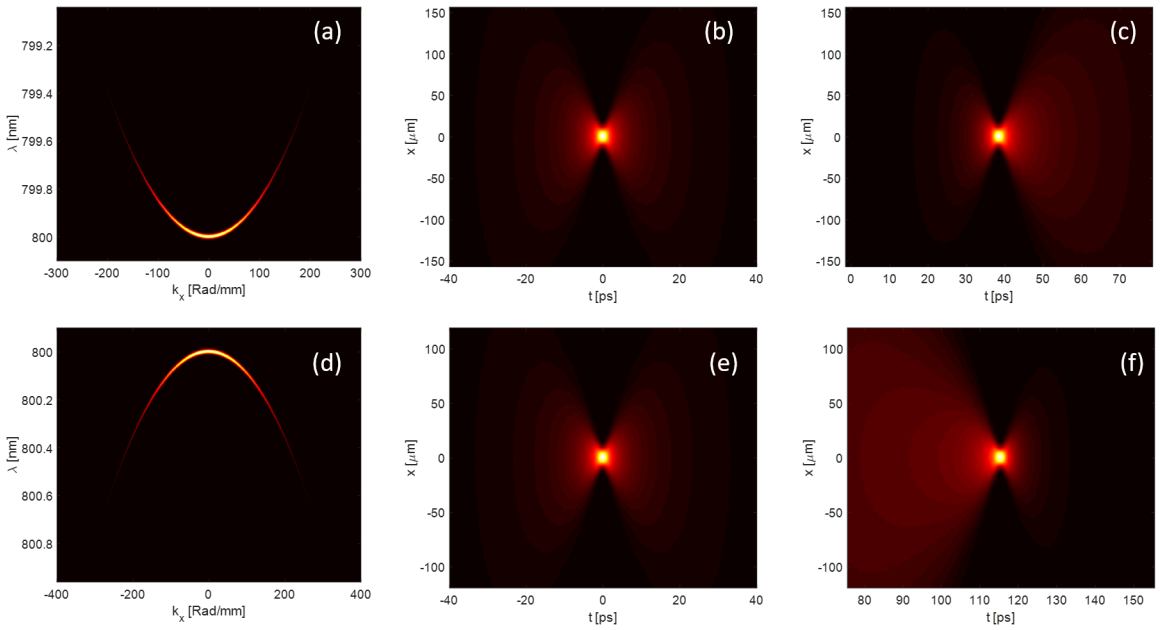

Figure 8.2: Spectrum of a ST-beam with the intersection angle $\theta = \pi/3$, (e) its intensity at $z = 0$mm, (f) $z = 20$mm.(d) Spectrum of a ST-beam with the intersection angle $\theta = \pi/6$, (e) its intensity at $z = 0$mm, (f) $z = 20$mm.

$\pi/3$. As seen, the scattered beam pattern is different when the light beam hits blockers with different sizes. This shows that the information regarding the width of the blocker is embedded in the profile of the scattered light beam. These Figures also reveals another property of the ST beams. As see, the scattered light field starts to be focused again after traveling some distance from the blocker. This property of the ST-beams is called *self-healing*.

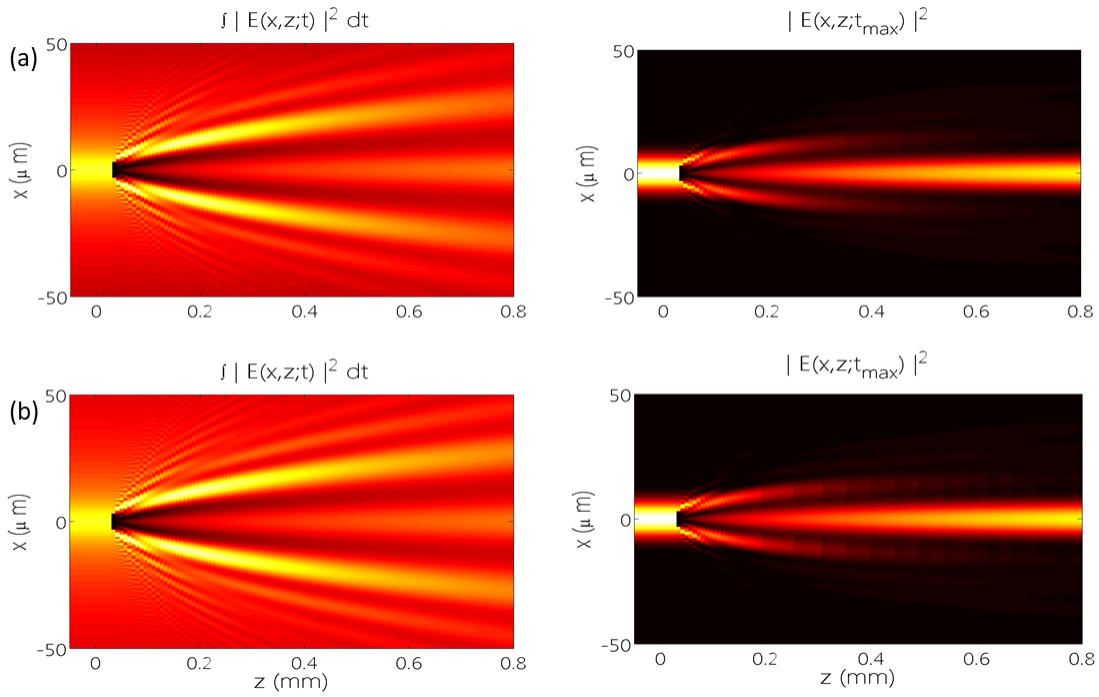

Figure 8.3: Intensity of the light field ($\int |E(x,z;t)|^2 dt$, and $|E(x,z;t=0)|^2$) along the propagation axis, where row (a) shows the results for a ST-beam with $\theta = \pi/6$, and bandwidth $\Delta\lambda = 0.17$nm, and row (b) represents the results for a ST-beam with $\theta = \pi/3$, and bandwidth $\Delta\lambda = 0.29$nm.

We can analytically show these two properties of the ST-beams by deriving the light field equation after hitting the blocker. To this end, we consider a specific case of the ST-beams where the intersection angle $\theta = \pi/2$. Considering general plane wave expansion (8.1), the light field equation before the blocker takes the form of,

$$E_i(x,z;t) = e^{i\beta z} \int F(k_x) e^{ik_x x} e^{-ig(k_x)t} dk_x, \tag{8.5}$$

where, $g(k_x) = c\sqrt{(k_x^2 + \beta^2)}$. Modeling the blocker as an optical component with the transmittance $1 - \Pi(\frac{x}{L})$, the scattered light field would be,

$$\begin{aligned} E_o(x, z; t) = & 2\pi e^{i\beta z} \int F(k_x) e^{ik_x x} e^{-ig(k_x)t} dk_x \\ & - L \int \int F_1(g^{-1}(\omega)) \operatorname{sinc}(\frac{L(1 - g^{-1}(\omega))}{2\pi}) e^{ik_z z} e^{ik_x x} e^{-i\omega t}, \end{aligned} \tag{8.6}$$

where, $g^{-1}(\omega) = \sqrt{(\omega/c)^2 - \beta^2}$. In the right hand side of (8.6), the first term is a same copy of the input beam which shows the self-healing property of the ST-beams, and the second term is a diffractive field containing information about the blocker. Hence, off-axis measurements can be considered as observations in an inverse problem in which the information of the scattering object is of interest.

The hardware setup used to generate ST-beams and its limitations

Figure 8.4 shows a schematic for the practical setup used to generate the ST-beams [36]. As seen in this Figure, a polychromatic pulsed plane wave is passed through a diffraction grating by which the beam temporal frequencies, ω's, are decomposed spatially in y direction. Then, a spatial phase modulator such as a SLM is used to assign an appropriate k_x to each wavelength. The slope of the phase of the SLM at each x, and y is defined based on the intersection angle θ, and considering the one-to-one relation between ω's and k_x's defined by (8.4). After passing through the SLM, the light fields with wavelengths are again combined using another grating to form a ST-beam.

Hardware limitations

To generate an ideal ST-beam, the optical setup shown in Fig. 8.4 [36] should be implemented using ideal components, so that only one spectral frequency k_x is assigned to a temporal frequency ω. Hence, the first grating should perfectly separate all wavelengths of the beam spatially in y direction to guarantee that only one wavelength is present at each location along the y-axis. In addition, the pixel size of the SLM, and the number of its quantization levels should ideally goes to zero and infinitely, respectively. Among these limitations, the finite width of the grating has the most destructive effect on the quality of the generated ST-beams. The limited size of the first diffraction grating results in each wavelength to spread along the y-axis and overlap with the adjacent wavelengths.

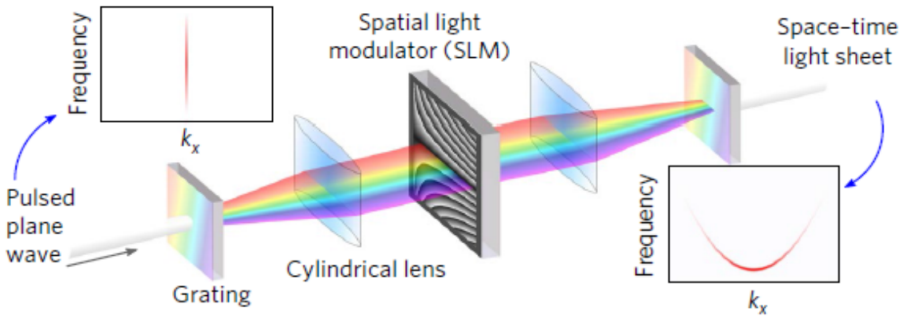

Figure 8.4: The hardware setup used to generate ST-beams (Figure from [36], p. 735).

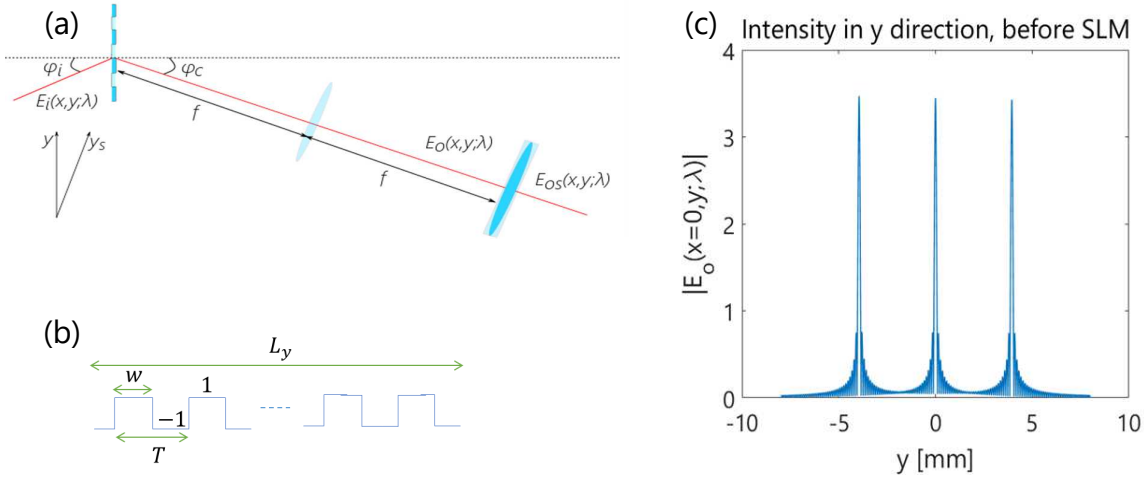

Figure 8.5: (a) Schematic of the first half of the hardware setup. (b) Mathematical model of the gratings. (c) The beam intensity right before the SLM, where the input plane wave contains three different wavelengths.

To show the effect of the limited-size grating on the properties of a ST-beam, we model the grating as a train of rectangular functions along y-axis as shown in Schematic 8.5 (b), and calculate the beam equation right before the SLM. Assuming the input light field to be a monochromatic plane wave with wavelength λ hitting the grating at the input angle ϕ_i, the grating output filed in y direction takes the form of,

$$E(y;\lambda) = \sum_{n=-\infty}^{+\infty} c_n \exp(\frac{i2\pi ny}{w}).\Pi(\frac{y}{L_y}) \exp(i\frac{2\pi}{\lambda} y \sin\phi_i), \tag{8.7}$$

where, w and L_y are the width of a rectangular functions and the width of the grating in y direction, respectively, and c_n's are the Fourier series coefficients of the train rectangular function modeling the gratings. After passing through the first free space–Lens–free space system acting as a weighted and scaled Fourier transform, the light wave equation right

before the SLM would be proportional to,

$$E_o(y;\lambda) \propto \text{sinc}(\frac{yL_y \cos\phi_c}{\lambda f} - \frac{nL_y}{w} - \frac{L_y \sin\phi_i}{\lambda}), \tag{8.8}$$

where, f is the focal length of the cylindrical lens, and ϕ_c is the grating output angle. Figure 8.5 (c) shows the beam before the SLM for three different wavelengths. As seen, the profile of the beams along the y-axis takes the form of sinc functions with non-zero width. This means that several spatial frequencies are assigned to a single wavelength which violates the key underlying idea behind generating the ST-beams. This unwanted effect stemming from finite width of the grating L_y is modeled as an *spectrum uncertainty* $\delta\lambda$ in the spectrum of the ST-beams.

For an ideal ST-beam, we assumed that $F(k_x, \omega) = F_1(k_x)\delta(\omega - g(k_x))$, where $g(k_x)$ holds a one-to-one relation between $|\omega|$ and k_x. Considering the effect of the grating with limited size, we need to replace the ideal delta function with a more realistic function whose width is determined by the spectrum uncertainty $\delta\lambda$. As a candidate, we can use a Gaussian function whose center is at $g(k_x)$, and its width is a known function of spectrum uncertainty $\delta\lambda$. So, the spectrum of a practical ST-beam can be modeled as,

$$F(k_x, \omega) = F_1(k_x) \exp(\frac{(\frac{2\pi c}{\omega} - \frac{2\pi c}{g(k_x)})^2}{h(\delta\lambda)}), \tag{8.9}$$

where, $h(.)$ is a known function.

The effect of spectrum uncertainty on the properties of ST-beams

Group velocity: Defining the group velocity of a light beam as $v_g = \frac{d\omega}{dk_z}$, the group velocity of an ideal ST-beam based on the plane equation $\frac{\omega}{c} = \beta + (k_z - \beta)\tan\theta$ would be,

$$v_g = c\tan\theta, \tag{8.10}$$

which could be bigger or less than the speed of light in free space c (superluminal, or subluminal, respectively). However, our calculations show that the speed of the ST-beams is highly constrained by the spectrum uncertainty.

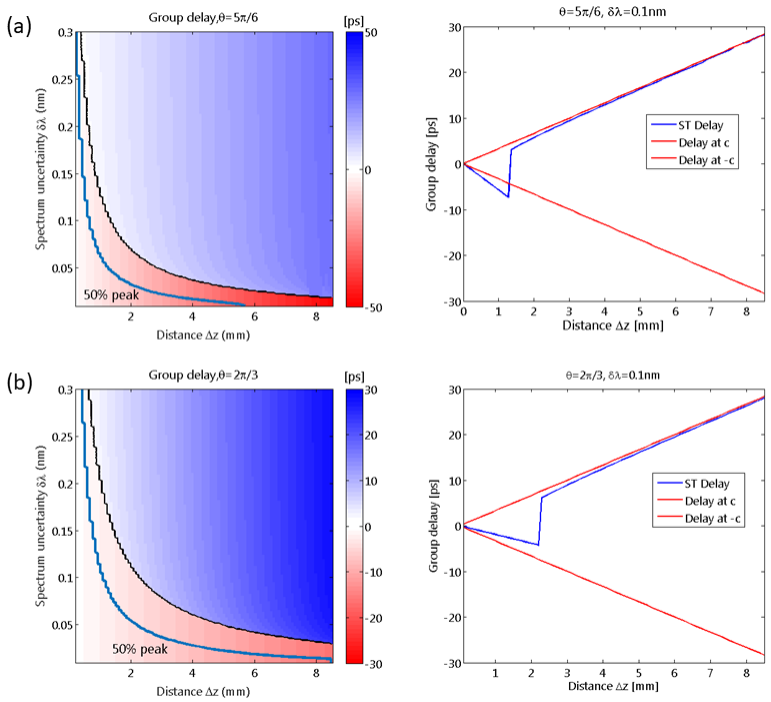

Figure 8.6: Group delay as a function of spectrum uncertainty and the propagation distance. Row (a) shows the results for the intersection angle $\theta = 5\pi/6$, and row (b) represents the results for $\theta = 2\pi/3$.

Figure 8.6 shows the group delay of the ST-beams with $\theta = 5\pi/6$, and $\theta = 2\pi/3$ as a function

of the propagation distance and spectrum uncertainty. As seen, higher spectrum uncertainty forces the ST-beams to converge to c in shorter distances from the source. The theory behind this behavior has been explained in [97].

Propagation and tail lengths: Being diffraction-free is the main motivation to generate ST-beams. However, this property is significantly affected by the spectrum uncertainty stemming from the hardware limitations discussed earlier. As seen in Fig. 8.7, increasing the spectrum uncertainty results in the beam to diffract faster and travel a shorter distance. The same results have been shown in 8.8 in terms of the traveling distance and the tail-length of the beam versus the amount of spectrum uncertainty. This Figure shows that we can play with the spectrum uncertainty to control the propagation distance and the beam width.

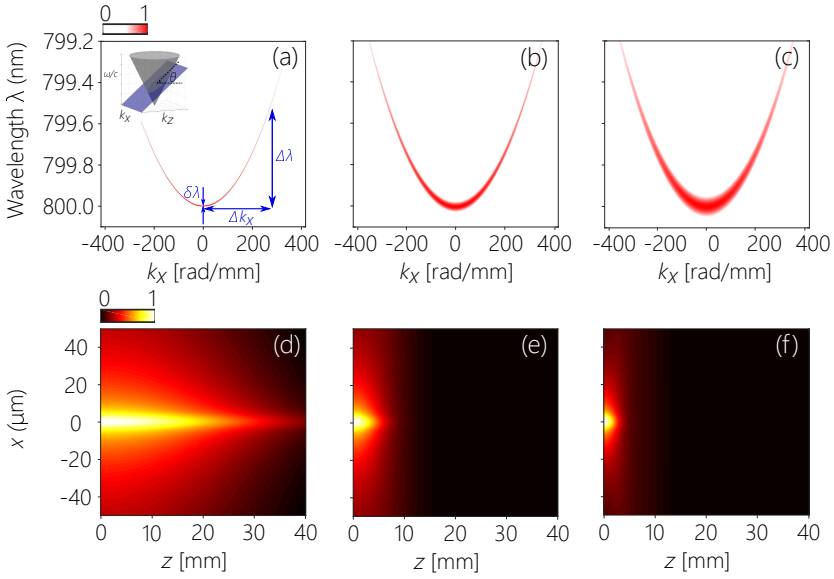

Figure 8.7: (a) Inset shows a schematic for the plane-cone intersection with angle θ with respect to k_z axis. This Figure shows the spectrum of a ST beam with the spectrum uncertainty $\delta\lambda = 5$pm, (b) $\delta\lambda = 35$pm, and (c) $\delta\lambda = 70$pm. (d)-(f) Intensity of the light beam $\int |E(x,z;t)|^2 dt$ where $\delta\lambda = 5$pm, 35pm, and 70pm, respectively. The bandwidth $\Delta\lambda = 0.5$nm, initial FWHM $x_0 = 5\mu$m, and $\theta = \pi/2$.

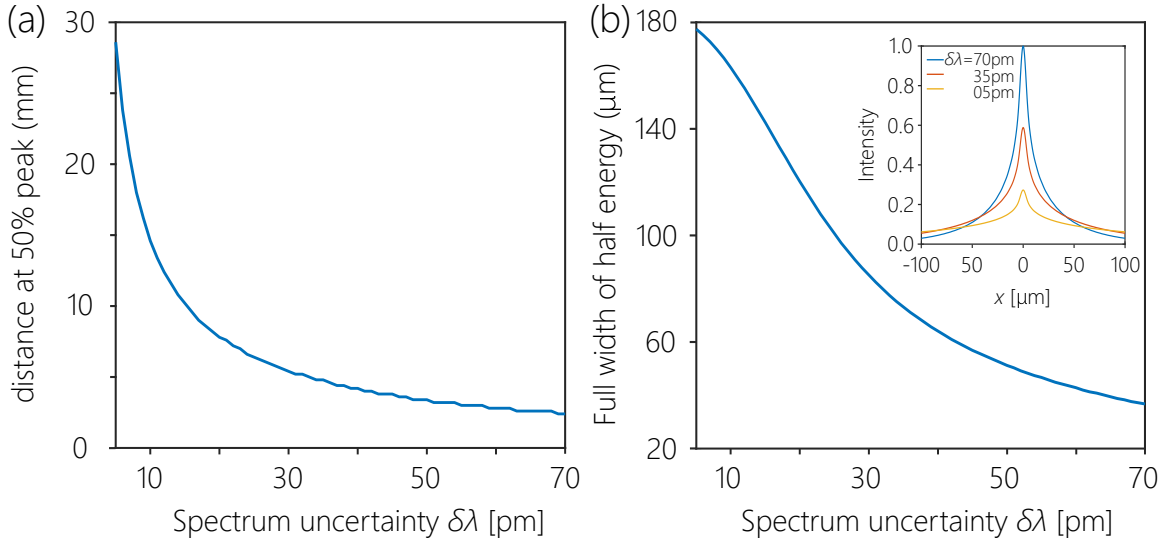

Figure 8.8: (a) This Figure shows the distance at which the beam peak drops to 50% of the initial peak for different values of the spectrum uncertainty $\delta\lambda$. As an criterion for propagation length, the distance at 50% peak decreases for larger values of spectrum uncertainty. (b) The full width of half energy is shown here as the tail length of the beam for different values of the spectrum uncertainty. The beam would be more focused in the center as $\delta\lambda$ is large. Inset shows the initial beam intensity for $\delta\lambda = 5$pm, 55pm, and 70pm.

Hardware limitations and its effect on information recovery performance

As seen, hardware limitations have undeniable effects on different properties of ST-beams. Assuming that one uses this class of diffraction-free beams for imaging and sampling applications, such physical constraints can affect the quality of information recovery as well. Most of these effects are destructive which can be captured in the measurement model and compensated via appropriate recovery algorithms. However as observed in the previous section, we can also look at these limitations as extra degrees of freedom to control the beam properties.

APPENDIX A: PRODUCT PROPERTY OF LCTS

Lemma 4. *Let $s(x)$ and $g(x)$ be two signals or light beams*[1]*. The LCT of their product, $\psi(x) = s(x) \cdot g(x)$, with real parameter matrix $M = \begin{pmatrix} a & b \\ c & d \end{pmatrix}$ is given by,*

$$\begin{aligned} T^M\{\psi(x)\}(u) &= \psi^M(u) \\ &= \frac{1}{2\pi|b|} e^{i\frac{d}{2b}u^2} [\big(s^M(u) e^{-i\frac{d}{2b}u^2}\big) * g^{FT}(\frac{u}{2\pi b})] \\ &= \frac{1}{2\pi|b|} e^{i\frac{d}{2b}u^2} [\big(g^M(u) e^{-i\frac{d}{2b}u^2}\big) * s^{FT}(\frac{u}{2\pi b})], \end{aligned} \tag{A.1}$$

for $b \neq 0$ and,

$$T^M\{\psi(x)\}(u) = \sqrt{d} e^{i\frac{cd}{2}u^2} s(du) g(du) \tag{A.2}$$

for $b = 0$. Here, $s^M(u)$ ($g^M(u)$) and $s^{FT}(u)$ ($g^{FT}(u)$) are the LCT and Fourier transform of $s(x)$ ($g(x)$), respectively.

Proof. The proof of (A.2) follows directly from the definition of LCTs with $b = 0$. To prove (A.1), we follow the same procedure used in [98] to establish the product property of the fractional Fourier Transform. We start by the definition of LCTs as,

$$\begin{aligned} T^M\{s(x) \cdot g(x)\}(u) &= \int_{-\infty}^{\infty} (s(x) \cdot g(x)) \\ &\times \sqrt{\frac{1}{i2\pi b}} \exp\big(\frac{i}{2b}(ax^2 - 2xu + du^2)\big) dx. \end{aligned} \tag{A.3}$$

Replacing $s(x)$ with the Inverse Linear Canonical Transform (ILCT) of its LCT, $s^M(\hat{u})$, with

[1]In this Appendix, we use the material published in Journal of the Optical Society of America A (JOSA A), 2018 [11].

parameter matrix $\begin{pmatrix} d & -b \\ -c & a \end{pmatrix}$, we have,

$$
\begin{aligned}
&T^M\{\psi(x)\}(u) = \psi^M(u) \\
&= \int_{-\infty}^{\infty} \Big(g(x) \times \sqrt{\frac{1}{i2\pi b}} \exp\big(\frac{i}{2b}(ax^2 - 2xu + du^2)\big) \\
&\times \int_{-\infty}^{\infty} s^M(\hat{u}) \sqrt{\frac{-1}{i2\pi b}} \exp\big(\frac{-i}{2b}(d\hat{u}^2 - 2x\hat{u} + ax^2)\big) d\hat{u} \Big) dx \\
&= \frac{\exp(\frac{id}{2b}u^2)}{2\pi|b|} \int_{-\infty}^{\infty} s^M(\hat{u}) \exp(\frac{-id}{2b}\hat{u}^2) \\
&\times (\int_{-\infty}^{\infty} g(x) \exp(\frac{-i}{2\pi b} 2\pi x(u - \hat{u}))dx) d\hat{u}.
\end{aligned}
\tag{A.4}
$$

Here, the degree of freedom in the LCT domain of $s(x)$ is denoted $\hat{u}$. As seen, the integral with respect to x is actually the Fourier Transform of $g(x)$, where the variable in the Fourier domain is replaced by $\frac{(u-\hat{u})}{2\pi b}$. Therefore, the LCT is,

$$
\begin{aligned}
&\psi^M(u) = \frac{\exp(\frac{id}{2b}u^2)}{2\pi|b|} \\
&\times \int_{-\infty}^{\infty} s^M(\hat{u}) \exp(\frac{-id}{2b}\hat{u}^2) g^{FT}(\frac{u - \hat{u}}{2\pi b}) d\hat{u} \\
&= \frac{\exp(\frac{id}{2b}u^2)}{2\pi|b|} [(s^M(u) \exp(\frac{-id}{2b}u^2)) * g^{FT}(\frac{u}{2\pi b})].
\end{aligned}
\tag{A.5}
$$

The last equation in (A.5) provides the LCT of the product of two signals in closed-form. Alternatively, this closed-form expression can be written as,

$$
\psi^M(u) = \frac{e^{(\frac{id}{2b}u^2)}}{2\pi|b|} [(g^M(u) e^{(\frac{-id}{2b}u^2)}) * s^{FT}(\frac{u}{2\pi b})], \tag{A.6}
$$

by switching the roles of $s(t)$ and $g(t)$ in (A.4) and replacing $g(t)$ with the ILCT of $g^M(\hat{u})$. This shows the *commutative property* for the LCT of a product. □

This property is used to define the output signal of a clipping LCT, where the clipping effect is modeled as the multiplication of the input beam with a rectangular function.

APPENDIX B: OUTPUT OF A CASCADE OF CLIPPING LCTS

To analyze the output beam of different combinations of regular and clipping LCTs, we first establish the *clipping additivity property*[1]. Based on this property, the output beam of a system consisting of a regular LCT with parameter matrix M_1 and a clipping LCT of width w with parameter matrix M_2 for the input beam $\psi(x)$ is equal to the output beam of a clipping LCT with width w and parameter matrix M_2M_1 as,

$$T^{M_2}\big\{T_w^{M_1}\{\psi(x)\}(u_1)\big\}(u_2) = T_w^{M_2M_1}\{\psi(x)\}(u_2), \tag{B.1}$$

where $M_1 = \begin{pmatrix} a_1 & b_1 \\ c_1 & d_1 \end{pmatrix}$, $M_2 = \begin{pmatrix} a_2 & b_2 \\ c_2 & d_2 \end{pmatrix}$ and $b_1 \neq 0$, $b_2 \neq 0$. This property follows from the definitions of regular and clipping LCTs.

In the proposed basis analysis approach, the generalized phase operator system can be implemented using a cascade of optical components modeled as regular and clipping LCTs.

Next, we establish several lemmas to capture the clipping effect at the output of systems implemented by clipping LCTs. First, we introduce some additional notation. For $\ell = 1, 2, \ldots, L$, we define $M_{L\ell} \triangleq M_L M_{L-1} \ldots M_\ell = \begin{pmatrix} a_{L\ell} & b_{L\ell} \\ c_{L\ell} & d_{L\ell} \end{pmatrix}$, and $M_{LL} \triangleq M_L$, where $M_\ell = \begin{pmatrix} a_\ell & b_\ell \\ c_\ell & d_\ell \end{pmatrix}$. We also define the recursive operator equations,

$$\begin{aligned} \kappa_n\big\{\psi(x); \{M_{L\ell}\}_\ell, \{w_\ell\}_\ell\big\}(u) &= \exp\left(i\Big(\frac{d_{Ln}}{2b_{Ln}} - \frac{d_{L(n+1)}}{2b_{L(n+1)}}\Big)u^2\right) \\ &\times \Big[\kappa_{n-1}\big\{\psi(x); \{M_{L\ell}\}_\ell, \{w_\ell\}_\ell\big\}(u) * \mathrm{sinc}(\frac{w_n u}{2\pi b_{Ln}})\Big],\ n = 2, 3, \ldots, L \end{aligned} \tag{B.2}$$

[1]In this Appendix, we use the material published in Journal of the Optical Society of America A (JOSA A), 2018 [11].

where,

$$\kappa_1\big\{\psi(x);\{M_{L\ell}\}_\ell,\{w_\ell\}_\ell\big\}(u)=\exp\left(i\Big(\frac{d_{L1}}{2b_{L1}}-\frac{d_{L2}}{2b_{L2}}\Big)u^2\right)$$
$$\times\left(T^{M_{L1}}\{\psi(x)\}(u)\exp\Big(-i\frac{d_{L1}}{2b_{L1}}u^2\Big)*\operatorname{sinc}\Big(\frac{w_1u}{2\pi b_{L1}}\Big)\right), \tag{B.3}$$

and $\{.\}_\ell$ is a set indexed by $\ell=1,2,...,L$.

1. The next lemma calculates the output of a system formed by a cascade of L clipping LCTs with $b_\ell\neq 0,\ \ell=1,2,\ldots,L$.

   Lemma 5. *Let $\psi(x)$ be the input beam of L clipping LCTs with $M_\ell=\begin{pmatrix}a_\ell & b_\ell\\ c_\ell & d_\ell\end{pmatrix}$, $\ell=1,...,L$ and $b_\ell\neq 0$. Then, the output of this cascade system is given by,*

$$\psi_o(u)=\left(\prod_{\ell=1}^{L}\frac{w_\ell}{2\pi|b_{L\ell}|}\right)$$
$$\times\kappa_L\big\{\psi(x);\{M_{L\ell}\}_\ell,\{w_\ell\}_\ell\big\}(u),\ \ell=1,2,\ldots,L, \tag{B.4}$$

   where $T^{M_{L1}}\{.\}(u)$ is the linear system equivalent to the cascade of L regular LCTs and κ_L is defined through the recursion in (B.2) and (B.3).

   Proof. The proof of Lemma 5 follows directly from the definition of clipping LCTs and the clipping additivity property in (B.1). □

2. The following lemma calculates the output of a sequence of L chirp multiplications and scaling systems – equivalently LCTs with zero b parameter – with finite-aperture size (e.g., useful in modeling lenses).

Lemma 6. *Let $\psi(x)$ be the signal or light beam input to a cascade of L clipping LCTs with parameter matrices $M_\ell = \begin{pmatrix} a_\ell & 0 \\ c_\ell & d_\ell \end{pmatrix}$, $\ell = 1, \ldots, L$. Then, the output signal $\psi_o(u)$ is given by,*

$$\begin{aligned} \psi_o(u) &= T^{M_L M_{L-1} \ldots M_2 M_1}\{\psi(x)\}(u) \\ &\quad \times \Pi\left(\frac{u}{\min\{\frac{w_1}{|d_{L1}|}, \frac{w_2}{|d_{L2}|}, ..., \frac{w_L}{|d_L|}\}}\right). \end{aligned} \tag{B.5}$$

Proof. From the definition of the clipping LCT with $b_\ell = 0$, for $\ell = 1, 2, \ldots, L$, we have,

$$\begin{aligned} \psi_o(u) &= T_{w_L}^{M_L}\left\{T_{w_{L-1}}^{M_{L-1}}\left\{ \ldots \{T_{w_1}^{M_1}\{\psi(x)\}\}\right\}\right\}(u) \\ &= \sqrt{d_L d_{L-1} \ldots d_3 d_2 d_1}\exp\big(i\frac{d_L d_{L-1} \ldots d_3 d_2 d_1}{2}u^2 \\ &\quad \times \big(\frac{c_L}{d_{L-1} d_{L-2} \ldots d_3 d_2 d_1} + \frac{c_{L-1} d_L}{d_{L-2} \ldots d_3 d_2 d_1} + \ldots \\ &\quad + \frac{c_2 d_L d_{L-1} \ldots d_3}{d_1} + c_1 d_L d_{L-1} \ldots d_3 d_2)\big) \\ &\quad \times \psi(d_L d_{L-1} \ldots d_3 d_2 d_1 u) \\ &\quad \times \Pi\left(\frac{u}{\min\{\frac{w_1}{|d_L d_{L-1} \ldots d_3 d_2 d_1|}, \frac{w_2}{|d_L d_{L-1} \ldots d_3 d_2|}, \ldots, \frac{w_L}{|d_L|}\}}\right). \end{aligned} \tag{B.6}$$

Accordingly, the result of Lemma 6 follows by observing that the terms on the RHS of (B.6) multiplying the rectangular function are the output of a regular LCT with

parameter matrix,

$$
\begin{aligned}
&M_L M_{L-1} ... M_1 = \\
&\begin{bmatrix} & \frac{1}{d_L d_{L-1} ... d_2 d_1} & 0 \\ \frac{c_L}{d_{L-1} ... d_1} + \frac{c_{L-1} d_L}{d_{L-2} ... d_1} + \ldots + c_1 d_L d_{L-1} \ldots d_2 & & d_L \ldots d_2 d_1 \end{bmatrix} \\
&\triangleq \begin{bmatrix} a_{L1} & b_{L1} \\ c_{L1} & d_{L1} \end{bmatrix},
\end{aligned}
\tag{B.7}
$$

where $d_{L\ell} = d_L d_{L-1} \ldots d_\ell$ for $\ell \neq L$. □

3. Similar to the previous cases, the following lemma computes the output a sequence of clipping LCTs with $M_\ell = \begin{pmatrix} a_\ell & b_\ell \\ c_\ell & d_\ell \end{pmatrix}$, $\ell = 1, \ldots, L$, however, in this case the system is formed by interleaving both types of clipping LCTs, such that the LCTs with odd and even orders have zero and non-zero parameter b, respectively. We remark that this case is commonly encountered in various applications. For example, a sequence of lenses in an optical setup act as chirp multiplications (equivalent to LCTs with zero b parameter), while the free-space propagation between the lenses can be modeled as Fresnel diffractions (LCTs with non-zero b parameter).

Lemma 7. *Let $\psi(x)$ be the input to a sequence of L clipping LCTs with parameter matrices $M_\ell = \begin{pmatrix} a_\ell & b_\ell \\ c_\ell & d_\ell \end{pmatrix}$, $\ell = 1, \ldots, L$, where $b_{2\ell'} \neq 0$ and $b_{2\ell'-1} = 0$, $\ell' = 1, 2, \ldots, \frac{L}{2}$, and L an even integer. Then, the output is given by,*

$$
\begin{aligned}
\psi_o(u) = &\left(\prod_{\ell'=1}^{\frac{L}{2}} \frac{w'_{\ell'}}{2\pi |b'_{\frac{L}{2}\ell'}|} \right) \\
&\times \kappa_{\frac{L}{2}} \big\{ \psi(x); \{M'_{\frac{L}{2}\ell'}\}_{\ell'}, \{w'_{\ell'}\}_{\ell'} \big\}(u),\ \ell' = 1, 2, \ldots, \frac{L}{2},
\end{aligned}
\tag{B.8}
$$

where $w'_{\ell'} = \min\left\{w_{2\ell'}, \frac{w_{2\ell'-1}}{|d_{2\ell'-1}|}\right\}$, $M'_{\frac{L}{2}\ell'} \triangleq M'_{\frac{L}{2}} M'_{\frac{L}{2}-1} \ldots M'_{\ell'} = \begin{pmatrix} a'_{\frac{L}{2}\ell'} & b'_{\frac{L}{2}\ell'} \\ c'_{\frac{L}{2}\ell'} & d'_{\frac{L}{2}\ell'} \end{pmatrix}$, *and* $M'_{\ell'} = \begin{pmatrix} a'_{\ell'} & b'_{\ell'} \\ c'_{\ell'} & d'_{\ell'} \end{pmatrix} \triangleq M_{2\ell'} M_{2\ell'-1}$, $\ell' = 1, 2, \ldots, \frac{L}{2}$, *and* $\kappa_{\frac{L}{2}}$ *is defined through the recursion in (B.2) and (B.3).*

Proof. To prove (B.8), the cascade of clipping LCTs is viewed as a sequence of two-LCT blocks with parameter matrices $M_{2\ell'-1}$ and $M_{2\ell'}$, wherein $b_{2\ell'-1} = 0$ and $b_{2\ell'} \neq 0$. Accordingly, the output of each block for arbitrary input $\psi(x)$ is,

$$\begin{aligned} & T_{w_{2\ell'}}^{M_{2\ell'}}\left\{T_{w_{2\ell'-1}}^{M_{2\ell'-1}}\{\psi(x)\}(v)\right\}(u) = \int \sqrt{d_{2\ell'-1}}\; e^{i\frac{c_{2\ell'-1} d_{2\ell'-1}}{2} v^2} \\ & \times \psi(d_{2\ell'-1} v)\Pi\Big(\frac{d_{2\ell'-1} v}{w_{2\ell'-1}}\Big) \times h^{M_{2\ell'}}(v,u)\Pi\Big(\frac{v}{w_{2\ell'}}\Big)\, dv \\ & = \int T^{M_{2\ell'-1}}\{\psi(x)\}(v) h^{M_{2\ell'}}(v,u)\Pi\Big(\frac{v}{\min\{w_{2\ell'}, \frac{w_{2\ell'-1}}{|d_{2\ell'-1}|}\}}\Big) dv \\ & = T^{M_{2\ell'} M_{2\ell'-1}}_{\min\{w_{2\ell'}, \frac{w_{2\ell'-1}}{|d_{2\ell'-1}|}\}}\{\psi(x)\}(u), \end{aligned} \tag{B.9}$$

where $h^{M_{2\ell'}}(v,u)$ is the kernel of a regular LCT with the parameter matrix $M_{2\ell'}$. Since the overall b parameter of each two-LCT block is non-zero, the result of Lemma 5 is invoked to obtain the output of the cascade system. □

4. The final combination is similar to the previous case as a cascade of both types of LCTs but with the difference that the LCTs with the non-zero parameter b are placed in the odd orders.

Lemma 8. *Consider a similar setup as in the statement of Lemma 7, but with* $b_{2\ell'-1} \neq$

0 *and* $b_{2\ell'} = 0, \ell' = 1, 2, \ldots, \frac{L}{2}$. *The output of the cascade system is given by,*

$$\begin{aligned}\psi_o(u) = \left(\prod_{\ell'=1}^{\frac{L}{2}} \frac{w'_{\ell'}}{2\pi|b'_{\frac{L}{2}\ell'}|}\right) \times \kappa_{\frac{L}{2}}\big\{\psi(x); \{M'_{\frac{L}{2}\ell'}\}_{\ell'}, \{w'_{\ell'}\}_{\ell'}\big\}(u) \\ \times \Pi\Big(\frac{d_L u}{w_L}\Big), \ell' = 1, 2, \ldots, \frac{L}{2}\,,\end{aligned} \tag{B.10}$$

where $w'_1 = w_1$, $w'_{\ell'} = \min\{w_{2\ell'-1}, \frac{w_{2\ell'-2}}{|d_{2\ell'-2}|}\}$ *for* $\ell' = 2, 3, \ldots, \frac{L}{2}$ *and* $\kappa_{\frac{L}{2}}$ *is defined through the recursion in (B.2) and (B.3).*

Proof. Again, we view the cascade system as a sequence of two-LCT blocks with $b_{2\ell'-1} \neq 0$ and $b_{2\ell'} = 0$ for $\ell' = 1, 2, \ldots, \frac{L}{2}$. Therefore,

$$\begin{aligned}&T^{M_{2\ell'}}_{w_{2\ell'}}\big\{T^{M_{2\ell'-1}}_{w_{2\ell'-1}}\{\psi(x)\}\big\}(u) = \sqrt{d_{2\ell'}}\exp\Big(i\frac{c_{2\ell'}d_{2\ell'}}{2}u^2\Big) \\ &\times \int \psi(x)h^{M_{2\ell'-1}}(x, d_{2\ell'}u)\Pi\Big(\frac{x}{w_{2\ell'-1}}\Big)\,dx \times \Pi\Big(\frac{d_{2\ell'}u}{w_{2\ell'}}\Big) \\ &= T^{M_{2\ell'}M_{2\ell'-1}}_{w_{2\ell'-1}}\{\psi(x)\}(u)\Pi\Big(\frac{d_{2\ell'}u}{w_{2\ell'}}\Big),\ \ \ell' = 1, 2, \ldots, \frac{L}{2}.\end{aligned} \tag{B.11}$$

This represents the output of a clipping LCT with a non-zero b parameter multiplied by a rectangular function of width $\frac{w_{2\ell'}}{|d_{2\ell'}|}$. Since the b parameter of $M_{2\ell'}M_{2\ell'-1}$ is non-zero, we invoke Lemma 5 to obtain the output of the entire system as,

$$\begin{aligned}\psi_o(u) = T^{M_L M_{L-1}}_{\min\{w_{L-1}, \frac{w_{L-2}}{|d_{L-2}|}\}}\Bigg\{T^{M_{L-2}M_{L-3}}_{\min\{w_{L-3}, \frac{w_{L-4}}{|d_{L-4}|}\}}\Big\{\ldots\big\{T^{M_2M_1}_{w_1}\{\psi(x)\}\big\}\Big\}\Bigg\}(u) \\ \times \Pi\Big(\frac{d_L u}{w_L}\Big).\end{aligned} \tag{B.12}$$

Similar to the previous case, the expression in (B.12) amounts to the output of a sequence of $\frac{L}{2}$ LCTs multiplying the rectangular function $\Pi(\frac{d_L u}{w_L})$. □

APPENDIX C: PERMISSION LETTERS TO REPRINT THE ARTICLES [8, 13, 12, 9, 10, 11] IN THIS DISSERTATION

From: Davood Mardaninajafabadi <d.mardani@Knights.ucf.edu>
Sent: Thursday, February 14, 2019 2:02 PM
To: Permissions Helpdesk <permissionshelpdesk@elsevier.com>
Subject: Request for permission

***** External email: use caution *****

Dear Editor,

I am writing to request for a permission to use my published paper (in which I am the first author) in Signal Processing Journal in my doctoral dissertation. I am completing a doctoral dissertation degree at the University of Central Florida entitled "Sparse signal recovery under sensing and physical hardware constraints". I would like your permission to reprint in my thesis/dissertation excerpts from the following:

Davood Mardani, George K. Atia, Ayman F. Abouraddy, "Signal reconstruction from interferometric measurements under sensing constraints," Signal Processing, Volume 155, 2019, Pages 323-333.

I would be so thankful if you please read and sign the attached letters. Please fill the places where I mentioned in blue color.

Best,
Davood Mardani
University of Central Florida

Figure C.1: Reprint permission request email for the signal processing article.

From: Permissions Helpdesk <permissionshelpdesk@elsevier.com>
Sent: Friday, February 15, 2019 10:29 AM
To: Davood Mardaninajafabadi
Subject: RE: Request for permission

Dear Davood,

As an Elsevier journal author, you retain the right to Include the article in a thesis or dissertation (provided that this is not to be published commercially) whether in full or in part, subject to proper acknowledgment; see https://www.elsevier.com/about/our-business/policies/copyright/personal-use for more information. As this is a retained right, no written permission from Elsevier is necessary.

If I may be of further assistance, please let me know.

Best of luck with your dissertation and best regards,
Laura

Laura Stingelin
Permissions Helpdesk
ELSEVIER |Operations
+1 215-239-3867 office
l.stingelin@elsevier.com
permissionshelpdesk@elsevier.com

1600 John F Kennedy Boulevard, Suite 1800
Philadelphia, PA 19103-2899 USA

www.elsevier.com
Twitter | Facebook | LinkedIn | Google+

Figure C.2: First response to the reprint permission request email for the signal processing article.

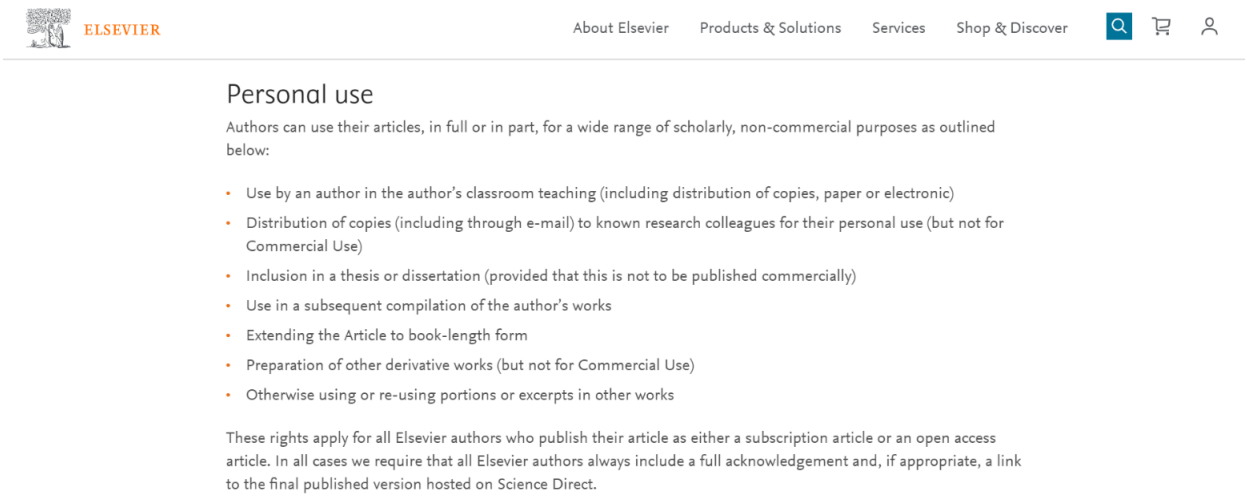

Figure C.3: Elsevier reprint permission page.

RE: Request for permission

Permissions Helpdesk <permissionshelpdesk@elsevier.com>
Wed 2/27/2019 3:39 PM
To: Davood Mardaninajafabadi <d.mardani@Knights.ucf.edu>

Dear Davood,

As outlined in our permissions licenses, this extends to the posting to your university's digital repository of the thesis provided that if you include the published journal article (PJA) version, it is embedded in your thesis only and not separately downloadable:

19. Thesis/Dissertation: If your license is for use in a thesis/dissertation your thesis may be submitted to your institution in either print or electronic form. Should your thesis be published commercially, please reapply for permission. These requirements include permission for the Library and Archives of Canada to supply single copies, on demand, of the complete thesis and include permission for Proquest/UMI to supply single copies, on demand, of the complete thesis. Should your thesis be published commercially, please reapply for permission. Theses and dissertations which contain embedded PJAs as part of the formal submission can be posted publicly by the awarding institution with DOI links back to the formal publications on ScienceDirect.

Best of luck with your thesis and best regards,

Laura

Laura Stingelin
Permissions Helpdesk
Domain Support
ELSEVIER |Operations
+1 215-239-3867 office
l.stingelin@elsevier.com
permissionshelpdesk@elsevier.com

1600 John F Kennedy Boulevard, Suite 1800
Philadelphia, PA 19103-2899 USA

www.elsevier.com
Twitter | Facebook | LinkedIn | Google+

Figure C.4: Second response to the reprint permission request email for the signal processing article.

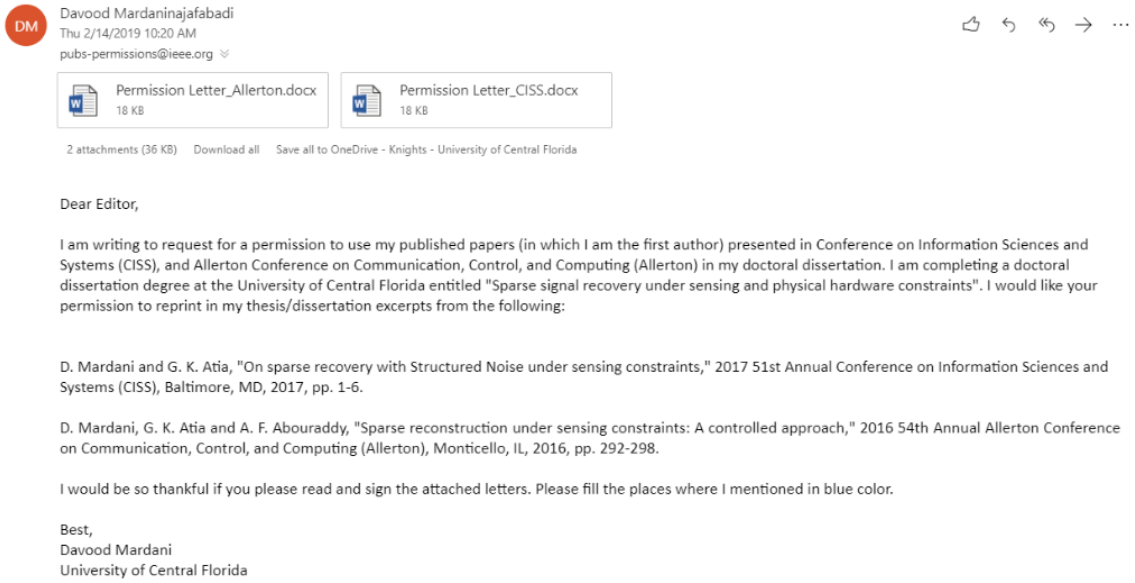

DM

Davood Mardaninajafabadi
Thu 2/14/2019 10:20 AM
pubs-permissions@ieee.org

Permission Letter_Allerton.docx
18 KB

Permission Letter_CISS.docx
18 KB

2 attachments (36 KB) Download all Save all to OneDrive - Knights - University of Central Florida

Dear Editor,

I am writing to request for a permission to use my published papers (in which I am the first author) presented in Conference on Information Sciences and Systems (CISS), and Allerton Conference on Communication, Control, and Computing (Allerton) in my doctoral dissertation. I am completing a doctoral dissertation degree at the University of Central Florida entitled "Sparse signal recovery under sensing and physical hardware constraints". I would like your permission to reprint in my thesis/dissertation excerpts from the following:

D. Mardani and G. K. Atia, "On sparse recovery with Structured Noise under sensing constraints," 2017 51st Annual Conference on Information Sciences and Systems (CISS), Baltimore, MD, 2017, pp. 1-6.

D. Mardani, G. K. Atia and A. F. Abouraddy, "Sparse reconstruction under sensing constraints: A controlled approach," 2016 54th Annual Allerton Conference on Communication, Control, and Computing (Allerton), Monticello, IL, 2016, pp. 292-298.

I would be so thankful if you please read and sign the attached letters. Please fill the places where I mentioned in blue color.

Best,
Davood Mardani
University of Central Florida

Figure C.5: Reprint permission request email for the IEEE papers.

Re: Request for permission

M.E. Brennan <me.brennan@ieee.org>
Thu 2/14/2019 11:39 AM

To: Davood Mardaninajafabadi <d.mardani@Knights.ucf.edu>
Cc: M E Brennan <me.brennan@ieee.org>; Joelle Masciulli <j.masciulli@ieee.org>

Dear Davood Mardani,

Please retain this mail for your records.
The IEEE does not require individuals working on a dissertation/thesis to obtain a formal reuse license however, you must follow the requirements listed below:

Textual Material

Using short quotes or referring to the work within these papers) users must give full credit to the original source (author, paper, publication) followed by the IEEE copyright line © [Year of publication] IEEE.

In the case of illustrations or tabular material, we require that the copyright line © [Year of original publication] IEEE appear prominently with each reprinted figure and/or table.

If a substantial portion of the original paper is to be used, and if you are not the senior author, also obtain the senior author's approval.

Full-Text Article

If you are using the entire IEEE copyright owned article, the following IEEE copyright/ credit notice should be placed prominently in the references: © [year of original publication] IEEE. Reprinted, with permission, from [author names, paper title, IEEE publication title, and month/year of publication]

Only the **accepted** version of an IEEE copyrighted paper can be used when posting the paper or your thesis on-line. You may not use the **final published** version

In placing the thesis on the author's university website, please display the following message in a prominent place on the website: In reference to IEEE copyrighted material which is used with permission in this thesis, the IEEE does not endorse any of [university/educational entity's name goes here]'s products or services. Internal or personal use of this material is permitted. If interested in reprinting/republishing IEEE copyrighted material for advertising or promotional purposes or for creating new collective works for resale or redistribution, please go to

http://www.ieee.org/publications_standards/publications/rights/rights_link.html

to learn how to obtain a License from RightsLink.

If applicable, University Microfilms and/or ProQuest Library, or the Archives of Canada may supply single copies of the dissertation.

Kind regards,

M.E. Brennan

Ms M.E. Brennan
IEEE
501 Hoes Lane
Piscataway, NJ 08854-4141 USA
me.brennan@ieee.org

+1 (732) 562-2660

Figure C.6: Response to the reprint permission request email for the IEEE papers.

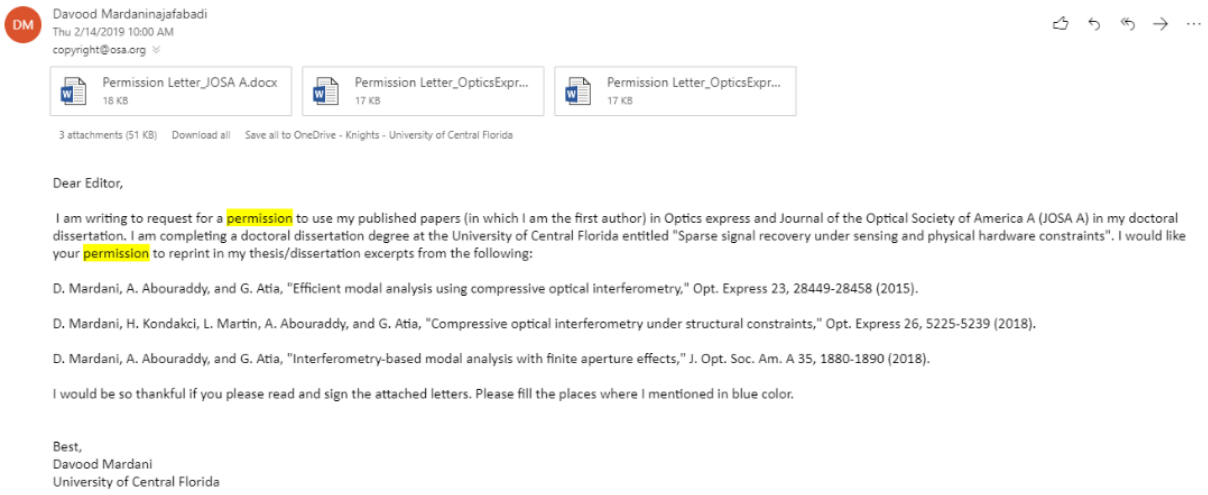

Davood Mardaninajafabadi
Thu 2/14/2019 10:00 AM
copyright@osa.org

Permission Letter_JOSA A.docx 18 KB
Permission Letter_OpticsExpr... 17 KB
Permission Letter_OpticsExpr... 17 KB

3 attachments (51 KB) Download all Save all to OneDrive - Knights - University of Central Florida

Dear Editor,

I am writing to request for a permission to use my published papers (in which I am the first author) in Optics express and Journal of the Optical Society of America A (JOSA A) in my doctoral dissertation. I am completing a doctoral dissertation degree at the University of Central Florida entitled "Sparse signal recovery under sensing and physical hardware constraints". I would like your permission to reprint in my thesis/dissertation excerpts from the following:

D. Mardani, A. Abouraddy, and G. Atia, "Efficient modal analysis using compressive optical interferometry," Opt. Express 23, 28449-28458 (2015).

D. Mardani, H. Kondakci, L. Martin, A. Abouraddy, and G. Atia, "Compressive optical interferometry under structural constraints," Opt. Express 26, 5225-5239 (2018).

D. Mardani, A. Abouraddy, and G. Atia, "Interferometry-based modal analysis with finite aperture effects," J. Opt. Soc. Am. A 35, 1880-1890 (2018).

I would be so thankful if you please read and sign the attached letters. Please fill the places where I mentioned in blue color.

Best,
Davood Mardani
University of Central Florida

Figure C.7: Reprint permission request email for the OSA articles.

RE: Request for permission

pubscopyright <copyright@osa.org>
Wed 2/27/2019 4:12 PM
To: Davood Mardaninajafabadi <d.mardani@Knights.ucf.edu>; pubscopyright <copyright@osa.org>

Dear Davood Mardani,

Thank you for contacting The Optical Society.

For the use of material from **[1]** D. Mardani, A. Abouraddy, and G. Atia, "Efficient modal analysis using compressive optical interferometry," Opt. Express 23, 28449-28458 (2015) and **[3]** D. Mardani, A. Abouraddy, and G. Atia, "Interferometry-based modal analysis with finite aperture effects," J. Opt. Soc. Am. A 35, 1880-1890 (2018):

> Because you are the author of the source paper from which you wish to reproduce material, OSA considers your requested use of its copyrighted materials to be permissible within the author rights granted in the Copyright Transfer Agreement submitted by the requester on acceptance for publication of his/her manuscript. If the entire article is being included, it is requested that the **Author Accepted Manuscript** (or preprint) version be the version included within the thesis and that a complete citation of the original material be included in any publication. This permission assumes that the material was not reproduced from another source when published in the original publication.

The **Author Accepted Manuscript** version is the preprint version of the article that was accepted for publication but not yet prepared and/or formatted by The Optical Society or its vendors.

For the use of material from **[2]** D. Mardani, H. Kondakci, L. Martin, A. Abouraddy, and G. Atia, "Compressive optical interferometry under structural constraints," Opt. Express 26, 5225-5239 (2018).

> Because you are the author of the source paper from which you wish to reproduce material, OSA considers your requested use of its copyrighted materials to be permissible within the author rights granted in the Copyright Transfer Agreement submitted by the requester on acceptance for publication of his/her manuscript. It is requested that a complete citation of the original material be included in any publication. This permission assumes that the material was not reproduced from another source when published in the original publication.

While your publisher should be able to provide additional guidance, OSA prefers the below citation formats:

> For citations in figure captions:
>
> [Reprinted/Adapted] with permission from ref [x], [Publisher]. (with full citation in reference list)
>
> For images without captions:
>
> Journal Vol. #, first page (year published) An example: J. Opt. Soc. Am. A 35, 1880 (2018)

OSA considers this email to be sufficient authorization for the use of the requested material.

Please let me know if you have any questions.

Kind Regards,

Rebecca Robinson

Rebecca Robinson
February 27, 2019
Authorized Agent, The Optical Society

The Optical Society (OSA)
2010 Massachusetts Ave., NW
Washington, DC 20036 USA
www.osa.org

Reflecting a Century of Innovation

Figure C.8: Response to the reprint permission request email for the OSA articles.

LIST OF REFERENCES

[1] S. Hawe, M. Kleinsteuber, and K. Diepold, "Analysis operator learning and its application to image reconstruction," *IEEE Transactions on Image Processing*, vol. 22, no. 6, pp. 2138–2150, 2013.

[2] S. R. Arridge and J. C. Schotland, "Optical tomography: forward and inverse problems," *Inverse Problems*, vol. 25, no. 12, p. 123010, 2009.

[3] R. Szeliski, *Computer vision algorithms and applications*. Springer, 2011.

[4] E. D. Vito, L. Rosasco, A. Caponnetto, U. D. Giovannini, and F. Odone, "Learning from examples as an inverse problem," *Journal of Machine Learning Research*, vol. 6, pp. 883–904, 2005.

[5] L. Denis, D. Lorenz, E. Thiébaut, C. Fournier, and D. Trede, "Inline hologram reconstruction with sparsity constraints," *Opt. Lett.*, vol. 34, no. 22, pp. 3475–3477, Nov 2009.

[6] Y. Wang, J. Yang, W. Yin, and Y. Zhang, "A new alternating minimization algorithm for total variation image reconstruction," *SIAM Journal on Imaging Sciences*, vol. 1, no. 3, pp. 248–272, 2008.

[7] M. F. Duarte, M. A. Davenport, D. Takhar, J. N. Laska, T. Sun, K. F. Kelly, and R. G. Baraniuk, "Single-pixel imaging via compressive sampling," *IEEE Signal Processing Magazine*, vol. 25, no. 2, pp. 83–91, March 2008.

[8] D. Mardani, G. K. Atia, and A. F. Abouraddy, "Signal reconstruction from interferometric measurements under sensing constraints," *Signal Processing*, vol. 155,

pp. 323 – 333, 2019. [Online]. Available: http://www.sciencedirect.com/science/article/pii/S0165168418303402

[9] D. Mardani, A. F. Abouraddy, and G. K. Atia, "Efficient modal analysis using compressive optical interferometry," *Opt. Express*, vol. 23, no. 22, pp. 28 449–28 458, Nov 2015. [Online]. Available: http://www.opticsexpress.org/abstract.cfm?URI=oe-23-22-28449

[10] D. Mardani, H. E. Kondakci, L. Martin, A. F. Abouraddy, and G. K. Atia, "Compressive optical interferometry under structural constraints," *Opt. Express*, vol. 26, no. 5, pp. 5225–5239, Mar 2018.

[11] D. Mardani, A. F. Abouraddy, and G. K. Atia, "Interferometry-based modal analysis with finite aperture effects," *J. Opt. Soc. Am. A*, vol. 35, no. 11, pp. 1880–1890, Nov 2018. [Online]. Available: http://josaa.osa.org/abstract.cfm?URI=josaa-35-11-1880

[12] D. Mardani, G. K. Atia, and A. F. Abouraddy, "Sparse reconstruction under sensing constraints: A controlled approach," in *2016 54th Annual Allerton Conference on Communication, Control, and Computing (Allerton)*, Sep. 2016, pp. 292–298.

[13] D. Mardani and G. K. Atia, "On sparse recovery with structured noise under sensing constraints," in *2017 51st Annual Conference on Information Sciences and Systems (CISS)*, March 2017, pp. 1–6.

[14] D. Mardani, H. E. Kondakci, L. Martin, A. F. Abouraddy, and G. K. Atia, "Modal analysis via compressive optical interferometry," in *2017 IEEE Photonics Conference (IPC)*, Oct 2017, pp. 621–622.

[15] L. Martin, D. Mardani, H. E. Kondakci, W. D. Larson, S. Shabahang, A. K. Jahromi, T. Malhotra, A. N. Vamivakas, G. K. Atia, and A. F. Abouraddy, "Basis-neutral Hilbert-space analyzers," *Scientific Reports*, vol. 7, p. 44995, 2017.

[16] M. I. Akhlaghi and A. Dogariu, "Compressive correlation imaging with random illumination," *Opt. Lett.*, vol. 40, no. 19, pp. 4464–4467, Oct 2015.

[17] V. Durán, F. Soldevila, E. Irles, P. Clemente, E. Tajahuerce, P. Andrés, and J. Lancis, "Compressive imaging in scattering media," *Opt. Express*, vol. 23, no. 11, pp. 14 424–14 433, Jun 2015.

[18] E. Tajahuerce, V. Durán, P. Clemente, E. Irles, F. Soldevila, P. Andrés, and J. Lancis, "Image transmission through dynamic scattering media by single-pixel photodetection," *Opt. Express*, vol. 22, no. 14, pp. 16 945–16 955, Jul 2014.

[19] A. F. Fercher, W. Drexler, C. K. Hitzenberger, and T. Lasser, "Optical coherence tomography— principles and applications," *Rep. Prog. Phys.*, vol. 66, no. 2, pp. 239–303, Jan. 2003.

[20] L. Martínez-León, P. Clemente, Y. Mori, V. Climent, J. Lancis, and E. Tajahuerce, "Single-pixel digital holography with phase-encoded illumination," *Opt. Express*, vol. 25, no. 5, pp. 4975–4984, Mar 2017.

[21] P. Clemente, V. Durán, E. Tajahuerce, P. Andrés, V. Climent, and J. Lancis, "Compressive holography with a single-pixel detector," *Opt. Lett.*, vol. 38, no. 14, pp. 2524–2527, Jul 2013.

[22] W. Gong and S. Han, "High-resolution far-field ghost imaging via sparsity constraint," *Scientific Reports*, vol. 5, p. 9280, 2015.

[23] G. R. Arce, D. J. Brady, L. Carin, H. Arguello, and D. S. Kittle, "Compressive coded aperture spectral imaging: An introduction," *IEEE Signal Processing Magazine*, vol. 31, no. 1, pp. 105–115, Jan 2014.

[24] G. A. Howland, J. Schneeloch, D. J. Lum, and J. C. Howell, "Simultaneous measurement of complementary observables with compressive sensing," *Phys. Rev. Lett.*, vol. 112, p. 253602, 2014.

[25] G. A. Howland, S. H. Knarr, J. Schneeloch, D. J. Lum, and J. C. Howell, "Compressively characterizing high-dimensional entangled states with complementary, random filtering," *Phys. Rev. X*, vol. 6, p. 021018, May 2016. [Online]. Available: https://link.aps.org/doi/10.1103/PhysRevX.6.021018

[26] J. Li, J. S. Li, Y. Y. Pan, and R. Li, "Compressive optical image encryption," *Sci. Rep.*, vol. 5, p. 10374, 2015.

[27] N. Rawat, B. Kim, I. Muniraj, G. Situ, and B.-G. Lee, "Compressive sensing based robust multispectral double-image encryption," *Appl. Opt.*, vol. 54, no. 7, pp. 1782–1793, Mar 2015.

[28] J. P. Dumas, M. A. Lodhi, W. U. Bajwa, and M. C. Pierce, "From modeling to hardware: an experimental evaluation of image plane and fourier plane coded compressive optical imaging," *Opt. Express*, vol. 25, no. 23, pp. 29 472–29 491, Nov 2017.

[29] D. Marcos, T. Lasser, A. López, and A. Bourquard, "Compressed imaging by sparse random convolution," *Opt. Express*, vol. 24, no. 2, pp. 1269–1290, Jan 2016.

[30] E. J. Candes, "The restricted isometry property and its implications for compressed sensing," *Compte Rendus de l'Academie des Sciences*, vol. 346, pp. 589–592, 2008.

[31] E. Hecht, *Optics*. Addison-Wesley, 2002.

[32] D. Mendlovic, *Optical Superresolution*. Springer New York, 2012.

[33] S. Farsiu, D. Robinson, M. Elad, and P. Milanfar, "Advances and challenges in super-resolution," *International Journal of Imaging Systems and Technology*, vol. 14, no. 2, pp. 47–57.

[34] D. A. Boas, D. H. Brooks, E. L. Miller, C. A. DiMarzio, M. Kilmer, R. J. Gaudette, and Q. Zhang, "Imaging the body with diffuse optical tomography," *IEEE Signal Processing Magazine*, vol. 18, no. 6, pp. 57–75, Nov 2001.

[35] H. E. Kondakci and A. F. Abouraddy, "Diffraction-free pulsed optical beams via space-time correlations," *Opt. Express*, vol. 24, no. 25, pp. 28 659–28 668, Dec 2016. [Online]. Available: http://www.opticsexpress.org/abstract.cfm?URI=oe-24-25-28659

[36] H. E. Kondakci and A. F. Abouraddy, "Diffraction-free space–time light sheets," *Nature Photonics*, no. 11, pp. 733—740, October 2017.

[37] A. F. Abouraddy, T. M. Yarnall, and B. E. A. Saleh, "Generalized optical interferometry for modal analysis in arbitrary degrees of freedom," *Opt. Lett.*, vol. 37, pp. 2889–2891, 2012.

[38] N. Mohan, I. Stojanovic, W. C. Karl, B. E. A. Saleh, and M. C. Teich, "Compressed sensing in optical coherence tomography," *Proc. SPIE*, vol. 7570, p. 75700L, 2010.

[39] Y. Rivenson, A. Stern, and J. Rosen, "Reconstruction guarantees for compressive tomographic holography," *Opt. Lett.*, vol. 38, no. 14, pp. 2509–2511, Jul 2013.

[40] Y. Wang, X. Ma, C. Chen, and X. Guan, "Designing dual-tone radio interferometric positioning systems," *IEEE Transactions on Signal Processing*, vol. 63, no. 6, pp. 1351–1365, March 2015.

[41] M. Maróti, P. Völgyesi, S. Dóra, B. Kusý, A. Nádas, A. Lédeczi, G. Balogh, and K. Molnár, "Radio interferometric geolocation," in *Proceedings of the 3rd International Conference on Embedded Networked Sensor Systems*, ser. SenSys '05. New York, NY, USA: ACM, 2005, pp. 1–12. [Online]. Available: http://doi.acm.org/10.1145/1098918.1098920

[42] L. Martin, W. D. Larson, H. E. Kondakci, D. Mardani, S. Shabahang, A. K. Jahromi, T. Malhotra, A. N. Vamivakas, G. K. Atia, and A. F. Abouraddy, "Hilbert-space analyzers: Basis-neutral modal analysis via generalized optical interferometry," in *Frontiers in Optics 2016*. Optical Society of America, 2016, p. FF3G.2. [Online]. Available: http://www.osapublishing.org/abstract.cfm?URI=FiO-2016-FF3G.2

[43] M. E. Brezinski, *Optical Coherence Tomography*. Academic Press, 2006.

[44] E. J. Candes and Y. Plan, "A probabilistic and RIPless theory of compressed sensing," *IEEE Transactions on Information Theory*, vol. 57, no. 11, pp. 7235–7254, Nov 2011.

[45] M. Lustig, D. L. Donoho, J. M. Santos, and J. M. Pauly, "Compressed sensing mri," *IEEE Signal Processing Magazine*, vol. 25, no. 2, pp. 72–82, March 2008.

[46] H. Pan, T. Blu, and M. Vetterli, "Towards generalized FRI sampling with an application to source resolution in radioastronomy," *IEEE Transactions on Signal Processing*, vol. 65, no. 4, pp. 821–835, Feb 2017.

[47] A. R. Thompson, J. M. Moran, and G. W. Swenson, *Interferometry and Synthesis in Radio Astronomy*. Wiley-VCH Verlag GmbH, 2007. [Online]. Available: http://dx.doi.org/10.1002/9783527617845.ch2

[48] J. A. Hogbom, "Aperture Synthesis with a Non-Regular Distribution of Interferometer Baselines," *A & A Supplement*, vol. 15, pp. 417–426, 1974.

[49] Y. Wiaux, G. Puy, Y. Boursier, and P. Vandergheynst, "Compressed sensing for radio interferometry: spread spectrum imaging techniques," *Proc.SPIE*, vol. 7446, pp. 7446 – 7446 – 6, 2009.

[50] F. Li, T. Cornwell, and F. De hoog, "The applications of compressive sensing to radio astronomy," in *Wireless Algorithms, Systems, and Applications*. Springer Berlin Heidelberg, 2010, pp. 352–359.

[51] M. A. Richards, "A beginner's guide to interferometric sar concepts and signal processing [aess tutorial iv]," *IEEE Aerospace and Electronic Systems Magazine*, vol. 22, no. 9, pp. 5–29, Sept 2007.

[52] G. Fornaro, F. Lombardini, A. Pauciullo, D. Reale, and F. Viviani, "Tomographic processing of interferometric SAR data: Developments, applications, and future research perspectives," *IEEE Signal Processing Magazine*, vol. 31, no. 4, pp. 41–50, July 2014.

[53] M. Born and E. Wolf, *Principles of Optics: Electromagnetic Theory of Propagation, Interference and Diffraction of Light*. Cambridge University Press, 1999.

[54] A. F. Abouraddy, T. M. Yarnall, and B. E. A. Saleh, "Angular and radial mode analyzer for optical beams," *Opt. Lett.*, vol. 36, pp. 4683–4685, 2011.

[55] Z. Barber, C. Harrington, C. Thiel, W. Babbitt, and R. K. Mohan, "Angle of arrival estimation using spectral interferometry," *Journal of Luminescence*, vol. 130, no. 9, pp. 1614 – 1618, 2010.

[56] A. Glindemann, *Principles of Stellar Interferometry*. Springer Berlin Heidelberg, 2011.

[57] J. G. Fujimoto, C. Pitris, S. A. Boppart, and M. E. Brezinski, "Optical coherence tomography: An emerging technology for biomedical imaging and optical biopsy," *Neoplasia*, vol. 2, no. 1–2, pp. 9 – 25, 2000.

[58] J. Wang, J. Yang, I. M. Fazal, N. Ahmed, Y. Yan, H. Huang, Y. Ren, Y. Yue, S. Dolinar, M. Tur, and A. E. Willner, "Terabit free-space data transmission employing orbital angular momentum multiplexing," *Nat. Photon.*, vol. 6, pp. 488–496, January 2012.

[59] N. Bozinovic, Y. Yue, Y. Ren, M. Tur, P. Kristensen, H. Huang, A. E. Willner, and S. Ramachandran, "Terabit-scale orbital angular momentum mode division multiplexing in fibers," *Science*, vol. 340, pp. 1545–1548, June 2013.

[60] J. Demas and S. Ramachandran, "Sub-second mode measurement of fibers using c2 imaging," *Opt. Express*, vol. 22, no. 19, pp. 23 043–23 056, Sep 2014. [Online]. Available: http://www.opticsexpress.org/abstract.cfm?URI=oe-22-19-23043

[61] L. Allen, M. W. Beijersbergen, R. J. C. Spreeuw, and J. P. Woerdman, "Orbital angular momentum of light and the transformation of laguerre-gaussian laser modes," *Phys. Rev. A*, vol. 45, pp. 8185–8189, Jun 1992. [Online]. Available: https://link.aps.org/doi/10.1103/PhysRevA.45.8185

[62] V. Namias, "The fractional fourier transform and its application in quantum mechanics," *IMA J. Appl. Math.*, vol. 25, pp. 241–256, 1980.

[63] H. Ozaktas, M. Kutay, and Z. Zalevsky, *The Fractional Fourier Transform: With Applications in Optics and Signal Processing*, ser. Wiley Series in Pure and Applied Optics. Wiley, 2001. [Online]. Available: https://books.google.com/books?id=1TQbAQAAIAAJ

[64] V. Namias, "Fractionalization of hankel transforms," *IMA J. Appl. Math.*, vol. 26, pp. 187–197, 1980.

[65] L. Yu, Y. Lu, X. Zeng, M. Huang, M. Chen, W. Huang, and Z. Zhu, "Deriving the integral representation of a fractional hankel transform from a fractional fourier

transform," *Opt. Lett.*, vol. 23, no. 15, pp. 1158–1160, Aug 1998. [Online]. Available: http://ol.osa.org/abstract.cfm?URI=ol-23-15-1158

[66] D. L. Donoho, "Compressed sensing," *IEEE Trans. Inf. Theory*, vol. 52, pp. 1289–1306, April 2006.

[67] E. J. Candes, "Compressed sensing," *Proc. Int. Congress of Mathematicians*, 2006.

[68] E. J. Candes, J. Romberg, and T. Tao, "Robust uncertainty principles: exact signal reconstruction from highly incomplete frequency information," *IEEE Transactions on Information Theory*, vol. 52, no. 2, pp. 489–509, Feb 2006.

[69] M. Saunders, "Pdco: Primal-dual interior method for convex objectives," *http://www.stanford.edu/group/SOL/software/pdco*.

[70] E. Candes and T. Tao, "The dantzig selector: Statistical estimation when p is much larger than n," *The Annals of Statistics*, vol. 35, no. 6, pp. 2313–2351, 2007.

[71] J. Tropp, "Greed is good: Algorithmic results for sparse approximation," *IEEE Trans. Info. Theory*, vol. 50, pp. 2231–2242, October 2004.

[72] W. Dai and O. Milenkovic, "Subspace pursuit for compressive sensing signal reconstruction," *IEEE Trans on Inf. Theory*, vol. 55, no. 5, pp. 2230–2249, May 2009.

[73] R. Tibshirani, "Regression shrinkage and selection via the lasso," *Journal of the Royal Statistical Society, Series B*, vol. 58, pp. 267–288, 1994.

[74] S. C. Pei and J. J. Ding, "Relations between gabor transforms and fractional fourier transforms and their applications for signal processing," *IEEE Trans. Signal Process.*, vol. 55, no. 10, pp. 4839–4850, Oct 2007.

[75] B. E. A. Saleh and M. C. Teich, *Fundamentals of Photonics*. John Wiley & Sons, 1994.

[76] A. Siegman, *Lasers*. University Science Books, 1986.

[77] M. Mirhosseini, O. S. Magaña-Loaiza, S. M. H. Rafsanjani, and R. W. Boyd, "Compressive direct measurement of the quantum wave function," *Phys. Rev. Lett.*, vol. 113, p. 090402, 2014.

[78] X. Liu and J. U. Kang, "Compressive SD-OCT: the application of compressed sensing in spectral domain optical coherence tomography," *Opt. Express*, vol. 18, no. 21, pp. 22 010–22 019, Oct 2010.

[79] R. Baraniuk, M. Davenport, R. DeVore, and M. Wakin, "A simple proof of the restricted isometry property for random matrices," *Constructive Approximation*, vol. 28, no. 3, pp. 253–263, 2008. [Online]. Available: http://dx.doi.org/10.1007/s00365-007-9003-x

[80] J. M. Steele, *The Cauchy-Schwarz Master Class: An Introduction to the Art of Mathematical Inequalities*. New York, NY, USA: Cambridge University Press, 2004.

[81] W. Hoeffding, "Probability inequalities for sums of bounded random variables," *Journal of the American Statistical Association*, vol. 58, no. 301, pp. 13–30, 1963. [Online]. Available: http://www.jstor.org/stable/2282952

[82] S. Bourguignon, J. Ninin, H. Carfantan, and M. Mongeau, "Exact sparse approximation problems via mixed-integer programming: Formulations and computational performance," *IEEE Transactions on Signal Processing*, vol. 64, no. 6, pp. 1405–1419, March 2016.

[83] D. Mardani and G. K. Atia, "Adaptive sequential compressive detection," *48th Asilomar Conference on Signals, Systems and Computers*, pp. 632–636, Nov 2014.

[84] D. Malioutov, S. Sanghavi, and A. Willsky, "Sequential compressed sensing," *IEEE Journal of Selected Topics in Signal Processing*, vol. 4, pp. 435–444, April 2010.

[85] H. Tan and C. H. Meyer, "Estimation of k-space trajectories in spiral MRI," *Magnetic Resonance in Medicine*, vol. 61, no. 6, pp. 1396–1404, 2009. [Online]. Available: http://dx.doi.org/10.1002/mrm.21813

[86] J. N. Laska, P. T. Boufounos, M. A. Davenport, and R. G. Baraniuk, "Democracy in action: Quantization, saturation, and compressive sensing," *Applied and Computational Harmonic Analysis*, vol. 31, no. 3, pp. 429 – 443, 2011. [Online]. Available: http://www.sciencedirect.com/science/article/pii/S1063520311000248

[87] J. N. Laska, M. A. Davenport, and R. G. Baraniuk, "Exact signal recovery from sparsely corrupted measurements through the pursuit of justice," in *43rd Asilomar Conf. on Sig., Sys. and Comp.*, Nov 2009, pp. 1556–1560.

[88] T. Blumensath, "Compressed sensing with nonlinear observations and related nonlinear optimization problems," *IEEE Transactions on Information Theory*, vol. 59, no. 6, pp. 3466–3474, June 2013.

[89] E. J. Candes and T. Tao, "Near-optimal signal recovery from random projections: Universal encoding strategies?" *IEEE Trans. on Inf. Theory*, vol. 52, no. 12, pp. 5406–5425, Dec 2006.

[90] D. Mardani, G. Atia, and A. F. Abouraddy, "Compressive interferometry for optical modal analysis in arbitrary degrees of freedom," *Information Theory and Applications Workshop (ITA)*, Feb. 2015.

[91] T. T. Cai and L. Wang, "Orthogonal matching pursuit for sparse signal recovery with noise," *IEEE Trans. on Inf. Theory*, vol. 57, no. 7, pp. 4680–4688, July 2011.

[92] M. A. Davenport and M. B. Wakin, "Analysis of orthogonal matching pursuit using the restricted isometry property," *IEEE Trans on Inf. Theory*, vol. 56, no. 9, pp. 4395–4401, Sept 2010.

[93] D. L. Donoho and X. Huo, "Uncertainty principles and ideal atomic decomposition," *IEEE Trans. on Inf. Theory*, vol. 47, no. 7, pp. 2845–2862, Nov 2001.

[94] M. Moshinsky and C. Quesne, "Linear canonical transformations and their unitary representations," *Journal of Mathematical Physics*, vol. 12, no. 8, pp. 1772–1780, 1971.

[95] B. D. Cullity, *Introduction to Magnetic Materials*. Reading, MA: Addison-Wesley, 1972.

[96] S.-C. Pei and J.-J. Ding, "Eigenfunctions of linear canonical transform," *IEEE Transactions on Signal Processing*, vol. 50, no. 1, pp. 11–26, Jan 2002.

[97] M. Yessenov, L. Mach, B. Bhaduri, D. Mardani, H. E. Kondakci, G. K. Atia, M. A. Alonso, and A. F. Abouraddy, "What is the maximum differential group delay achievable by a space-time wave packet in free space?" *Opt. Express*, vol. 27, no. 9, pp. 12 443–12 457, Apr 2019.

[98] L. B. Almeida, "Product and convolution theorems for the fractional fourier transform," *IEEE Signal Processing Letters*, vol. 4, no. 1, pp. 15–17, Jan 1997.